ABSTRACT

Title of Dissertation: HIGH EFFICIENCY CIS SOLAR CELLS BY A SIMPLE TWO-STEP SELENIZATION PROCESS AND WAVEGUIDE BRAGG GRATINGS IN INTEGRATED PHOTONICS

Yang Zhang, Doctor of Philosophy, 2019

Dissertation directed by: Professor Mario Dagenais, Department of Electrical and Computer Engineering

Part I: High Efficiency CIS Solar Cells with Simple Fabrication Method

CIS has a very high optical absorption coefficient, which makes it able to absorb more than 90% of the incident photons with energies higher than 1.04 eV within 1-2 μm thickness. Because of the high absorption coefficient and low bandgap, high quality CIS solar cells can have a very high short circuit current compared with other thin film material or other type of solar cells. We offer a very simple two-step process based on annealing stacked elemental layers under selenium vapor within a graphite box, followed by a potassium fluoride postdeposition treatment, which is a low-cost and highly manufacturable approach. We are able to reproducibly achieve above 12% conversion efficiency, with the champion cell exhibiting near-record 14.7% efficiency. Our results indicate that perhaps the CIS system is less sensitive to elaborate processing steps and details than previously thought. This simple approach

offers a very useful experimental platform from which to study a variety of thin film PV research topics, including the possibility of producing tandem solar cell by also using perovskite.

Part II: Waveguides Bragg Gratings in Integrated Photonics

Integrated photonics on silicon-based material combines two great inventions of the last century: silicon technology and photonic technology. It is paving the way for a monolithically integrated optoelectronic platform on a single chip. Being a prevailing research topic in the past decade, it has seen tremendous progress with the successful development of high-performance components. Among all integrated photonics platforms, the silicon nitride planar waveguide platform provides benefits like low optical losses, transparency over a wide wavelength range (400-2350 nm), compatibility with CMOS and wafer-scale foundry processes, and high-power handling capabilities.

In this part, waveguides Bragg gratings are investigated to improve the performance of several integrated photonics components. An 83-dB rejection ratio pump filter using a periodic waveguide Bragg grating with an efficient z-shape waveguide design to suppress the TM mode and avoid scattered modes is demonstrated. Fabry-Perot cavity enhanced four-wave mixing devices are optimized based on a numerical model developed with an ABCD matrix method and four-wave mixing in a Fabry-Perot cavity that uses grating is demonstrated experimentally. Finally, to reduce the pixel size and power consumption of optical phased array for virtual reality applications, complex waveguide Bragg gratings are generated via both Layer Peeling/Adding algorithm and genetic algorithm to support slow-light modes over certain bandwidth.

HIGH EFFICIENCY CIS SOLAR CELLS BY A SIMPLE TWO-STEP SELENIZATION PROCESS AND WAVEGUIDE BRAGG GRATINGS IN INTEGRATED PHOTONICS

by

Yang Zhang

Dissertation submitted to the Faculty of the Graduate School of the
University of Maryland, College Park, in partial fulfillment
of the requirements for the degree of
Doctor of Philosophy
2019

Advisory Committee:
Professor Mario Dagenais, Chair
Professor Martin Peckerar
Professor Phillip Sprangle
Professor Thomas E. Murphy
Professor Amitabh Varshney

Acknowledgements

My journey of attaining a Ph.D. in electrical and computer engineer at UMD is filled with frustration and joyfulness, obstacles and success. It is a unique experience in which that I learn to accept the failures and challenges, and stay resilient and motivated. On the way to touching the shiny degree, there are many people I would like to give my heartful thanks to. Without your support and advice, my journey would not be so wonderful.

First and foremost, I would like to thank my advisor, Professor Mario Dagenais, who provided me with the opportunity and the resources to carry out the work presented in this thesis. Without his guidance and encouragement, the achievement made in this thesis work would not come true. Without his persistence and fruitful discussions, I could still be trapped somewhere and lost in determining the direction of my research. Supported by Prof. Dagenais, I have devoted myself fully on the projects with a diverse set of research experiences which have been instrumental in my development as both an independent and collaborative researcher.

I would like to thank Prof. Martin Peckerar and Prof. Amitabh Varshney for their insightful technical discussion on my thesis work about optical phased array. The biweekly meeting with them was always fruitful and full with passion. I would also like to thank Prof. Israel De León of Tecnológico de Monterrey for the frequent discussion as well as his insights on slow-light device. I want to thank Dr. Bob Bartolo for guiding the work of CIS solar cell and for sharing his knowledge and intuition of photovoltaics. I would also like to thank Prof. Phillip Sprangle and Prof.

Thomas E. Murphy for serving my thesis committee and for giving me valuable advices on my thesis.

One of the amazing treasures of UMD is its well-known scholars and talented students. It was my privilege to work with Jim O'Connor, Jonathan A. Hummel, Tom Loughran, John Abrahams and Mark Lecates from the Nano-Fabrication Lab, who are highly experienced in nano-fabrication and generous with their help. There are many brilliant colleagues in our group. I would like to give special thanks to Dr. Tian Li, Dr. Yang Meng and Dr. Tiecheng Zhu who helped me a lot with my research in the first two years of my Ph.D. study. I would also like to thank Dr. Yangyi Yao, Wei-Lun Hsu, Yiwen Hu, Dr. Feifei Chen, Shengjie Xie, Jiahao Zhan, Pradip Gatkine, Po-chun Huang and Xueton Sun for the research ideas and frequent discussions. In addition, I would like to thank all the people in the Nanocenter and the X-ray Crystallographic Center at UMD.

To Jiaqi Dai, Zhengyang Wang, Yuzhi Hu, Chen Li, Xiaoxiao Ge, and many others, thank you for being such great friends and for accompanying me all the time for over six-and-half years.

Moreover, I would like to thank my parents Shengjun Zhang and Aizhen He and my family in China. Without their sacrifices and unconditional love, I would not have made it this far. I love you all very much.

Last but not least, I would like to thank my wife, Xi Zhang. You were the first line of defense against the looming stresses of my Ph.D. life. Your understanding and support was the motivation that kept me doing well in both research and personal life. This thesis is dedicated to you.

Table of Contents

List of Tables

List of Figures

Part I High Efficiency CIS Solar Cells with Simple Fabrication Method

Chapter 1 Introduction

Silicon was the first commercial solar cell material and is still the most generally used material in solar cell applications. However, silicon is not the ideal material for solar cells because it has low absorption efficiency due to an indirect band gap. A lot of semiconductors have been investigated to serve as an alternative to silicon-based solar cells. Among them, $Cu(In,Ga)Se_2$-based (CIGS) solar cells are one of the most promising candidates as a cost-effective high-performance solar cells. It has many advantages as a thin film solar cell absorber, for instance, low-cost, high-rate semiconductor deposition over large areas using layers only a few microns thick, direct band gap, a high absorption coefficient ($\sim 10^5$ cm^{-1}), which can be used for the fabrication of monolithically interconnected modules and as a tandem cell. Furthermore, CIGS solar cells and modules have shown excellent long-term stability in outdoor testing. CIGS have exhibited the highest conversion efficiencies among the thin-film solar cell technology. As we can see in Figure 1.1, in recent years, several research laboratories in the world have reported cutting-edge high efficiency CIGS solar cells with efficiencies above 22% [1,2].

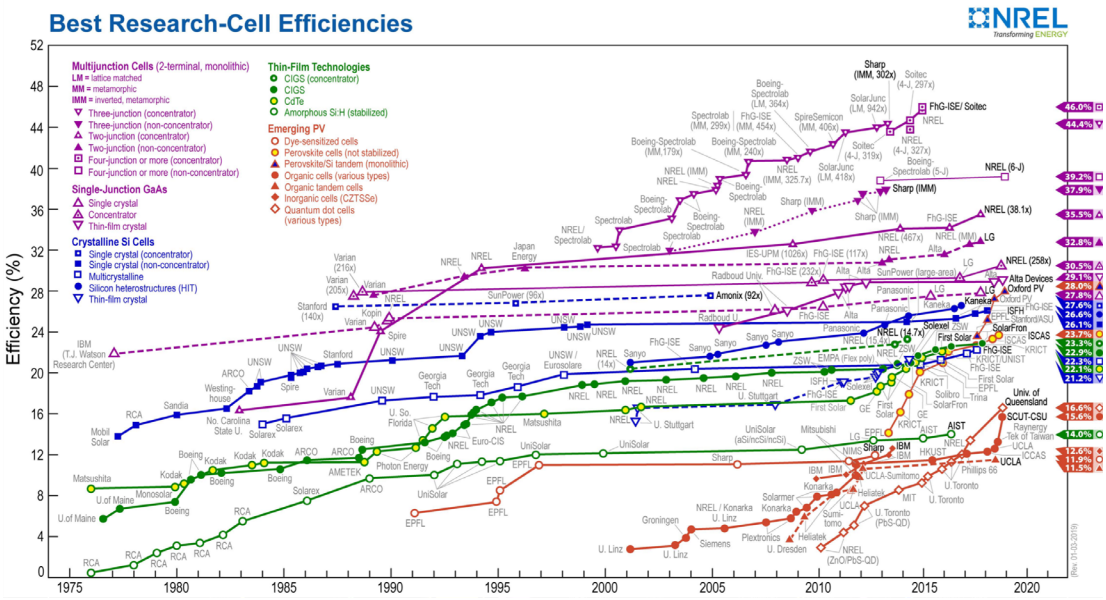

Figure 1.1 Best research-cell efficiencies chart

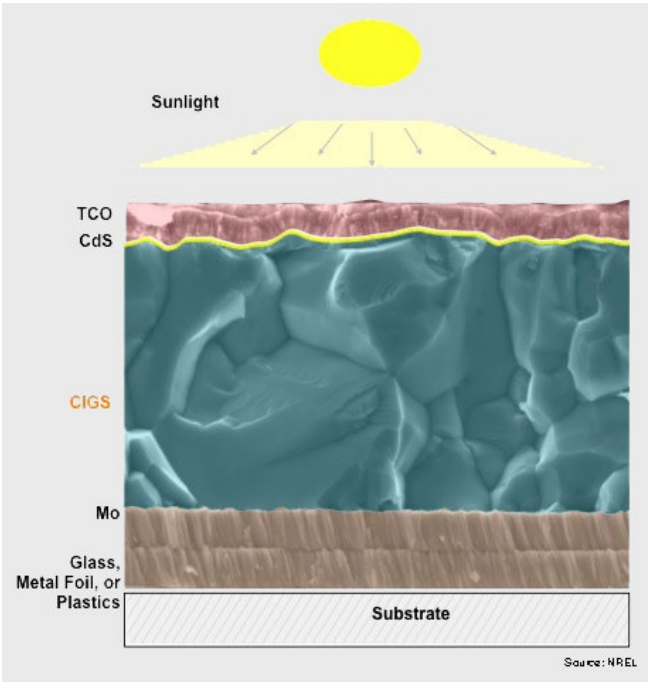

Figure 1.2 Typical structure of CIGS solar cell

A CIGS thin film solar cell typically contains 7 different layers, as shown in Figure 1.2. Each layer has its own function and characteristics as well as process method for fabrication.

The substrate is typically a soda-lime glass (SLG). The benefits of the out-diffused Na ion into the CIGS absorber layer from soda-lime glass is either forming Na_{In} defects or removing mid-gap traps, to increase the electrical conductivity and to reduce the grain boundary energy barrier. However, Na_2Se is believed to cause a poor adhesion between CIGS and Mo. Flexible substrates have been developed recently using polymer and metal foils. Because of their flexibility, potential space or portable applications can be considered. The back contact electrode uses a molybdenum (Mo) layer. Polycrystalline CIGS layer acts as a p-type light absorber, and forms a p-n junction with CdS buffer layer (n-type). The ZnO and AZO bilayer works as a transparent conducting oxide film. Anti-reflection (AR) coating (e.g., MgF_2) is optional, and an optimized AR coating would typically raise the solar efficiency by about 1-2% in absolute efficiency. Lastly, a bi-layer Ni/Al grid is used as a front contact material.

In this part of the thesis, we focus on the two-step fabrication of low bandgap CIS (without Ga) solar cells, which is optimal for fabricating the bottom cell of double-junction tandem thin film solar cell. CIS has a very high optical absorption coefficient, which makes it able to absorb more than 90% of the incident photons with energies higher than 1.04 eV within 1-2 μm thickness. Because of the high absorption coefficient and low bandgap, high quality CIS solar cells can have a very high short circuit current compared with other thin film material or other type of solar

cells. We develop a very simple two-step process based on annealing stacked elemental layers under selenium vapor (selenization) within a graphite box, followed by a Potassium Fluoride (KF) postdeposition treatment (PDT). We are able to reproducibly achieve above 12% conversion efficiency in our CIS cells, with the champion cell exhibiting near-record 14.7% efficiency. This is the best published performance for a CIS solar cell fabricated by the two-step selenization process using a graphite box. This is a low-cost and large-area approach which is highly manufacturable. Precise control of the Cu/In ratio in the precursor ensures that single phase chalcopyrite CIS films with grain size larger than 2 μm are obtained, which is the key for making high efficiency solar cells. KF PDT in Se vapor environment helps form a hole-blocking layer between CdS/CIS interface, which reduces the tunneling recombination and significantly increases the open circuit voltage. Our results indicate that perhaps the CIS system is less sensitive to elaborate processing steps and details than previously thought. This simple approach offers a very useful experimental platform from which to study a variety of thin film PV research topics.

Chapter 2 Material Properties and Formation of CIGS Film

2.1 Material Properties of CIGS Film

$CuInSe_2$ and $CuGaSe_2$ crystallize in a diamond-like lattice structure with a face-centered tetragonal unit cell that is referred to a chalcopyrite structure as shown in Figure 2.1. The CIGS film is a hybrid of $CuInSe_2$ and $CuGaSe_2$, since it is always formed via alternating some In atoms with Ga atoms. So by studying pure $CuInSe_2$, we can understand the properties of CIGS film. Figure 2.1 shows a unit cell of the chalcopyrite lattice structure. Each selenium atom (anion) is surrounded by a tetrahedron of two Cu and two In (Ga) atoms (cations), and each metallic atom (cation) is the center of a tetrahedron of four selenium atoms (anions). Table 2.1 shows typical lattice constants and electrical properties for $CuInSe_2$ and $CuGaSe_2$ films.

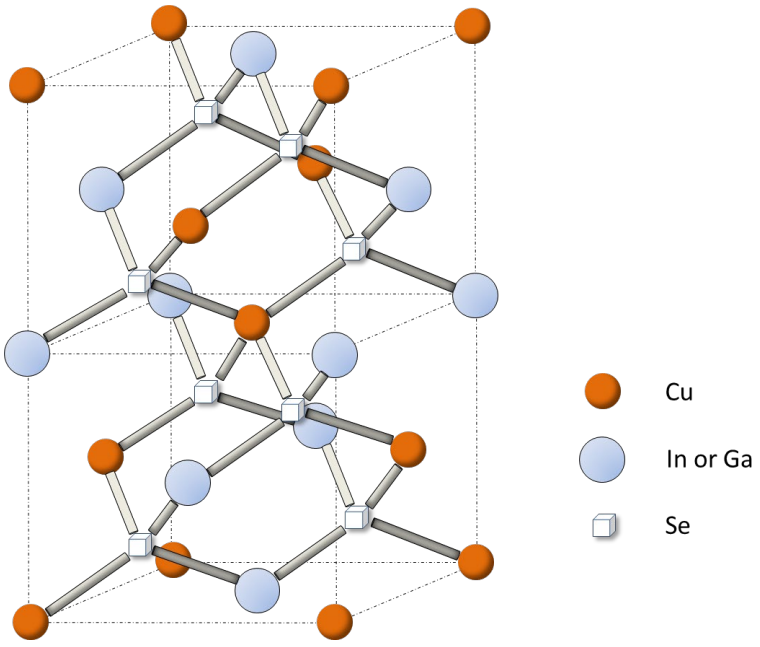

Figure 2.1 Schematic of a tetragonal unit cell of the CIGS chalcopyrite structure

Table 2.1 Typical lattice constants and electrical properties for $CuInSe_2$ and $CuGaSe_2$ films.

	Lattice constants		Band gap energy	Absorption coefficient
	a (nm)	c(nm)	Eg (eV)	α (cm^{-1})
$CuInSe_2$	0.5784	1.1614	1.04	$\sim 1\times10^5$
$CuGaSe_2$	0.5596	1.1002	1.68	$>3\times10^4$

Both $CuInSe_2$ and $CuGaSe_2$ are direct band gap semiconductors. As we can see in Table 2.1, the absorption coefficient for $CuInSe_2$ and $CuGaSe_2$ are very high, larger than 10^4 cm^{-1}. Thus, about 99% of the incoming light will be absorbed within ~ 1μm.

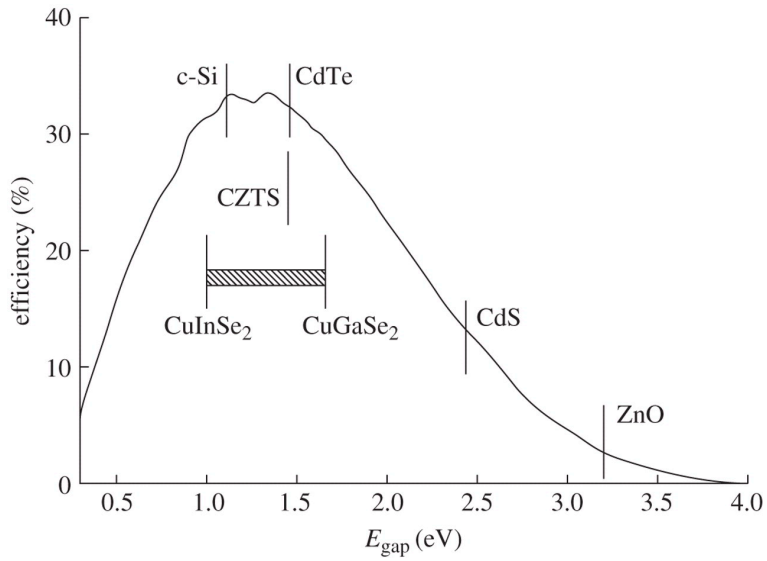

Figure 2.2 Shockley–Queisser limit and adjustable range of band gap of CIGS film.

$CuInSe_2$ and $CuGaSe_2$ have different band gaps. This is how we can control the band gap of CIGS film by varying the Ga content. The band gap $E_g(x)$ of $CuIn_{1-x}Ga_xSe_2$ is given as:

$$\mathrm{E}_g(\mathrm{x}) = 1.040 + 0.626x - 0.167x(1-x) \tag{3.1}$$

The band gap of CIGS film is adjustable within the range from 1.04 eV to 1.68 eV. According to the detailed balance limit model worked out by Shockley–Queisser, the maximum solar conversion efficiency is around 33.7% assuming a single p-n junction with a band gap of 1.34 eV (using an AM 1.5 solar spectrum). So, by substituting part of In by Ga, the band gap of CIGS film can be adjusted to better match the solar spectrum. Figure 2.2 shows the Shockley–Queisser limit and the adjustable range of band gap of CIGS film.

Based on the above theory, one would expect that when Ga/(In+Ga) ratio is 0.545 (the band gap of the absorber is 1.34 eV), the CIGS solar cell could have the highest conversion efficiencies, but this is not the case. In practice, when substituting In by Ga at the beginning, the conversion efficiency increases with the increase of the Ga content until the efficiency reaches a maximum when the Ga/(In+Ga) ratio is about 0.3 (the band gap of the absorber is about 1.19 eV). Beyond that, the efficiency decreases with the increasing of band gap of CIGS film. It seems that the composition of CIGS is optimized by a Ga/(In+Ga) ratio of about 0.3. This is mainly due to the impact of midgap defects and the increase in the interface recombination with increasing Ga content at high Ga/(In+Ga) ratios [3].

Moreover, the band gap profile is one of the most important and thoroughly understood properties of the CIGS layer. The Ga content and therefore the band gap of the absorber can be manipulated to decouple the optical absorption from the voltage, and reduce the effects of back surface recombination and short diffusion length. In general, the band gap is single-graded in such a way that the region toward the back contact of the device has a higher band gap, which enhances the separation of photon-generated charge carriers and reduces the recombination at the back contact and assists in collection [4,5]. On the other hand, double-grading, i.e. a notch profile is created that both increases the band gap toward the back and front of the device, can be done by having a Cu deficient surface layer. This grading toward the front of the device decouples the electrical and optical response.

Besides the optical properties, the electrical properties are also of concern when making CIGS solar cell. Here, we consider two parameters, i.e., the anti-stoichiometry ε and non-molecularity δ parameters, given by:

$$\varepsilon = \frac{2[\mathrm{Se}]}{[Cu]+3[In]} - 1 \tag{2.1}$$

$$\delta = \frac{[Cu]}{[In]} - 1 \tag{2.2}$$

If δ>0 (Cu-rich), the films are likely of p-type conductivity, but Cu_2Se will exist. The films are likely of p-type conductivity, if ε>0 (Se-rich). That is, $CuInSe_2$ and $CuGaSe_2$ with an excess of Cu is always p-type while In-rich (or Ga-rich) films can be either p-type or n-type. Table 2.2 lists some electrical properties of I-III-VI_2 chalcopyrite semiconductors (I = Cu, III = Ga, In and VI = Se). In the absorber layer, p-type CIGS film forms the p-n junction with n-type CdS buffer layer, thus Cu-rich or slightly III-rich material should be deposited. In practice, high-efficient CIGS solar cell requires an overall Cu-deficient composition, with a thin, even more Cu-deficient surface layer. The composition of this surface layer corresponds to the stable ordered vacancy compound (OVC) $Cu(In, Ga)_3Se_5$ [6–8]. The formation of this OVC layer occurs automatically on the top surfaces of slightly Cu-deficient CIGS film at high deposition temperature when Cu/(In+Ga) ratio in the bulk of the film is kept at 0.85~0.95. Thus, there is a significant difference between the bulk and surface compositions. This OVC layer is weakly n-type [8], and because the bulk of the absorber is p-type, they form a buried p-n junction [7–9]. The inverted surface

increases the barrier for recombination at CIGS/CdS interface due to the higher band gap of 1.23-1.3 eV [8,10,11], and is thus the key to high-efficiency solar cells.

Table 2.2 Electrical properties of I-III-VI_2 chalcopyrite semiconductors.

Stoichiometry	Cu-rich	Slightly III-rich	Very III-rich
I/III ratio	> 1	0.85 ~ 0.95	< 0.5
Conductivity	p-type	p-type	n-type
ρ (Ω•cm)	≤ 0.1	10 ~ 20	$> 10^4$
n (cm^{-3})	$> 10^{17}$	$2 \sim 4\times10^{16}$	$10^{14} \sim 10^{15}$
σ ($cm^2V^{-1}S^{-1}$)	15 ~150	15 ~ 150	90 ~ 900

* ρ: resistivity, n: carrier concentration, σ: mobility

A critical issue in CIGS solar cells is whether the grain boundaries (GBs) are active as non-radiative recombination centers, benign or inactive for recombination, or perhaps even beneficial for photovoltaic performance through 3-dimensional minority carrier collection. Until now, the reason and the effect of GBs are not very clear. However, several groups states that surface reconstruction at the GBs of CIGS forms a charge-neutral hole barrier that expels holes and creates a “free zone” for fast electron transport. As we can see in Figure 2.3, in p-type CIGS bulk layer, the positively charged GBs repel holes and attract electrons. This effect reduces non-

radiative recombination at GBs and forms minority-carrier photocurrent collection channels that enhance the device performance [12–27].

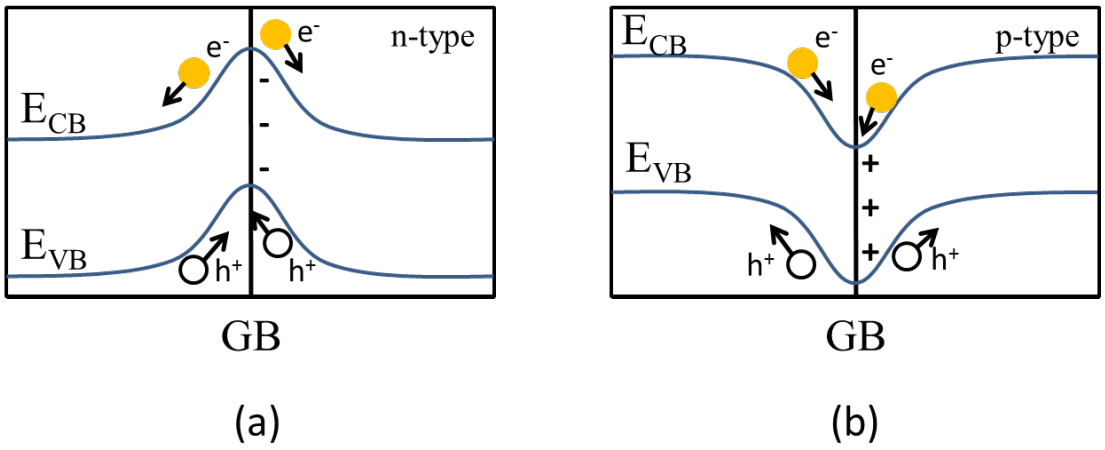

Figure 2.3 Schematic of the band diagram perpendicular to the grain boundary: (a) n-type material, GB screens out electrons (majority), attracts holes (minority); (b) p-type material, GB screens out holes (majority), attracts electrons (minority).

2.2 CIGS Solar Cell Deposition Processes

A wide variety of semiconductor processing methods have been applied to synthesize CIGS compound, but only a few of them were successful in producing a high quality CIGS absorber for thin film photovoltaic cell. Figure 2.4 shows the process flow of the conventional CIGS module preparation process. To develop the most promising technique for the commercial manufacture of solar cells, the most important criteria are that the deposition can be completed at low cost while maintaining high deposition rate with high yield and reproducibility. To achieve high yield and reproducibility, control of the compositional uniformity over large areas is critical.

Among all layers, the formation of CIGS absorber is the key process. CIGS layer should be at least 1 μm thick, and the relative compositions of the constituents should be kept within the bounds determined by the phase diagram, see Figure 2.5.

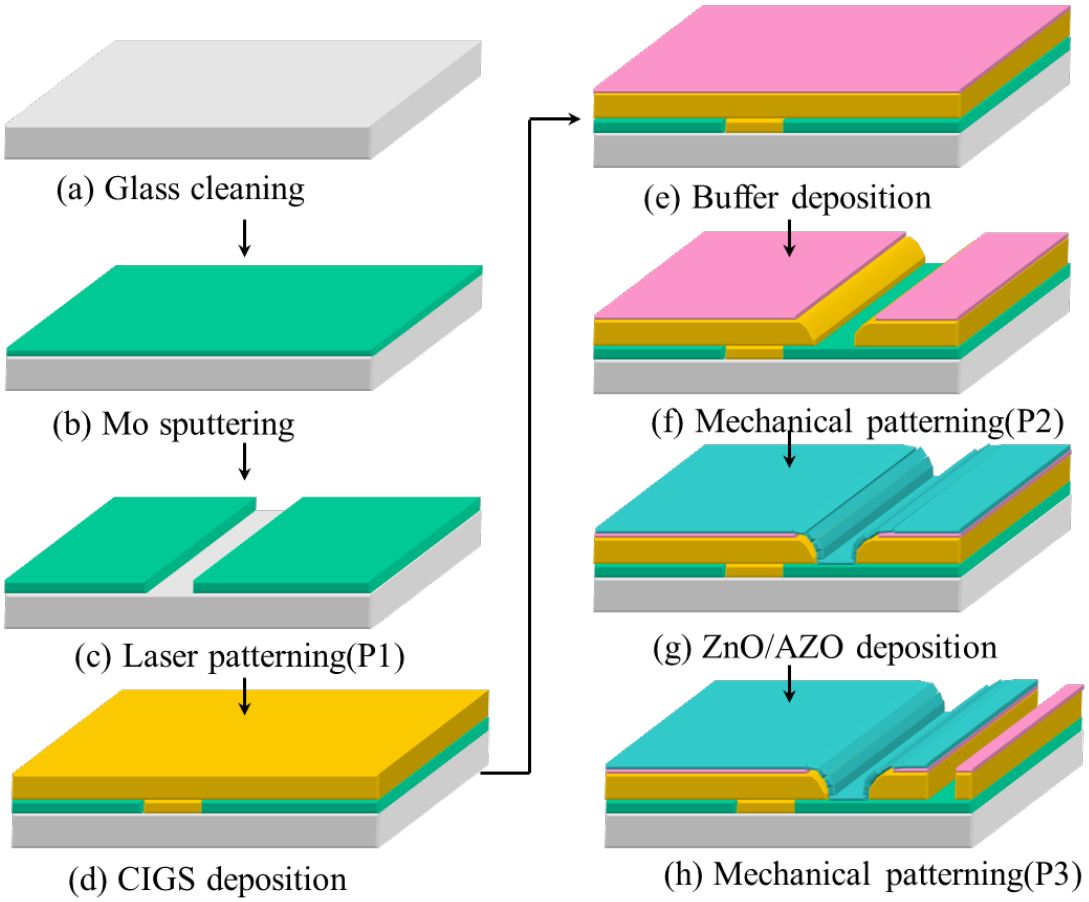

Figure 2.4 Process Flow of CIGS Module Production

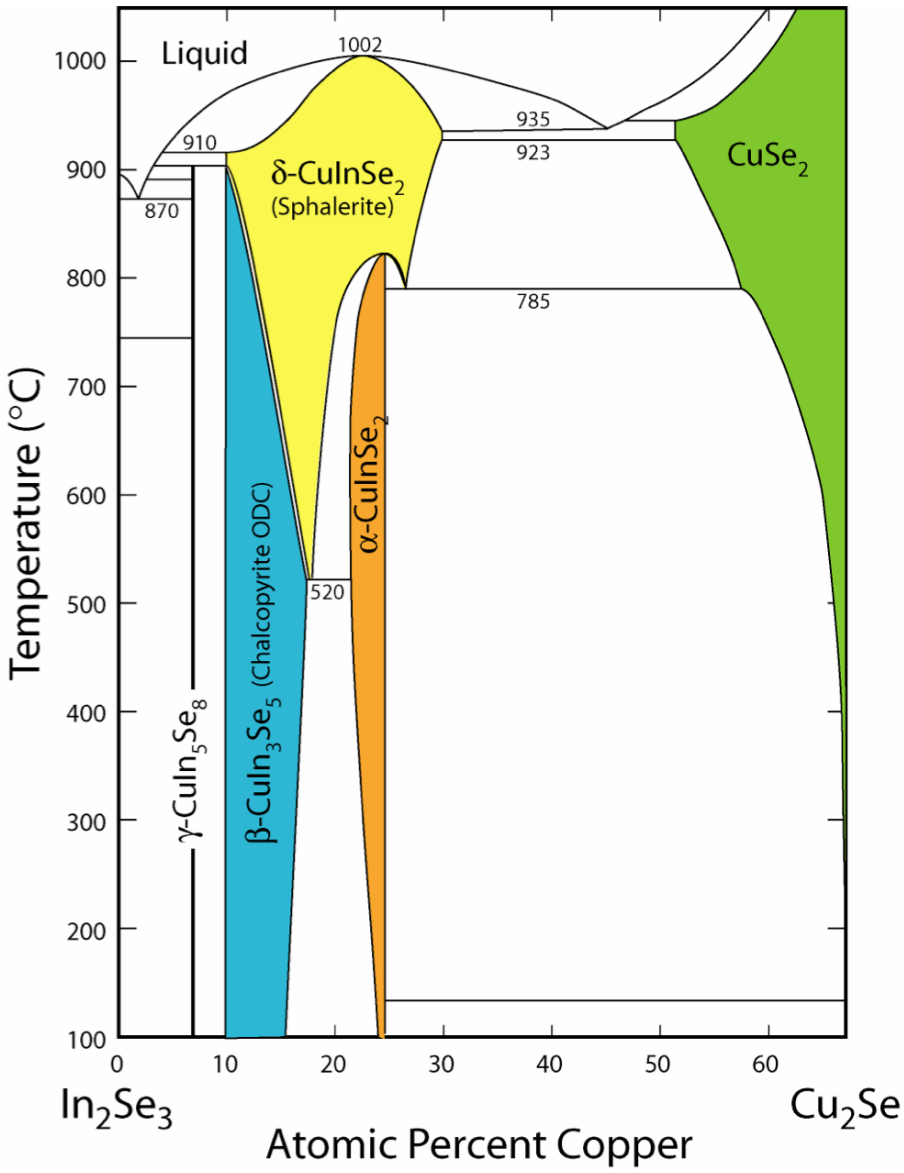

Figure 2.5 Phase diagram of CIS. α-phase ($CuInSe_2$) is the most relevant phase for the application in solar cells; β-phase ($CuIn_3Se_5$) & γ-phase ($CuIn_5Se_8$) are defect phases built by ordered arrays of defect pairs; δ-phase ($CuInSe_2$) is a high temperature phase.

The most promising deposition methods can be divided into two general approaches that have both been used to demonstrate high device efficiencies. One is called co-evaporation approach. Historically, CIGS solar cells fabricated by the three-stage co-

evaporation process developed at the National Renewable Energy Laboratory [28] set the record. To pursue a low-cost and large-area approach with high yield and reproducibility for depositing CIS absorber layer, another approach, that is a two-step selenization (annealing) process, was developed [29,30]. In fact, Solar Frontier is the worldwide frontrunner with a 22.3% efficiency obtained by using a two-step sputtering-selenization formation method [2].

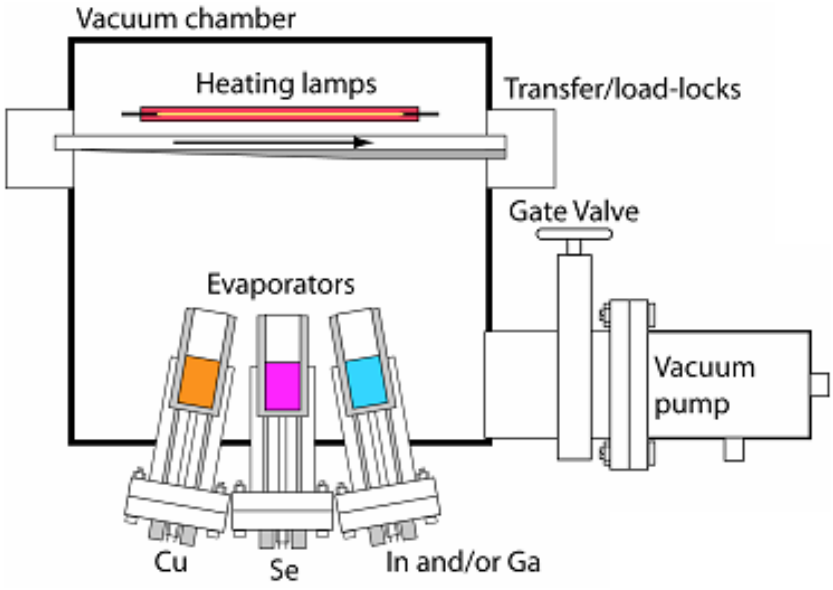

Figure 2.6 Schematic of the vacuum chamber used in co-evaporation process of CIGS films.

The three-stage co-evaporation process is characterized by simultaneous exposure of high-temperature substrate to Cu, Ga, In and Se vapor fluxes, as illustrated in Figure 2.6. The elements of Cu, In, Ga and Se are loaded into the effusion cells or open-boat

sources and heated up to over 1300 °C for Cu, 1100 °C for In, 1200 °C for Ga and 350 °C for Se to produce respective molecular beams of the elements which are directed towards the heated rotating substrate. The primary advantage of this method is that the composition of the elements and band gap can be controlled by precisely varying the effusion cell temperature which determines the element fluxes at any time during the deposition process. The CIGS devices with the efficiency of 22.0% have been fabricated by this method [1].

The schematic diagram of the typical three-stage co-evaporation process is illustrated in Figure 2.7. In the three-stage process, the sequence is In-Ga-Se deposition, Cu-Se deposition, and again In-Ga-Se deposition. During the first stage, the substrate temperature is set to be 350~400 °C, and In, Ga and Se are deposited to form the sesquiselenide, $(In, Ga)_2Se_3$. Only in the second stage, the Cu is supplied and the film is Cu-rich. In this period, where Cu is diffusing into the $(In, Ga)_2Se_3$ prepared in the first stage, a Cu-rich CIGS is produced along with a secondary Cu-Se binary compound (Cu_2Se), and grain growth takes place by recrystallization. The larger grain size in Cu-rich film (> 1μm) has been explained by the presence of the binary $Cu_{2-x}Se$ phase which segregates during growth of a Cu-rich CIGS film [31]. $Cu_{2-x}Se$ forms a quasi-liquid surface layer and leads to a liquid-solid type growth. In the third stage, a slightly Cu-deficient CIGS forms by adding more $(In, Ga)_2Se_3$.

The three-stage process, however, has limitations in industrial large-area module production mainly due to high production cost caused by high-vacuum and high-temperature operation conditions. Furthermore, co-deposition technique has a limitation in achieving uniformity in large scale deposition.

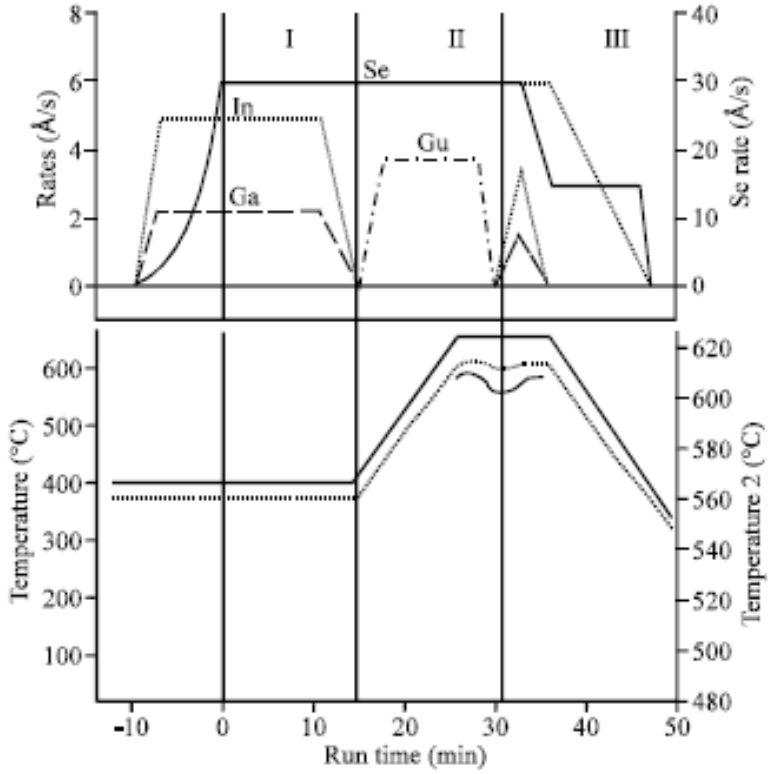

Figure 2.7 Schematic diagram of the typical three-stage co-evaporation process [32].

The second common approach to produce a device-quality CIGS absorber is usually referred to as two-step selenization (annealing) process. The two-step process consists of the deposition of a stack of metallic precursor layers followed by subsequent selenization. Traditionally, the metal precursors are prepared by sputtering and then selenized at high temperature (>550 °C) in a reactive H_2Se or Se vapor ambient, as shown in Figure 2.8. The metallic precursor is used to determine the final composition of the film and to ensure spatial uniformity. The Cu/(Ga+In) and the Ga/(Ga+In) ration of the final CIGS film are mostly given by the thicknesses of the precursor layers and thus can be sufficiently controlled by Energy-dispersive X-ray spectroscopy (EDS). Moreover, sputtering is an attractive process because it is easily

scalable using commercially available deposition equipment and can provide good uniformity over large areas with high deposition rates.

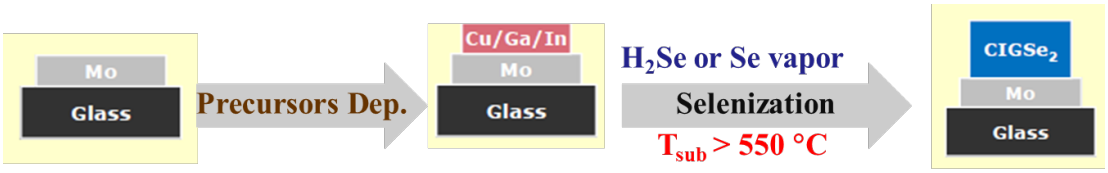

Figure 2.8 Schematic diagram of the two-step selenization process for CIGS fabrication.

Selenium can be supplied by different ways at the reaction step in the two-step selenization. Typically, Se vapor or H_2Se/Ar atmosphere is provided to form the CIGS film. However, since Se vapor and H_2Se gas are toxic, some safer selenization methods have been proposed. Rapid thermal annealing (RTA) of stacked elemental layer, where Se is evaporated on top of the precursor stack, has been suggested by Palm *et al* [33]. As a novel CIS process, Bindu *et al*. deposited Se film on a glass substrate using chemical bath deposition (CBD) at room temperature, totally avoiding using of H_2Se or Se vapor [34]. Indium and copper were then deposited on the selenium layer to yield glass/Se/In/Cu or glass/Se/Cu/In precursor by sequential vacuum evaporation. Finally, the stacked layer precursor was thermally annealed in high vacuum at the temperature range 150 °C to 400 °C.

In recent years, the introduction of alkali metal element postdeposition treatment (PDT) of CIGS films, including Sodium Fluoride (NaF) PDT, Potassium Fluoride (KF) PDT, Rubidium Fluoride (RbF) PDT, Caesium Fluoride (CsF) PDT and etc., has led to the achievement of several consecutive new world record efficiencies up to

22.3% for the CIGS solar cell technology. Both approaches, three-stage co-evaporation process [1] and two-step selenization process [2], take advantage of Alkali PDT and have demonstrated efficiency above 22%. In spite of different growth methods of the CIGS absorber layer, several groups observed the beneficial effect of the Alkali PDT. Addition of alkali elements to the CIGS material is beneficial for the cell performance, mainly due to an increase of the p-type conductivity and the passivation of compensating defects [35–37].

After reviewing these two major process methods, we found out that the following requirements are necessary for both to achieve high performance solar cells:

1. The reaction temperature should reach above 500 °C.
2. The composition should be controlled to form a Cu-poor surface.
3. An oversupply of Selenium during the process should be provided.
4. Alkali PDT should be applied.

Besides these two popular approaches, several more cost effective processes, based on low temperature and non-vacuum technique, have been developed to help commercialize the CIGS thin film solar cells. One example approach is electrodeposition, which has been considered as a suitable process for large-scale industrial processes, requiring low energy consumption and low capital investment [38,39]. There are two major methods of electrodeposition that have been explored. One method includes co-deposition of all elements [40–42], while the other implements selenization of pre-deposited metallic precursors [43,44]. Fundamentally, electrodeposition of Cu-In-Ga-Se alloys is carried out

potentiostatically on Mo-coated substrates from aqueous chemical solutions containing complex agents, e.g., CuCl, $InCl_3$, $Ga(NO_3)_3 \cdot 7H_2O$, H_2SeO_3 and KSCN [42,44]. Solar cells with efficiency of 15.4% were fabricated by electrodeposition of quaternary CIGS followed by subsequent thermal annealing [39]. The stability of the solution, high deposition rate and large area non-uniformity remain a significant challenge [45].

Another interesting non-vacuum process for low cost mass production for CIGS solar cells is Screen printing. A 'knife blade' coating technique is used to coat a water based precursor ink on glass/Mo substrate [46], which leaves a layer of mixed oxides with a typical thickness of around 2.5~3.0 μm on the substrate after drying. This oxide layer is converted to a layer of metal alloys of Cu-Ga-In under a forming gas mixture of H_2 and N_2 at temperatures in the range 475 °C to 525 °C. Finally, this alloy coating is selenized in H_2Se gas ambient in the range 440 °C to 475 °C to form CIGS layer. An efficiency of ~ 13% was reported by this process. The main advantages of this non-vacuum process include high compositional control of the absorber layer, high material utilization and low cost.

Spray deposition has also been taken into account as a possible non-vacuum technique that is amenable to the manufacture of large area films with low processing costs. Schulz et al. has employed nanoparticle-based precursors for spray deposition of CIGS materials [47]. In their approach, nanoparticle colloids were prepared by reacting a mixture of CuI and/or $[Cu(CH_3CN)_4](BF_4)_2$ and/or InI_3 and/or GaI_3 in pyridine with Na_2Se in methanol at reduced temperature under inert atmosphere.

Colloids with the compositions $CuInSe_{2.5}$, CuSe, In_2Se_3 and $Cu_{1.10}$ $In_{0.68}Ga_{0.23}Se_x$ were prepared by each corresponding reaction.

Chapter 3 Experimental Details

In this study, we will mainly focus on the fabrication and characterization of $CuInSe_2$ (CIS), since it is a perfect candidate as a bottom cell in a two-junction tandem solar cell. In this chapter, the fabrication procedure of CIS solar cells will be introduced.

Our CIS thin film solar cells are fabricated by using a 2-step sequential process, and is based on annealing and selenization of Stacked Elemental Layers (SEL) using a partially closed graphite box (Figure. 3.1) under Se vapor. Cu and In are sequentially deposited by sputtering to form the SEL (see Figure. 3.2). Sputtering can be easily applied to fabricate larger devices due to its high manufacturability. The SEL is then selenized in a Se vapor and converted to a CIS film in an optimized thermal process. Heterojunction devices using the structure ZnO/CdS/CuInSe2 were fabricated.

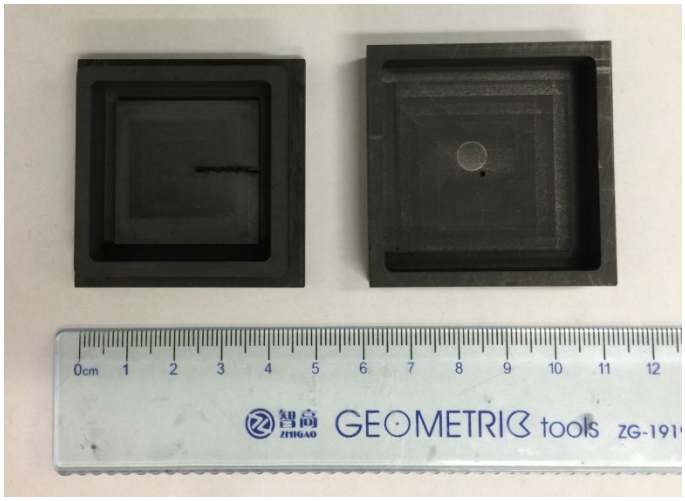

Figure 3.1 Picture of real graphite box, left is the bottom part, right is the cover.

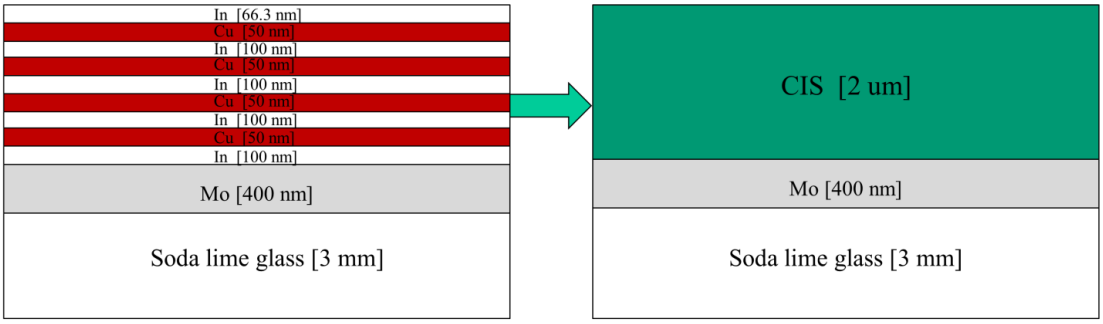

Figure 3.2 Formation of CIS absorber layer by selenization of SELs.

3.1 Substrate and Mo Back Contact Preparation

The substrate used in this work is a commercially available soda-lime glass (3 mm thick) [EcoGuard Mo, Molybdenum Conductive Glass] coated with 0.4 microns of molybdenum which is manufactured by Guardian. The sheet resistance of the Mo layer is 0.55 Ω/square, and the resistivity is about 15-22 μΩ·cm. The substrate was cleaved into 1.5 cm square pieces. To clean organic and inorganic impurities that exist on the surface, each sample is cleaned with acetone, methanol, 2-propanol and finally cleaned in an ultrasonic bath prior to the precursor deposition.

3.2 CIS Precursor Deposition

The CIS precursor layer was deposited by DC magnetron sputtering of Cu and In in an AJA sputtering reactor with base pressure of 1×10^{-6} Torr. The sputter system can hold up to three targets, so the precursor can be deposited without breaking vacuum. The sputtering parameters are listed in Table 3.1.

Table 3.1 Sputtering parameters of Cu and In layer.

	Cu	In
Substrate temperature	R.T.	R.T.
Argon pressure	6×10^{-3} Torr	6×10^{-3} Torr
Argon flow rate	20 sccm	20 sccm
RF power	4.39 W/cm^2	1.32 W/cm^2
Base pressure	1×10^{-6} Torr	1×10^{-6} Torr
Deposition rate	2 Å/s	1.2 Å/s

To further form a slightly In-rich CIS film with atomic Cu/In ratio of 0.95, the precursor was deposited by the sequence of 100 nm In/ 50 nm Cu/ 100 nm In/ 50 nm Cu/ 100 nm In/ 50 nm Cu/ 100 nm In/ 50 nm Cu /66.3 nm In, see Figure 3.2. Here, the thickness of each Cu and In layer were varied by accurately controlling the sputtering time. Prior to the optimization of the metallic precursor deposition, the deposited Cu and In films with different thicknesses were first investigated. Subsequently the optimization process of the precursor was performed. Both methods of cross-section scanning electron microscopy (SEM) and thickness determined by profilometry have been used to achieve the accurate control of the thickness.

Table 3.2 Properties of Cu, In and Se.

	Standard atomic weight	Density ($g \cdot cm^{-3}$)
Cu	63.546	8.96
In	114.818	7.31
Se	78.96	4.81

To form the correct atomic ratio, a calculation of the layer thicknesses is performed. Table 3.2 lists the properties of Cu, In and Se that is required to calculate the relationship between atomic ratio and layer thickness. As mentioned in chapter 2, the anti-stoichiometry ε and non-molecularity δ are two parameters to determine the electrical properties of CIS film,

$$\varepsilon = \frac{2[\mathrm{Se}]}{[Cu]+3[In]} - 1 \tag{3.1}$$

$$\delta = \frac{[Cu]}{[In]} - 1 \tag{3.2}$$

Since in the metallic precursor, the areas of different metal layers are the same, the ratio of thickness can represent the ratio of volume. Then, the atomic ratio is easily calculated as follow,

$$\frac{[Cu]}{[In]} = \frac{t_{Cu} \times \rho_{Cu} \div w_{Cu}}{t_{In} \times \rho_{In} \div w_{In}} \approx 2.2147 \frac{t_{Cu}}{t_{In}} \tag{3.3}$$

$$\frac{2[Se]}{[Cu]+3[In]} = \frac{2(t_{Se} \times \rho_{Se} \div w_{Se})}{(t_{Cu} \times \rho_{Cu} \div w_{Cu}) + 3(t_{In} \times \rho_{In} \div w_{In})} = \frac{1.2183 t_{Se}}{1.4100 t_{Cu} + 0.6366 t_{In}} \tag{3.4}$$

where t is the thickness, ρ is the density, w is the standard atomic weight. Based on equation (3.3), to form a slightly In-rich CIS film with atomic Cu/In ratio of 0.95, a Cu/In thickness ratio of 0.4290 is required. Also, according to the experimental results, the final thickness of the CIS absorber layer is about 3 times the thickness of the metallic precursor. Combining both information, to form a 2-μm CIS absorber layer, a total thickness of 200 nm and 466.3 nm is required for Cu and In respectively.

3.3 CIS Absorber Selenization

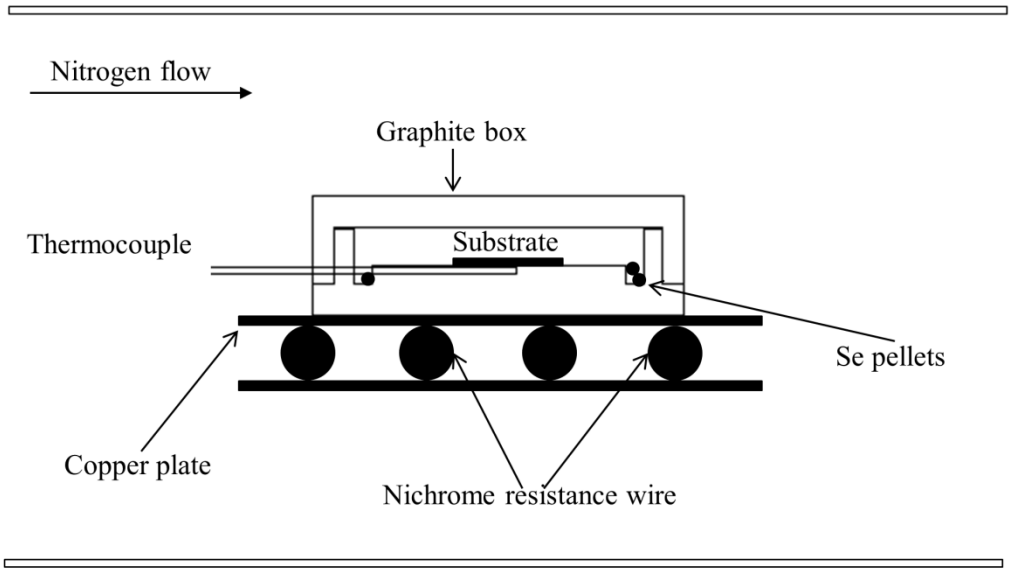

Figure 3.3 Schematic representation of the selenization oven.

The following selenization is the most important step to obtain p-type CIS films. After sputtering the metallic precursor, the sample was carefully removed from the sputtering chamber, and then was put at the center of the graphite box (see Figure. 3.3). Selenium pellets were put in the bottom of the box. The temperature of the sample was controlled by a type K thermocouple, which is in direct contact to the back of the sample (glass side). The distance between the top lid and the sample surface is 3 mm. The designed short distance is to maintain the high Se vapor pressure. The graphite box was put inside a home-made oven, which uses nichrome resistance wire to heat. Pure nitrogen was purged into the system at a slow flow rate for 5 min after the graphite box was placed in the furnace and before the selenization started.

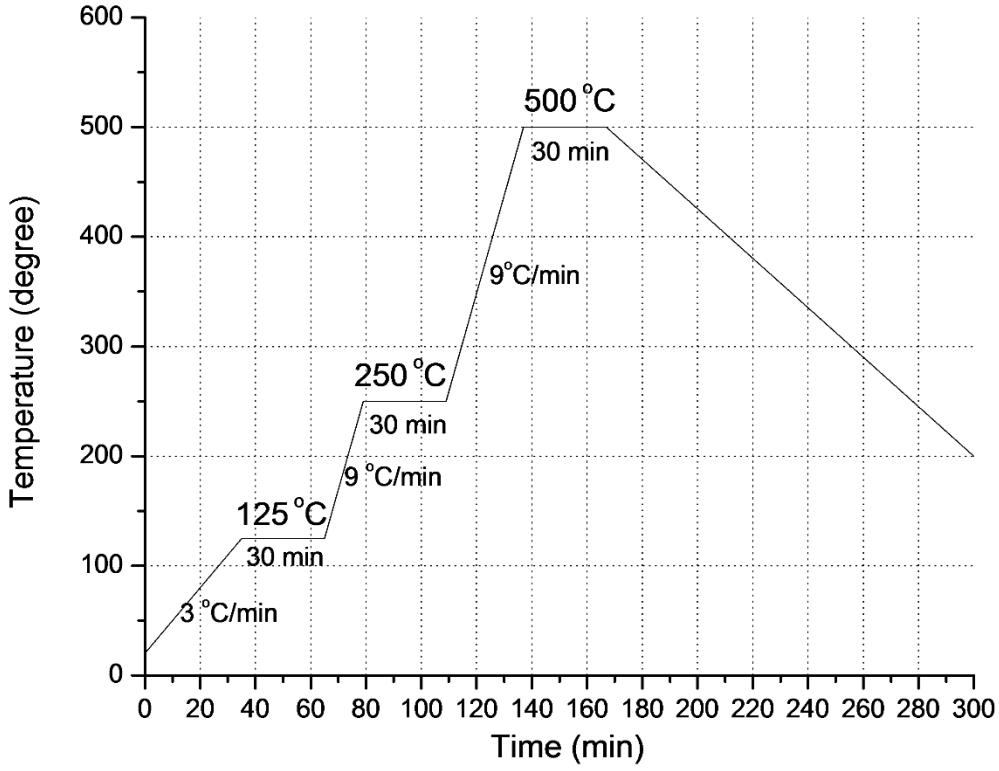

Figure 3.4 Three-step selenization temperature profile.

Figure 3.4 shows the temperature profile for the general selenization process. It is a three-stage annealing step. It starts by increasing the temperature of the oven from room-temperature to 125 °C at a rate of 3 °C/min and by keeping the temperature at 125 °C for 30 min. Then the graphite box is heated up to 250 °C at a rate of 9 °C/min and then the temperature stays at 250 °C for another 30 min. Finally the temperature is increased to 500 °C at a rate of 9 °C/min and is held there for 30 min. After the end of the selenization process, the furnace cools down by itself. The reason for using 125 °C is to make the stacked metal layers diffuse into each other. Then, the Se was evaporated and made to react with the Cu and In films at 250 °C to form Cu-Se and

In-Se compound. The CIS film was formed from melting the Cu-Se and In-Se films and recrystallizing the resulting film at 500 °C.

3.4 KF PDT

The Metra thermal evaporator was used to deposit KF on CIS surface by using resistance heating. The evaporation parameters are listed in Table 3.3.

.

Table 3.3 Thermal evaporation parameters of KF.

Parameter	Value
Substrate temperature	R.T.
Base pressure	1×10^{-6} Torr
Current	125 A
Voltage	80 V
Deposition rate	1 Å/s

20 nm KF thin layer is evaporated on the surface of CIS absorber layer. Immediately after the evaporation of KF layer, it is necessary to rinse the sample with DI water. Details will be explained in the next chapter. Finally, the sample is annealed at 350 °C for 20min within a Se vapor environment in a graphite box.

3.5 Buffer Layer Deposition

About 600 Å CdS layer is deposited by chemical bath deposition (CBD) in an alkaline aqueous solution. The solvents are 0.015 M cadmium sulfate ($CdSO_4$), 1.5 M Thiourea (NH_2CSNH_2), 14.8 N, 28-30% Ammonia (NH_4OH). The molecular weight of $CdSO_4.8/3\ H_2O$ is 256.46 g/mol. To make 500 mL of 0.015 M solution, 1.923 g is weighed and transferred into a beaker, and then diluted with 500 mL DI water. The molecular weight of NH_2CSNH_2 is 76.12 g/mol. Similarly, to make 500 mL of 1.5 M solution, 57.09 g is weighed and diluted with 500 mL DI water. It is important to stir the solution for 30 min and use a 0.2 μm tissue culture filter unit to filter the solution, because the Thiourea does not dissolve quickly and it does contain foreign matter that is not dissolved.

Table 3.4 listed the respective chemicals volume required to make a solution and their mother solution concentration.

Table 3.4 Details of chemical solutions used in the CdS buffer layer deposition.

Chemical	Volume	Concentration
$CdSO_4$	25 mL	0.015 M
NH_2CSNH_2	12.5 mL	1.5 M
NH_4OH	31.25 mL	7.5 M
DI H_2O	183 mL	-

The bath water temperature was 65 °C. The reaction time was 14 min and the stirrer speed was 80 rpm. To avoid yellow foreign particles, samples were squirted with DI water when they were pulled out of the solution. The detailed procedure for CBD-CdS buffer is shown in Figure 3.5. Figure 3.6 shows the Teflon sample holder we have made to hold the four samples. The samples can be spaced evenly around the holder and the magnetic stirring rod can be put inside the center hollow part.

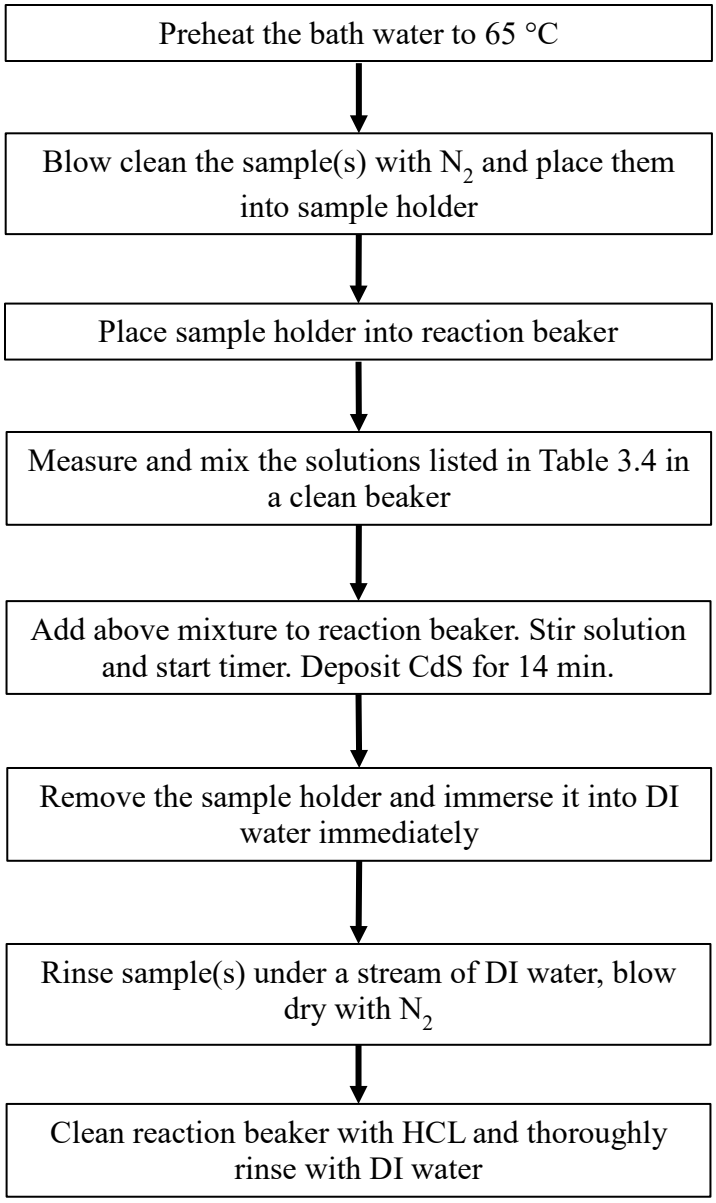

Figure 3.5 Procedure of the CBD-CdS buffer layer.

Figure 3.6 Teflon sample holder for CBD

There are a couple of things that needs to be pointed out. The CdS films do not stick to glass. But they will stick to Mo or CIS surface. The process time drifts a bit depending on the age of the Thiourea, ambient temperature, etc. We monitored the thickness in real time by the apparent color of the CdS on Mo. It is not actually the color of the CdS, but the apparent color due to the thin film interference pattern. As approaching the end of the process time, the apparent color on the Mo went from brown, to purple, to deep blue, to blue-green. Blue (about 600 Å) is ideal. Purple (about 500 Å) is good unless you have a very rough CIS layer underneath, in which case you may see some voltage loss due to incomplete coverage. Blue-green (700 Å and up) is safe, and there will be no voltage loss, but it will lose more current in the CdS.

3.6 Window Layers Deposition

To create the transparent conductive oxidization (TCO) layer, 80 nm i-ZnO and 120 nm ZnO:Al are deposited by RF sputtering. The RF sputtering of i-ZnO can reduce damage and protect the CdS buffer layer. The substrate is heated up to 150 °C. Then the base pressure is pumped down to about $2\text{-}4\times10^{-7}$ Torr. This is critical since the quality of ZnO layer is sensitive to the oxygen content inside the chamber. The target-to-substrate distance was kept at 63 cm. The sputtering parameters are listed in Table 3.5.

Table 3.5 Sputtering parameters of i-ZnO and ZnO:Al layer.

	i-ZnO	ZnO:Al
Substrate temperature	150 °C	150 °C
Argon pressure	2×10^{-3} Torr	2×10^{-3} Torr
Argon flow rate	20 sccm	20 sccm
RF power	2.19 W/cm^2	2.63 W/cm^2
Base pressure	$2\text{-}4\times10^{-7}$ Torr	$2\text{-}4\times10^{-7}$ Torr
Deposition rate	5.3 nm/min	5 nm/min
Resistivity	4.5×10^{5} Ω·cm	5×10^{-3} Ω·cm

3.7 Top Contact Layers Deposition and Device Isolation

Finally, 50 nm Ni and 1.3 μm Al layers are deposited by e-beam evaporation as the top metal contact.

In this study, all CIS devices are fabricated on 1.5 cm x 1.5 cm substrate (see Figure 3.7). To electrically isolate the 9 devices on each of the 1.5 cm x 1.5 cm samples, I used a sharp razor blade to define each individual device. The electrode pattern for each device consists of 3 equally spaced fingers of 0.1 mm in width and 1.1 mm in length separated by 0.65 mm with a 0.8 mm x 0.8 mm contact pad.

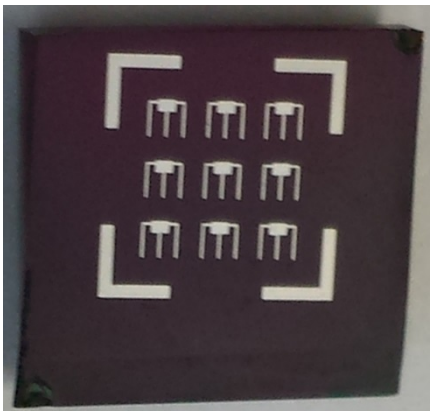

Figure 3.7 Picture of one 1.5 cm x 1.5 cm sample with 9 devices in it.

3.8 Characterization Methods

Various analysis tools were used to study the property and measure the performance of CIS solar cells in this study. Scanning electron microscopy (SEM) was used to investigate the morphological feature of various thin films, like the top-view and

cross-sectional images of CIS layer, the top-view of i-ZnO and ZnO:Al layers, and etc. Energy-dispersive X-ray spectroscopy (EDS) is one of the most common used technologies for the chemical analysis of thin films. It was used to analyze the atomic ratio in metallic precursor and selenized CIS absorber layer. X-ray diffraction (XRD) is a standard technique for the determination of the crystal structure of the samples. By studying XRD spectrum, different compound phase will be pointed out, which indicates the quality of the tested samples. Hall-effect measurement is a technique used to measure the amount and type of carriers present in a semiconductor. The four-point probe setup is used to measure the sheet resistivity of i-ZnO and ZnO:Al layers. External quantum efficiency (EQE) is the ratio of the number of charge carriers collected by the solar cell to the number of photons of a given energy shining on the solar cell from outside (incident photons). It was measured over a range of different wavelengths to characterize a solar cell's performance at each photon energy level. Current-voltage (I-V) characteristics of CIS solar cells were recorded both under one-sun illumination and without any illumination. From the measured I-V curve, the fill factor FF, open-circuit voltage V_{oc}, short-circuit current I_{sc}, efficiency η and many other parameters can be extracted.

Chapter 4 Results and Discussion

In this chapter, we focused on an interesting set of relationships between the processing parameters and different device figures of merit. For example, the following sections examined the effect of the annealing temperature profile on the grain size, pore (or pinhole) density, and analysis of current voltage curve, including reverse saturation current, series resistance and shunt resistance.

4.1 Optimization of Metallic Precursor

Fabrication of the CIS absorber layer is a key process. Both precursor and selenization have a direct effect on the properties of the final CIS absorber, such as stoichiometry, morphology, and electrical properties. In the deposition of the metallic precursor, the most important part is the precise control of the atomic element ratio, which directly determines the properties of the CIS semiconductor. As calculated in section 3.2, there is a relationship between the thickness ratio and the atomic ratio of each element, so, to form a CIS absorber layer with the desired atomic ratio, accurate control of the thickness of each layer must be achieved. Here we did not change any parameters of the sputtering condition, like deposition power density, Argon pressure and etc., since the only properties of interest are the thickness and the uniformity. The metal was sputtered from a metal target, not a compound or alloy target. So there is no need to investigate the composition of the deposited films. All the sputtering parameters were listed in section 3.2, Table 3.1.

The thicknesses of the Cu and In films were analyzed by both methods of cross-sectional SEM and profilometry. Firstly, the Cu films were deposited using DC sputtering method on the SLG substrate. The thickness of Cu film was measured in multi points. As we can see in Figure 4.1, a very uniform Cu layer was deposited, up to 400 nm. The measured results from profilometry highly agree with the SEM results. Excellent control of the Cu film thickness was achieved.

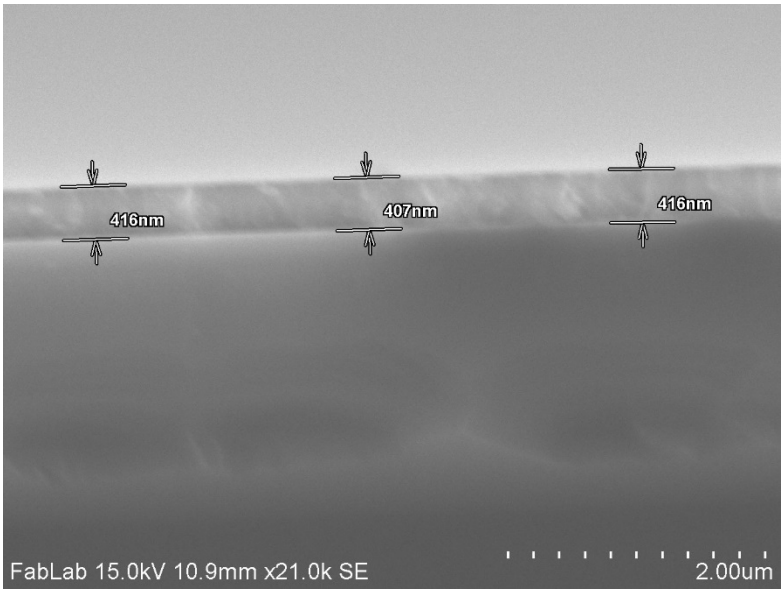

Figure 4.1 Cross-sectional SEM image of Cu film.

In addition, the In film deposited on the SLG substrate was also investigated. Here, the In films with different thickness between 50 nm to 500 nm were deposited. Figure 4.2 shows the top-view SEM images. It is obvious that segregation and agglomeration of In occurs in the deposition. The fact that In has a high diffusion coefficient and low melting points cause the formation of hillocks. Then, these discontinuous hillocks attached to the substrate surface and formed a film. As more In particles are deposited

on the substrate, these In hillocks gradually become bigger. These hillocks cause rough surface of metallic precursor and CIGS absorber. And they also cause the formation of the voids at the interface of CIS/Mo. In order to obtain a smoother metallic precursor and CIS absorber, the large In hillocks should be avoided.

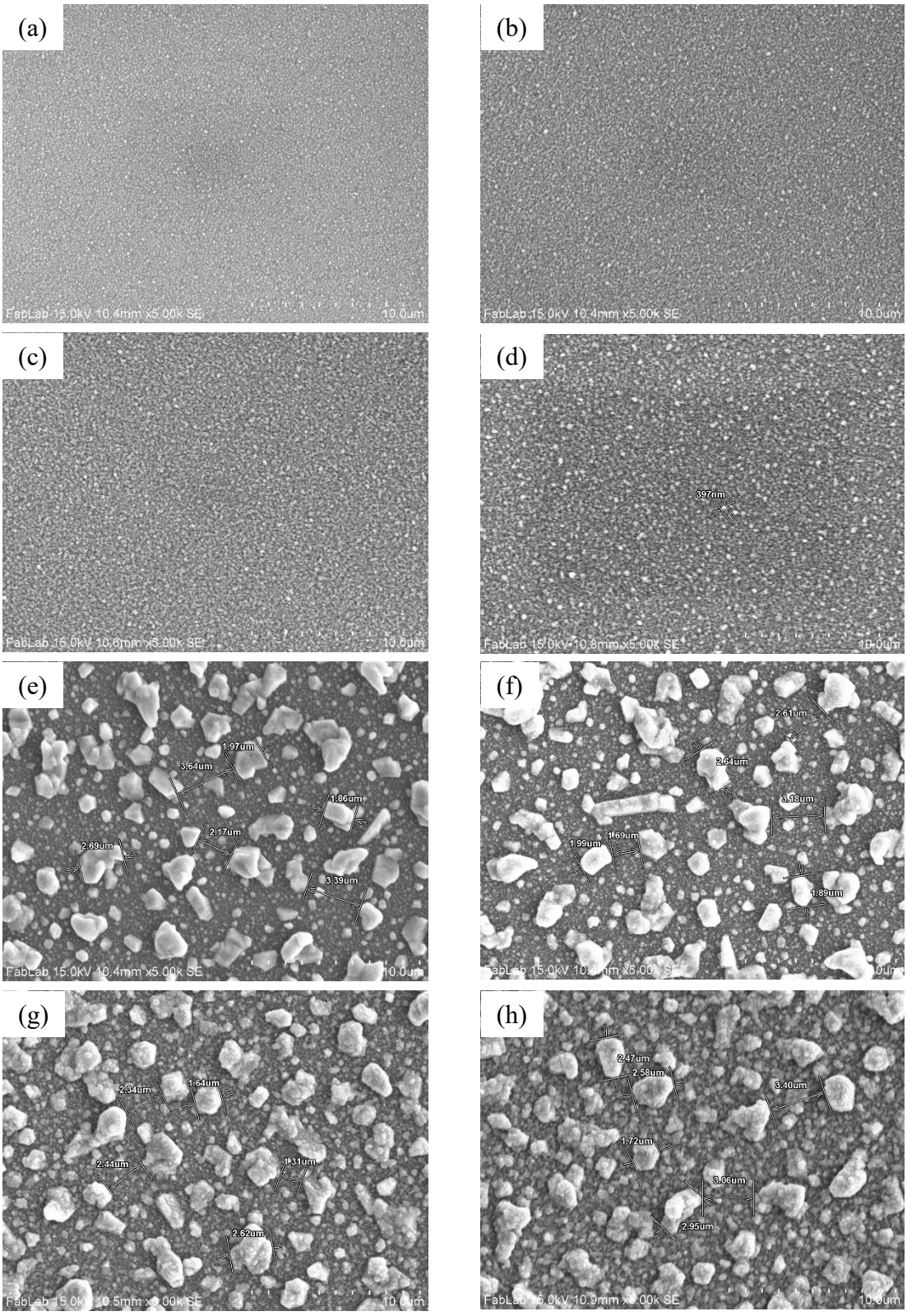

Figure 4.2 Top-view SEM images of In films with different thickness: (a) 50 nm, (b) 100 nm, (c) 150 nm, (d) 200 nm, (e) 250 nm, (f) 300nm, (g) 400 nm, (f) 500 nm.

As we could see from Figure 4.2, films that are less than 200 nm had much smaller hillocks than those thicker ones. The cross-sectional SEM image of a 200-nm In film was shown in Figure 4.3. Smooth surface and accurate control of thickness was achieved here.

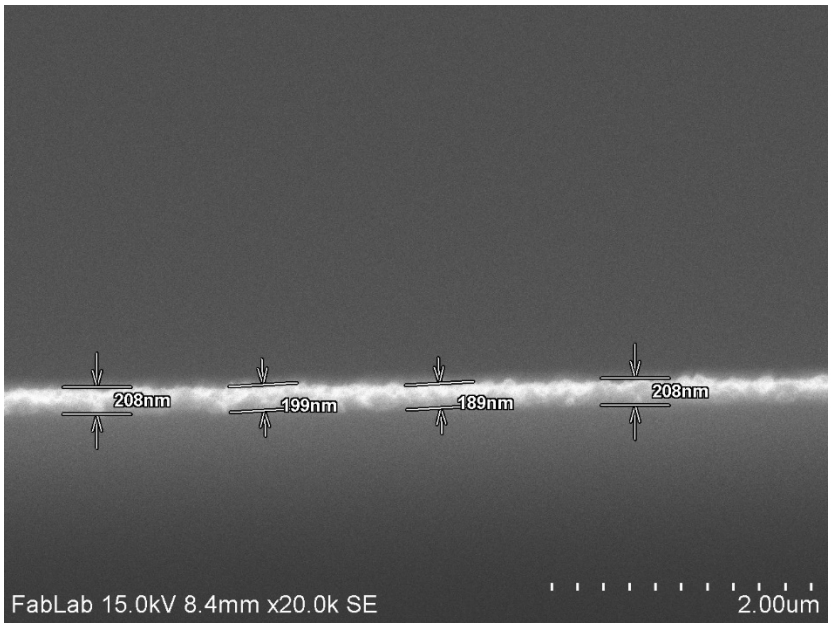

Figure 4.3 Cross-sectional SEM images of In film.

Now, thickness of both Cu and In films was precisely controlled. In order to obtain the high efficient CIS solar cell, the next step is to vary the Cu/In thickness ratio, which controls the chemical composition of the CIS absorber layer. Figure 4.4 showed the schematic of the metallic precursor. The thickness of each layer depends on the different thickness ratios. As calculated in section 3.2, the relationship between the thickness ratio and atomic ratio of Cu and In is,

$$\frac{[Cu]}{[In]} = \frac{t_{Cu} \times \rho_{Cu} \div w_{Cu}}{t_{In} \times \rho_{In} \div w_{In}} \approx 2.2147 \frac{t_{Cu}}{t_{In}} \tag{4.1}$$

Also, the thickness of In is controlled to a thickness less than 200 nm to prevent the hillocks formation. Based on the above equation, the CIS solar cell performance was investigated by varying the Cu/In atomic ratio from 0.93 to 1.

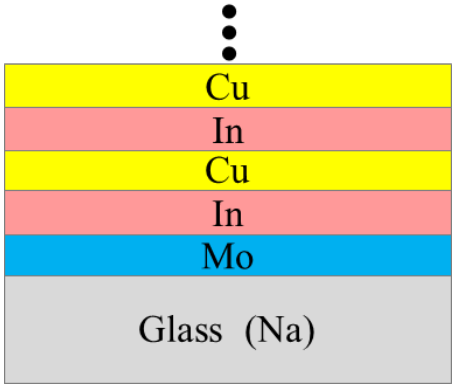

Figure 4.4 Schematic of the stacked sequence of the metallic precursor.

The I-V curve of CIS solar cells with different Cu/In ratios is plotted in Figure 4.5. And the performance of each cell is summarized in Figure 4.6. All the data were taken under illumination with simulated Air Mass 1.5 Global (AM1.5G) spectrum of 1000 W/m^2 at 300 K. It is clear that when the film is slightly Cu-poor, that is Cu/In atomic ratio is less than 1, the current density increases as the Cu/In ratio increases. This is because the p-type doping concentration in CIS film increases as the film contains more Cu, which leads to better a p-n junction between the CIS and the buffer layer.

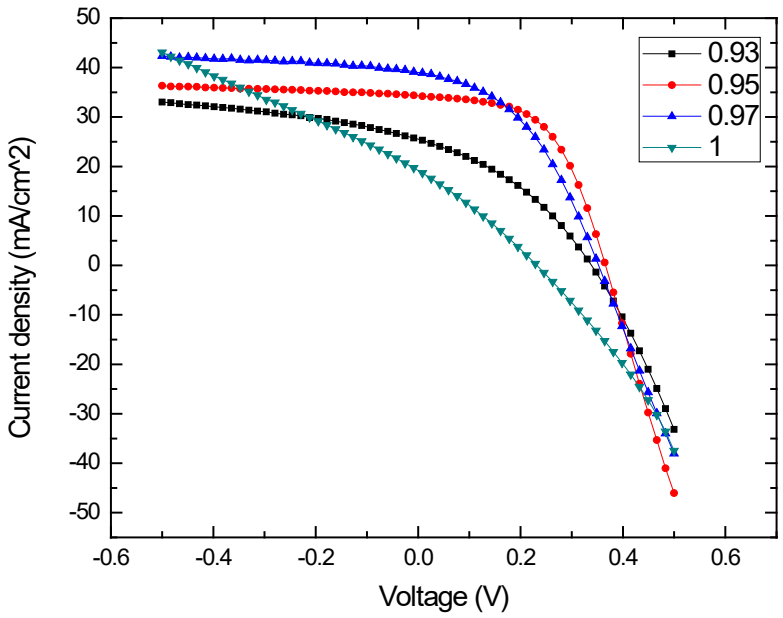

Figure 4.5 Current density versus voltage for CIS thin-film solar cells with different Cu/In atomic ratio.

The I–V characterization was modeled using a 1-diode equation:

$$J = -J_{sc} + J_s \times (e^{(\frac{q(V - J \times R_s)}{nkT})} - 1) + \frac{V - J \times R_s}{R_{sh}} \qquad (4.2)$$

where J_{sc} is the short-circuit current density, J_s is the reverse saturation current density, R_s is the series resistance in Ω/cm^2, and R_{sh} is the shunt resistance in Ω/cm^2. All device parameters are shown in Table 4.1. When the film is close to Cu-rich, in this case the Cu/In ratio is 1, the shunt resistance clearly decreases. Such degradation is due to the formation of the secondary Cu-Se binary compound (Cu_2Se), which works as a parallel shunt path in the CIS film. In addition, as mentioned in section 2.1, formation of OVC surface layer is the key to high-efficiency solar cells. The formation of the OVC layer occurs automatically on the top surfaces of slightly Cu-

deficient CIS thin films at high temperature when the Cu/In atomic ratio in the bulk of the film is kept at 0.85~0.95 [48].

From the above theory and the experimental results, the performance of the CIS solar cell is optimized at a 0.95 Cu/In atomic ratio.

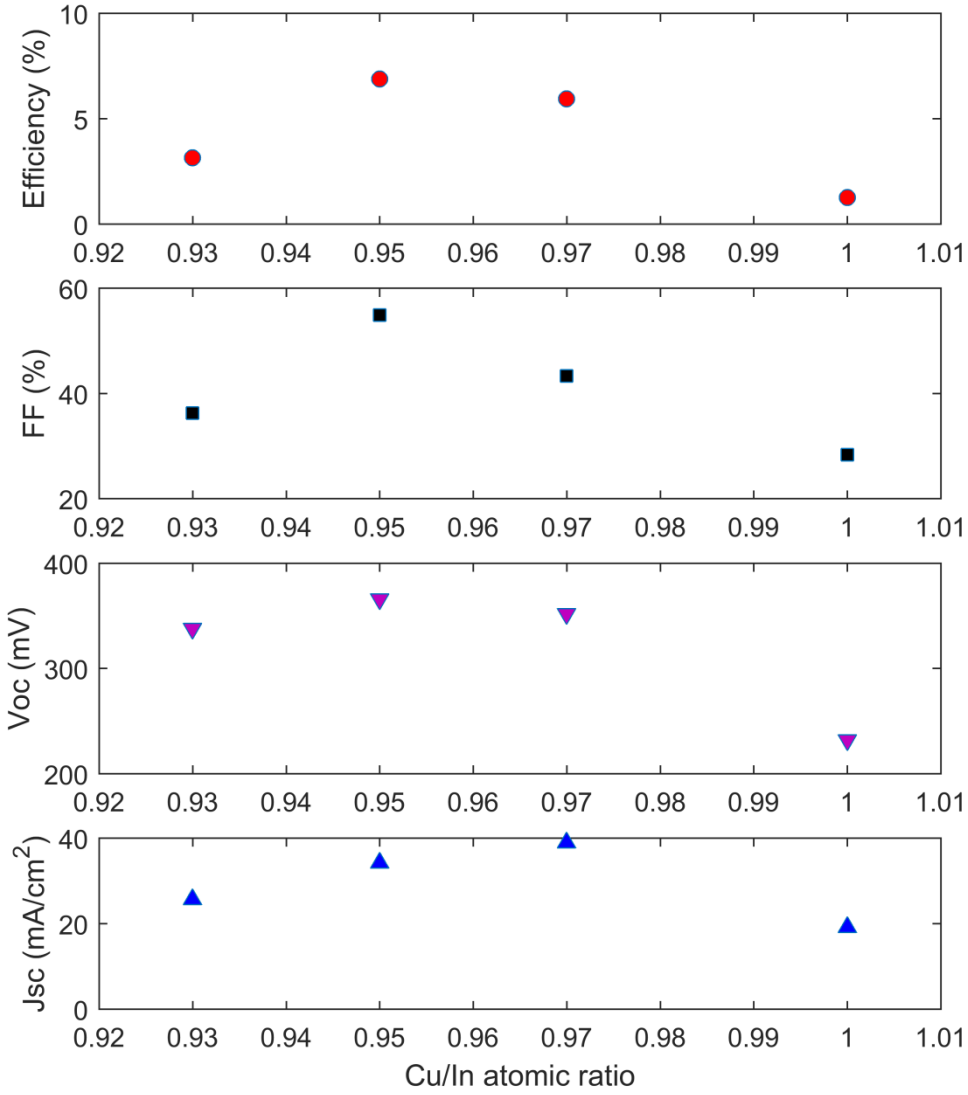

Figure 4.6 Performance of CIS thin-film solar cells as a function of Cu/In atomic ratio.

Table 4.1 Device parameters of CIS thin-film solar cells as a function of Cu/In atomic ratio.

Cu/In ratio	1-diode model			
	J_s (mA/cm^2)	n	R_s ($\Omega \cdot cm^2$)	R_{sh} ($\Omega \cdot cm^2$)
0.93	2.17e-3	5.329	1.447	101.356
0.95	7.00e-7	1.315	2.145	257.80
0.97	5.12e-5	2.069	2.723	179.99
1	6.27e-3	8.303	1.839	26.94

4.2 Film Properties Dependence on Annealing Time

The chalcopyrite CIS was formed at 500 °C at the third step of the annealing temperature profile, see Figure 3.4. In order to get better CIS thin film with larger grain size, several samples were annealed for different times at 500 °C. Figure 4.7 (a)–(f) shows the SEM images of CIS thin films prepared by the respective selenization process at 500 °C for the time range between 10 and 90 min. It is worthy to mention that the thickness of each layer in the metallic precursors was kept

constant (Cu/In ratio is 0.95), and that all samples were deposited under the same conditions.

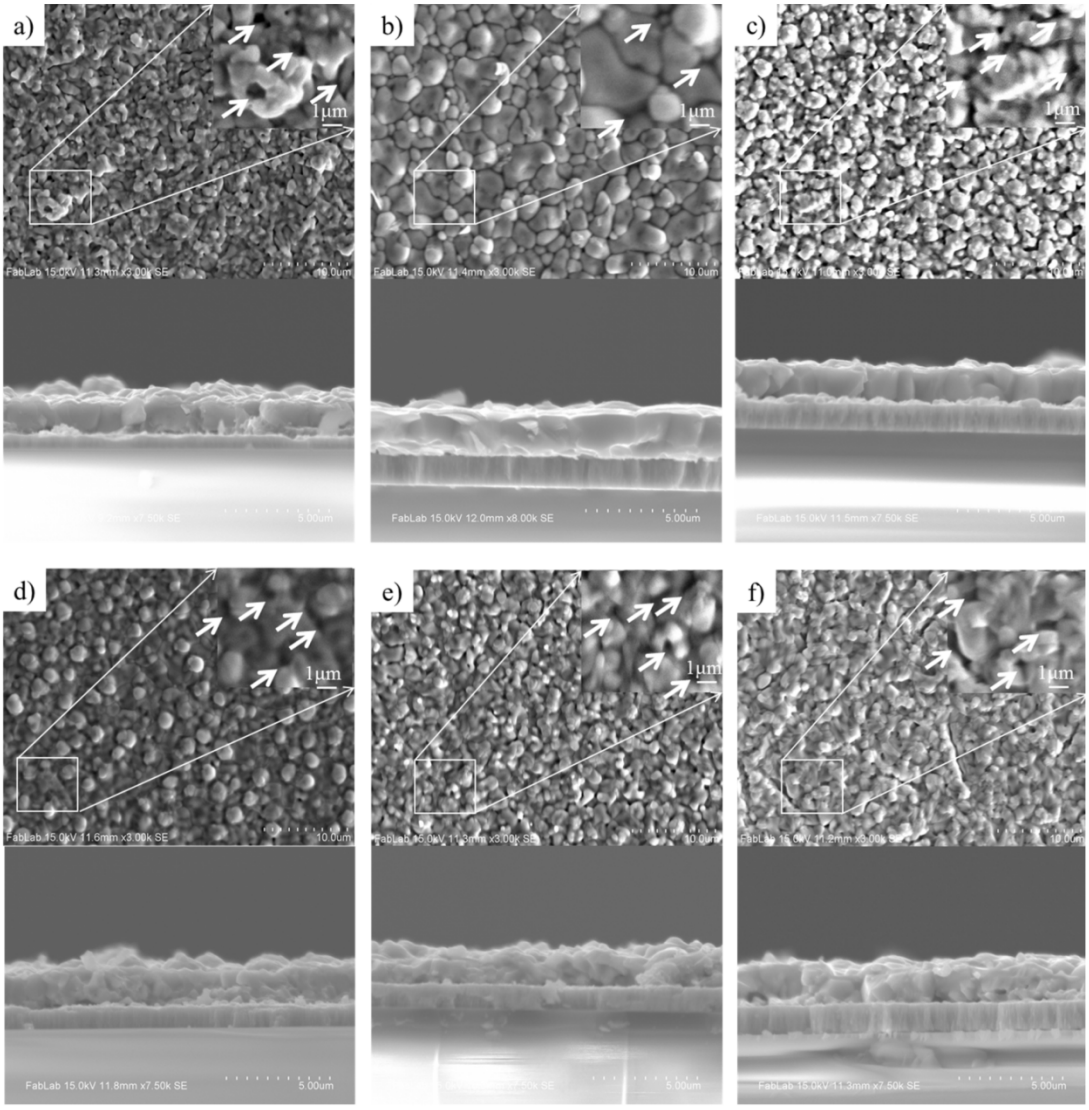

Figure 4.7 Top view and cross-sectional SEM images of CIS thin films after selenization at 500 °C for different time: (a) 10 min, (b) 30 min, (c) 40 min, (d) 50 min, (e) 60 min, (f) 90 min. The inset in the up-right corner is the zoom-in SEM picture, with arrows pointing to pore (pinhole).

Comparison of these micrographs reveals the dramatic influence of the reaction time on the formation kinetics of the CIS thin films. For a short-time annealing of 10 min, see Figure 4.7 (a), the film showed poor morphological characteristics with sub micrometer grains and a porous surface. The X-ray diffraction (XRD) spectrum of this film is shown in Figure 4.8 (a). The peaks for the In–Se and Cu–Se compounds indicate the amount of unreacted material remaining in the film. This had a significant impact on the performance of the cell, as parallel conducting path between the CIS and TCO layers is formed through these pores and material, which is to be discussed in more details later. When annealed for longer than 30 min, fully reacted films were produced. In Figure 4.8 (b), the XRD spectrum is shown for the CIS thin-film solar cell formed at 500 °C for 30 min. With narrow peaks of the single-phase chalcopyrite compound, the XRD spectrum confirms the existence of large crystal structure observed in the SEM images. Among these SEM images, clearly, the CIS film annealed for 30 min, see Figure 4.7 (b), had the largest average grain size (3–5 μm), relatively uniform grain boundaries, and a lower pore (pinhole) density (see the insets in Figure 4.7). As the annealing time increased, see Figure 4.7 (c)–(f), the grain size became smaller, both in the top view and cross-sectional images, and the film started to form a rougher surface with circular grains. In the cross-sectional images, more grain boundaries are observed at samples with longer annealing time, which indicates smaller grain size and lower quality films. Another useful motivation for this research is that because of the compact size of our graphite box (we could make it even smaller), it is possible to put it inside an XRD system to do real-time investigation on the formation of CIS while selenizing the precursors.

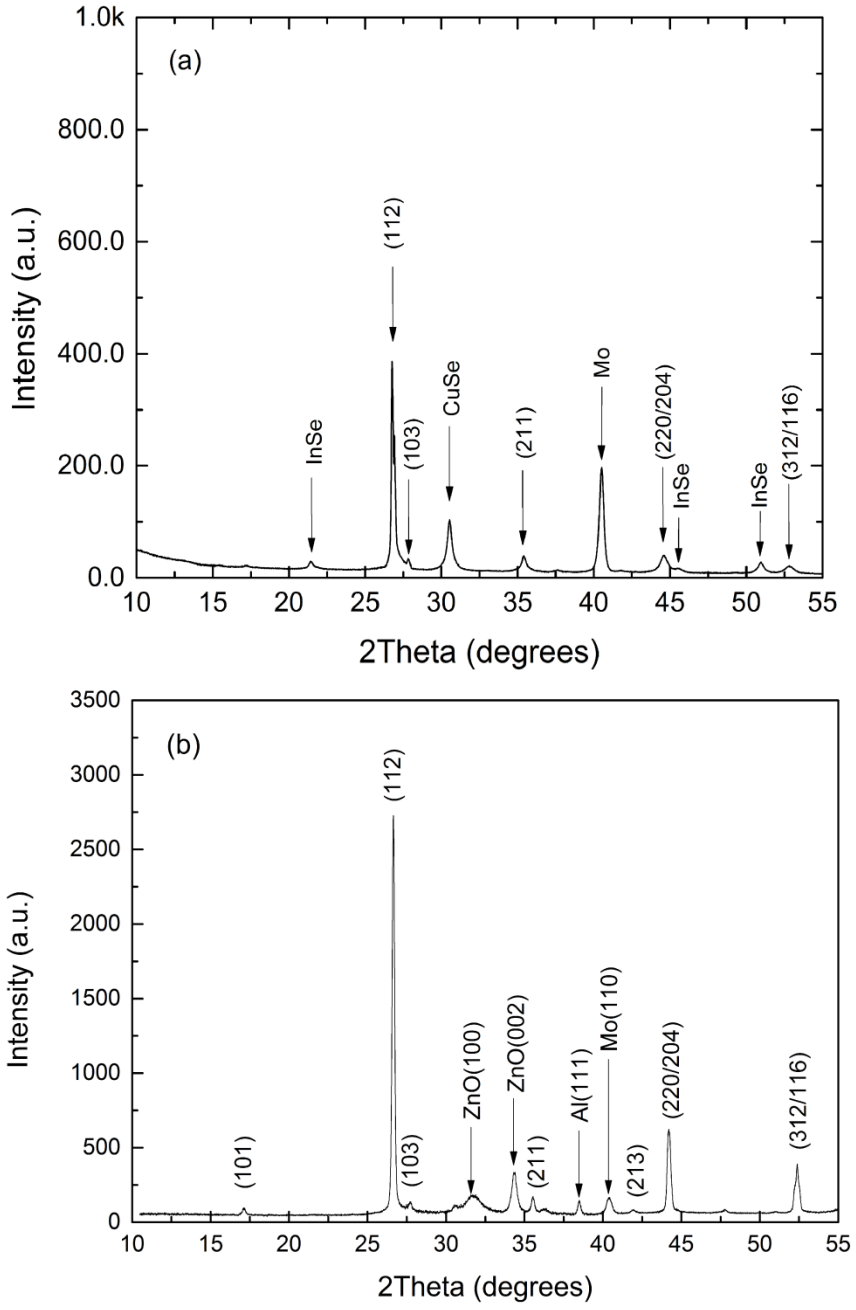

Figure 4.8 XRD spectrum of the CIS thin-film solar cells: (a) 500 °C for 10 min, (b) 500 °C for 30 min.

Table 4.2 presents the chemical compositions of CIS films measured by energy-dispersive X-ray spectroscopy (EDS). Here, the anti-stoichiometry ε and non-molecularity δ are considered to determine the electrical properties of CIS film,

$$\varepsilon = \frac{2[\mathrm{Se}]}{[Cu]+3[In]} - 1 \tag{4.1}$$

$$\delta = \frac{[Cu]}{[In]} - 1 \tag{4.2}$$

All samples had δ < 0 (In rich), since the precursors are deposited to get a Cu/In atomic ratio of 0.95. The films are likely of p-type conductivities, if ε > 0 (Se rich). From this point of view, the CIS films annealed for longer than 30 min were preferable to form p-n junction with n-type CdS layer. Ten-minute selenization is not sufficient for having plenty of Se to react with the precursor, which qualitatively agrees with the unreacted materials observed in the XRD spectrum, see Figure 4.8 (a).

Table 4.2 EDS results of CIS films after different annealing times

Annealing time (min)	Element concentration (at.%)			Atomic ratio	
	Cu	*In*	*Se*	$\delta = \frac{[Cu]}{[In]} - 1$	$\varepsilon = \frac{2[\mathrm{Se}]}{[Cu]+3[In]} - 1$
a) 10	24.24	25.88	49.88	-0.063	-0.021
b) 30	22.80	24.90	52.30	-0.084	0.073
c) 40	22.68	25.05	52.27	-0.095	0.069
d) 50	22.49	25.04	52.47	-0.102	0.075
e) 60	22.58	25.05	52.37	-0.099	0.072
f) 90	23.43	25.26	51.31	-0.072	0.034

Completed cells were prepared based on CIS films selenized for different times, to see the effect of the quality of CIS thin film on the performance of solar cells. Figure 4.9 plots the results. Comparing the efficiency and grain size in Figure 4.9, device with larger grain size has higher efficiency. The cell with the largest grain size (lowest pinhole density), which was annealed for 30 min, gave the best performance.

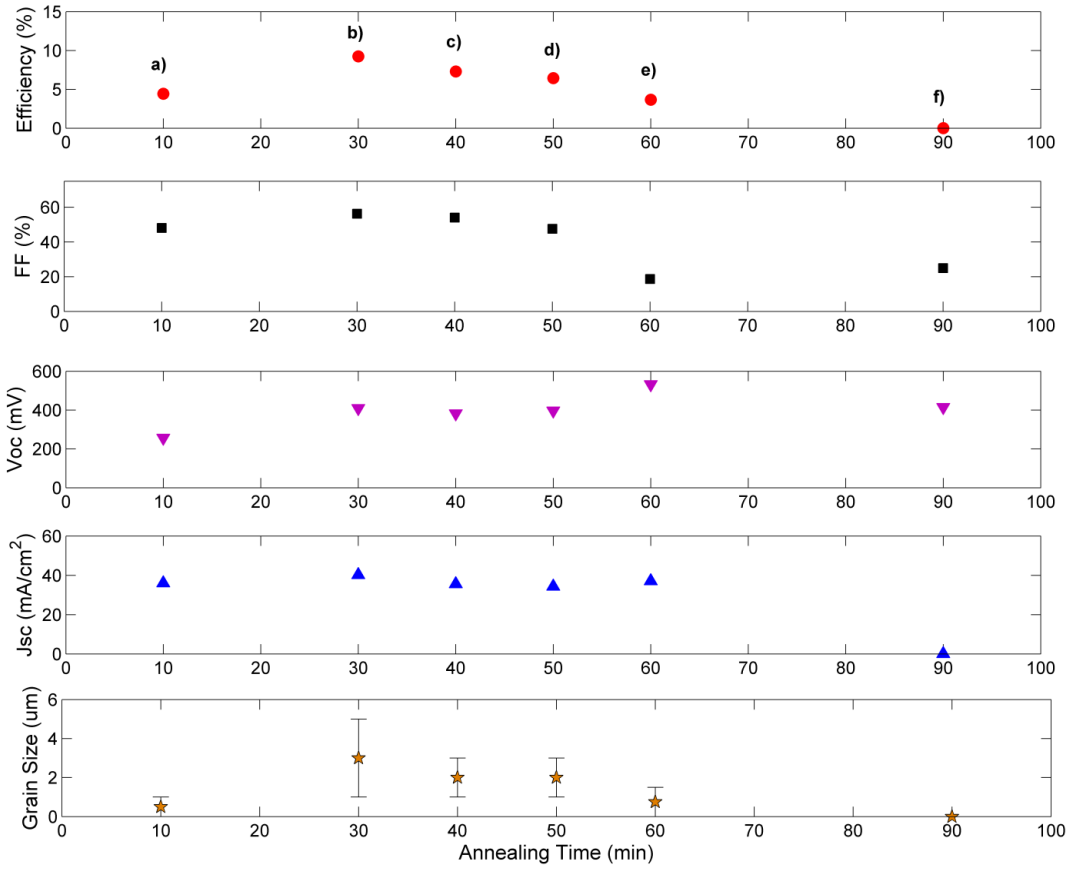

Figure 4.9 Performance of CIS thin-film solar cells as a function of annealing time at 500 °C.

4.3 CdS Thickness

In this section, the optimization of CdS thickness was carried by measuring the performance and EQE of CIS solar cell. Here, the metallic precursor was deposited with Cu/In atomic ratio of 0.95. And then, it was selenized inside the graphite box with the temperature profile illustrated in Figure 3.4. The annealing time at 500 °C was kept 30 min. After the selenization process, the CBD-CdS buffer with a deposition time from 12 to 15 min was deposited as soon as possible. Then i-ZnO/ZnO:Al layers with the thicknesses of 80 nm and 120 nm were subsequently deposited using the RF sputtering method.

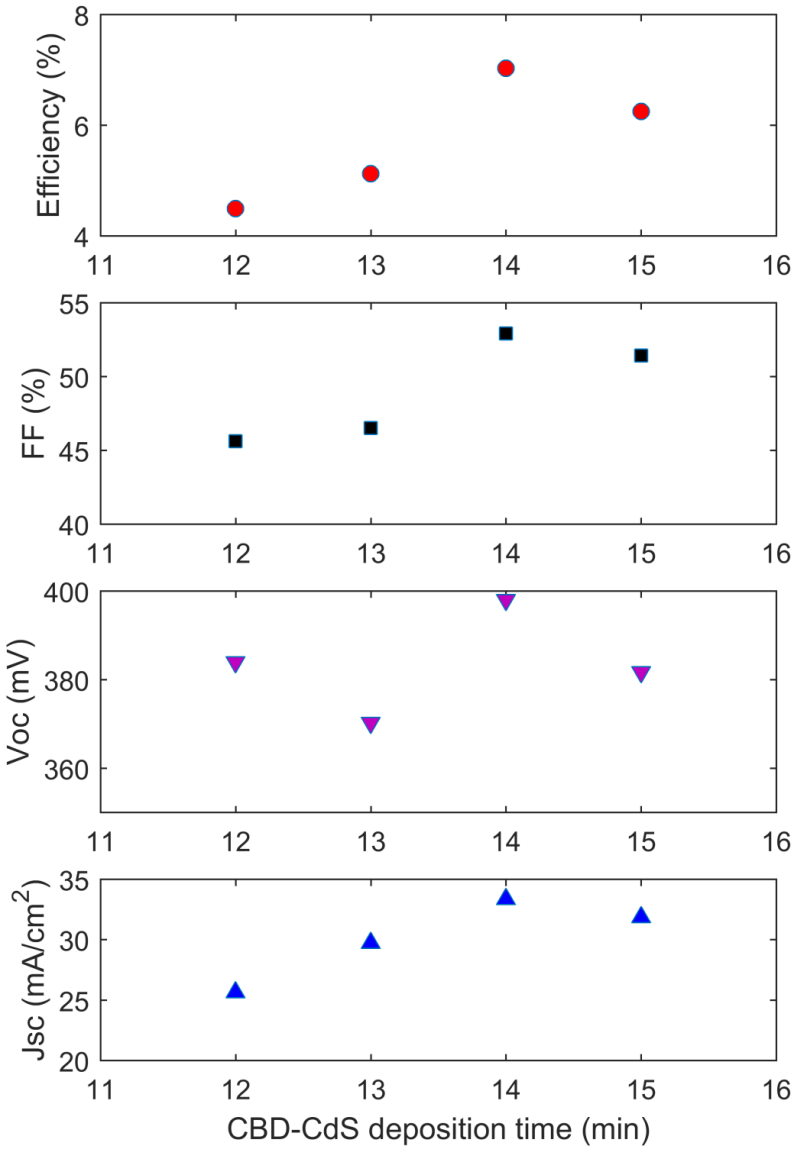

Figure 4.10 erformance of CIS thin-film solar cells as a function of CdS deposition time.

Figure 4.10 showed the performance of CIS solar cells with different CdS deposition time. Because the exact thickness could not be measured, I used the deposition time to represent the value of thickness. From the results, it was distinct that the best performance cell was the one with CdS after 14 min deposition. To establish a rough

relationship between the deposition time and the thickness of CdS, I monitored the thickness by the apparent color of the CdS on Mo. After 14 min CBD deposition, the surface looked blue, which means that about 60 nm CdS was deposited on the surface.

To better understand the effect of CdS thickness, EQE measurement was performed on CIS solar cells. Figure 4.11 plotted the results. The band gap of CdS is 2.4 eV, so the cut-off wavelength is about 515 nm. Photons with wavelength shorter than 515 nm will be absorbed in the CdS film. From Figure 4.11, it is obvious that thicker CdS absorbed more photons, which lowered the EQE of the solar cells at shorter wavelengths. However, because thin CdS buffer layer couldn't cover the surface uniformly, the interface property between CdS and CIS film was poor. This leads to higher defects density and increased recombination. So, the overall EQE is lower when the CdS thickness is not enough.

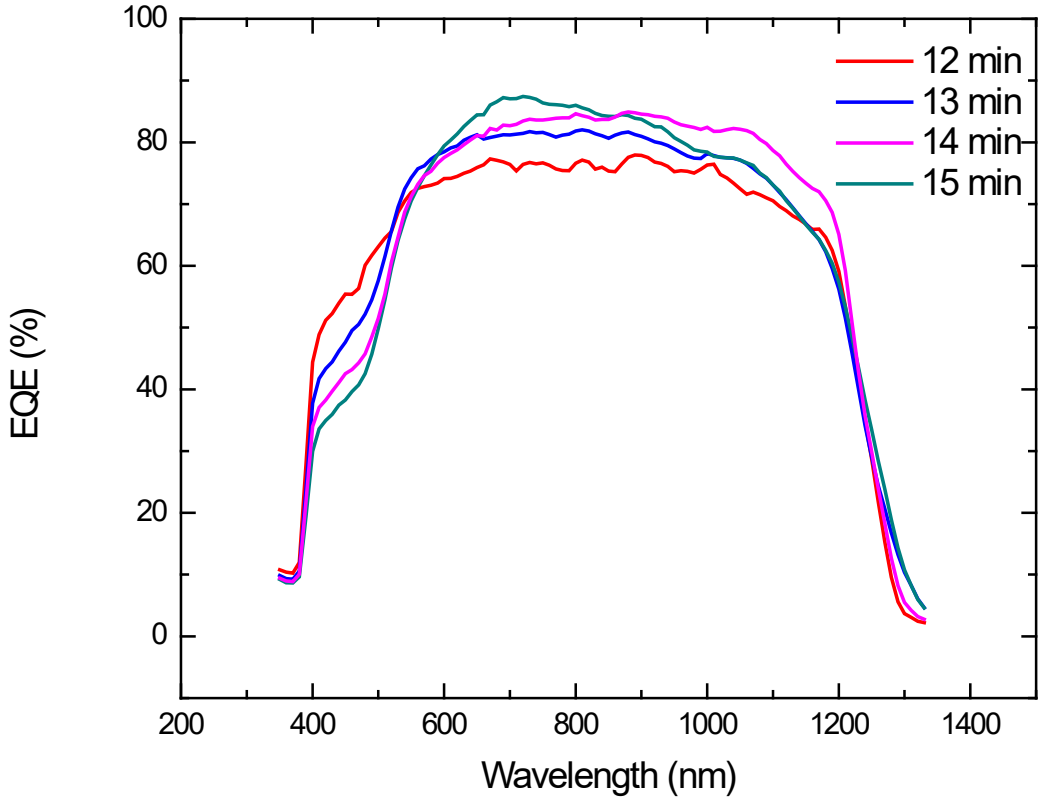

Figure 4.11 EQE of CIS thin-film solar cells with different CdS deposition time.

From above experimental results, the performance of the CIS solar cell is found to be optimized when the deposition time of CdS is 14 min.

4.4 Device Area

One CIS solar cell was fabricated to study the effect of device area on the performance. All the data discussed below was measured from one cell. Initially, a large cell of area 22.405 mm^2 was electrically isolated. Then, the area of this cell was re-defined by using a sharp razor blade. Each time after changing the area, the I-V characterization and the performance of the solar cell was measured, see Figure 4.12

and Figure 4.13. Also, the I-V characterization was modeled using a 1-diode equation. The parameters are listed in Table 4.3.

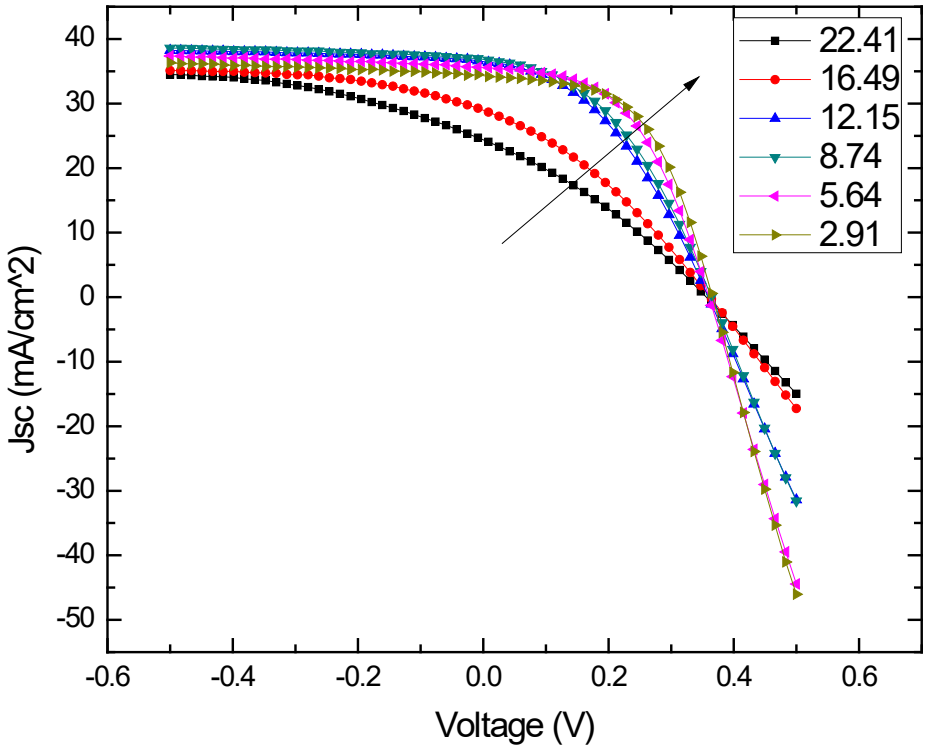

Figure 4.12 Current density versus voltage for CIS solar cell with different area (mm^2).

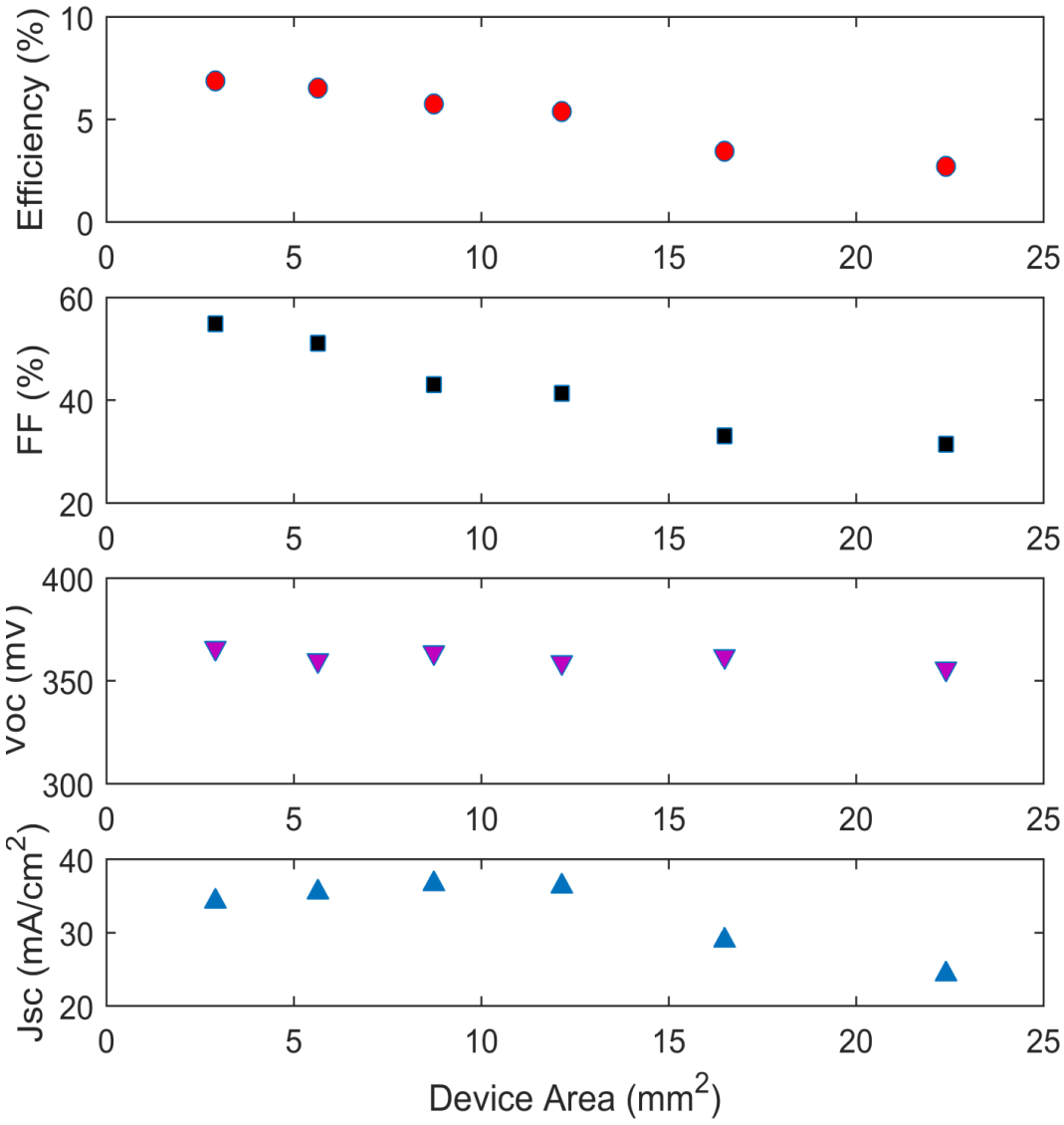

Figure 4.13 Performance of CIS thin-film solar cells with different area.

From the above figure, it was clear that as the device became smaller, the efficiency increased. The main reason causing the improvement is a better fill factor. It also can be seen in Figure 4.12, that the smaller the area, then the I-V curve got closer to a "square" shape. The short circuit current first increased then decreased, while the open circuit current remained almost the same. By fitting the I-V curve using a 1-

diode model, apparently, the reverse saturation current decreased as I made the cell smaller, which means the recombination became less. This can be easily explained by the decreased transport length of electrons before being collected by the top contact, since the top contact pattern remained the same when the device area is changed. Shorter transport length leads to a smaller recombination rate, due to a decreasing number of defects before being collected. In addition, the decreasing series resistance can also be explained by the shorter transport length.

Table 4.3 Device parameters of CIS solar with different area.

Area (mm^2)	Efficiency (%)	1-diode model			
		J_s (mA/cm^2)	n	R_s ($\Omega \cdot cm^2$)	R_{sh} ($\Omega \cdot cm^2$)
22.405	2.731	8.84e-3	9.786	3.244	3096.5
16.49	3.467	8.74e-4	3.912	5.181	191.55
12.15	5.397	4.58e-5	2.087	3.264	350.92
8.74	5.757	3.11e-5	2.003	3.078	302.32
5.64	6.546	1.60e-6	1.397	2.376	260.23
2.91	6.889	7.00e-7	1.315	2.145	257.80

However, the shunt resistance became smaller, which was worse, when the area was smaller. This is due to the shunt path generated in the periphery. Assuming that the number of the generated shunt sources per unit length is constant and the side length of the square area is d, then the density of the shunt source is proportional to 1/d. So,

the smaller area means a larger density of shunt path, which leads to smaller shunt resistance.

4.5 Potassium Fluoride Postdeposition Treatment Sample Characterizations

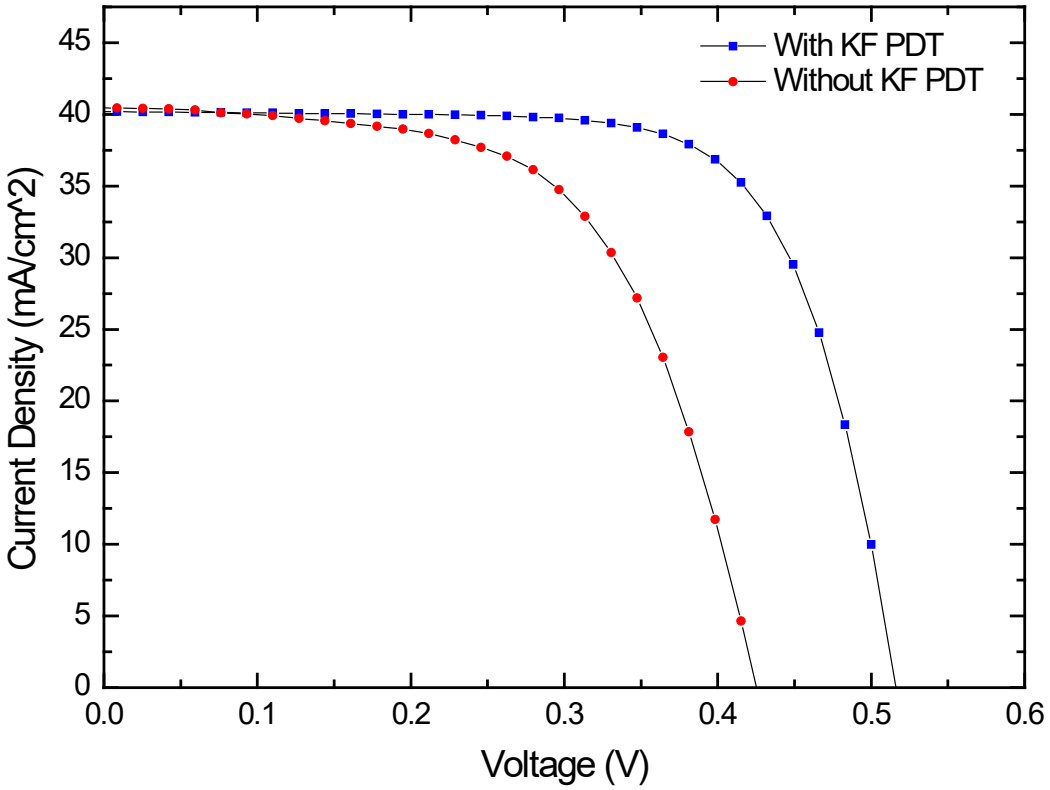

Figure 4.14 Current density vs voltage for CIS solar cell with and without KF PDT.

Figure 4.14 shows the I–V characteristics of the best CIS solar cells without and with KF PDT. All device parameters are shown in Table 4.4. Both cells have quite similar short-circuit current density (J_{sc}). However, the efficiency of the cell with KF PDT is

14.7% compared with the cell without KF PDT, which had a 10.3% efficiency. The increase of the open-circuit voltage (V_{oc}) and of the fill factor (FF) are the main reasons that lead to the 4.4% absolute increase in efficiency. V_{oc} increased from 0.423 to 0.516 V, and the FF increased from 60.0% to 70.7% after applying KF PDT to the standard processing. EQE is measured on both films to determine if the 90-mV gain in V_{oc} can be explained by the difference in the bandgap. The EQE results are shown in Figure 4.15. By integrating these results with NREL ASTM G173-03 Reference Spectra, we predict a short-circuit current density of 39.5 mA/cm^2 as compared with J_{sc} of 40.5 mA/cm^2 extracted from a Newport solar simulator using a calibrated Si solar cell, which demonstrate a good agreement. According to the measurement, both films can absorb photons and generate photocurrent for wavelengths up to about 1.2 μm, which means that they have a similar bandgap of about 1 eV. In fact, we believe that two factors result in the increase of V_{oc} and FF. Pianezzi et al. [49] pointed out that the CdS/CIGS interface was improved during KF PDT, and a reduced recombination at the interface was found using temperature-dependent J–V measurements. In addition, Shin et al. [50] indicated that the Cu-Se bond was weaker than In-Se bond; therefore, Cu can diffuse into the bulk during annealing in a Se environment. Then, the surface tunneling recombination is reduced due to the formation of a hole-blocking layer at the interface, which decreases the tunneling of holes across the n-ZnO layer into the p-CIS layer, resulting in the increase of V_{oc}.

Table 4.4 Device parameters for CIS solar cell with and without KF PDT.

Sample	Efficiency (%)	V_{oc} (V)	J_{sc} (mA/cm^2)	FF (%)	J_s (mA/cm^2)	R_s (Ω·cm^2)	R_{sh} (Ω·cm^2)	n
Without KF PDT	10.3	0.423	40.5	60.0	2.15e-6	1.01	255.5	1.68
With KF PDT	14.7	0.516	40.2	70.7	5.47e-8	0.52	1250	1.48

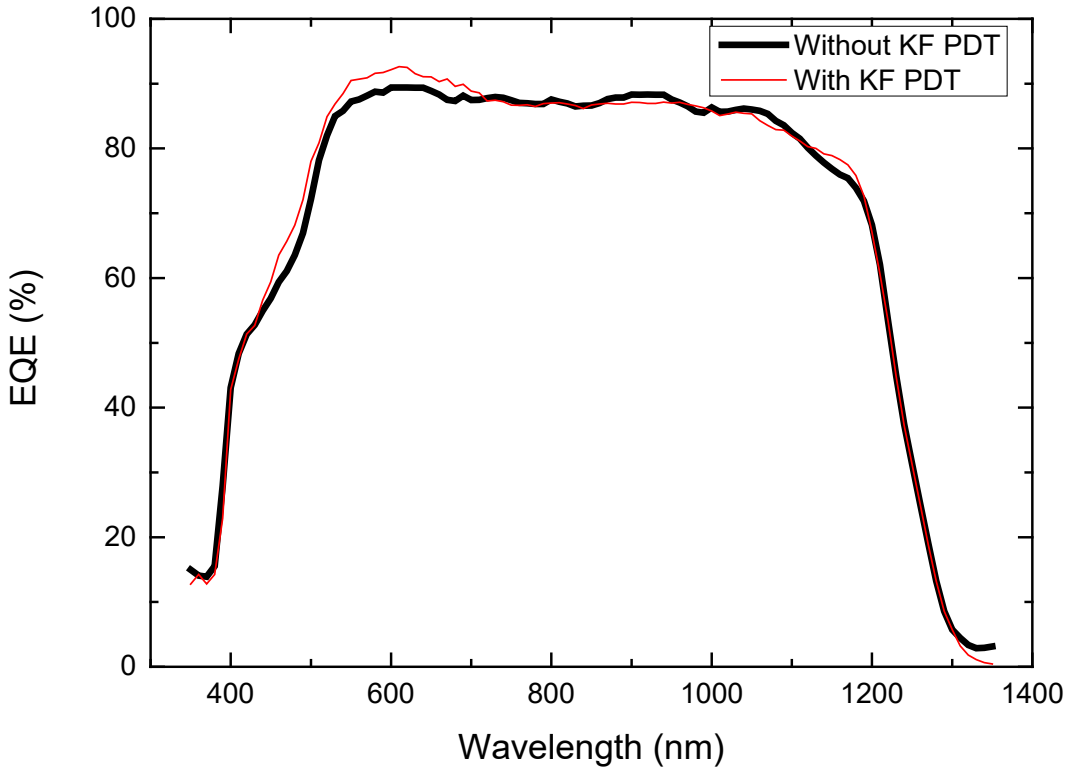

Figure 4.15 EQE of the CIS thin-film solar cell with and without KF PDT.

If the photocurrent is calculated based on the 1000-W/m^2 AM1.5G spectrum, assuming that each photon in this range will generate one electron–hole pair and assuming a completely transparent window layer, the maximum photocurrent is calculated to be about 48.6 mA/cm^2 [51], compared with the measured value for both

cells of 40.5 and 40.2 mA/cm^2. Loss of the photocurrent results from the loss of the EQE in different spectral regions. The absorption edge for the red response is due to the absorption in CdS and ZnO with bandgaps of 2.42 and 3.3 eV, respectively, and the blue response loss is the result of both ZnO free-carrier absorption and rear surface recombination. The sloping of the EQE curve as the wavelength increases can be explained by the fact that the distance at which the photons are absorbed is longer for low-energy photons: the light generated carriers must travel longer distances to be collected by the p-n junction, which have higher probability of recombination and, hence, a lower collection probability.

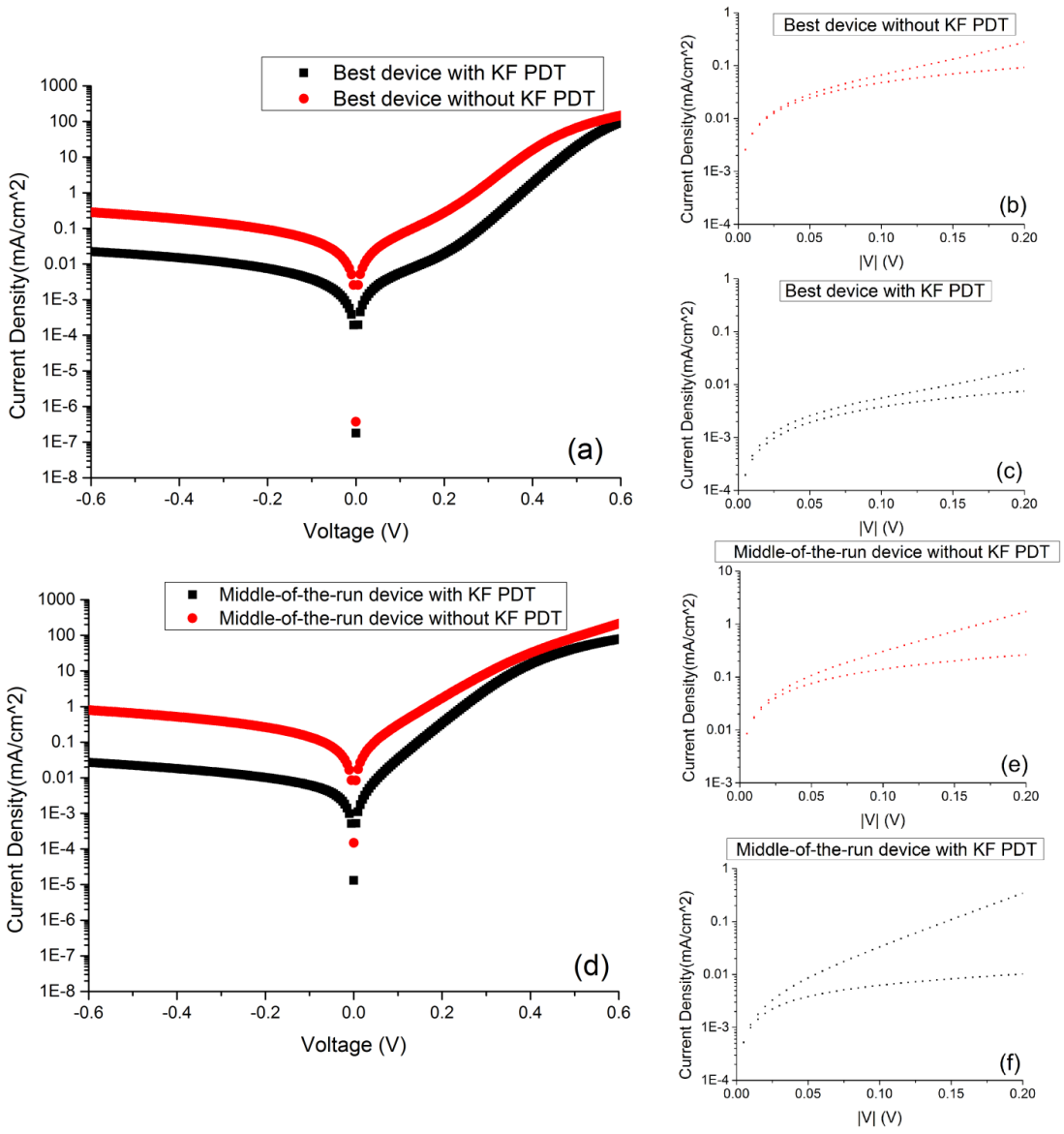

Figure 4.16 Dark IV characteristics of CIS thin film solar cells. (a) dark IV of best devices with and without KF PDT; (b), (c) dark current of best devices plotted in absolute value terms, i.e. |I| vs |V|; (d) dark IV of middle-of-the-run devices with and without KF PDT. Under one sun illumination, the device with KF PDT has 10.26% conversion efficiency, V_{oc} = 0.478 V and J_{sc} = 38.15 mA/cm2, the device without KD PDT has 6.64% conversion efficiency, V_{oc} = 0.396 V and J_{sc} = 35.31 mA/cm2; (e), (f) dark current of middle-of-the-run devices plotted in absolute value terms, i.e. |I| vs |V|.

Figure 4.16 shows the dark I–V curves of CIS thin-film solar cells without and with KF PDT. A close look into the reverse current of both cells reveals that shunt leakage exhibits a nonlinear dependence on the applied voltage, which cannot be explained by the traditional equivalent circuit model for solar cells (see Figure 4.17). A parallel shunt resistance R_{sh} represents the shunt current in this model, indicating an ohmic feature. Obviously, this model is not strictly suitable for CIS thin-film solar cells fabricated by our group. Furthermore, by fitting the reverse current in the voltage range of –6 to 0 V with a power law, we obtain a good fit for all cells with power exponent about 1.5–2.5. A space-charge-limited (SCL) current model was assumed to explain this nonlinear current feature in CIS thin-film solar cells [52,53]. From Figure 4.16 (b) and (e), two distinct regions in the dark I–V curve of the device without KF PDT can be identified. One is the high forward bias region (V >∼0.05V), showing an exponential forward current behavior ($I \propto e^{qV/nk_BT}$). Another is the low bias region (|V | <∼0.05V); symmetry of the current around V = 0 was clearly observed, whereas the curve with KF PDT [see Figure 4.16 (c) and (f)] shows almost no symmetry. The symmetry of the current can also be explained by the SCL current model. The reduction of the symmetry nature of current with KF PDT indicates that KF treatment helps reduce the shunt current from the SCL model.

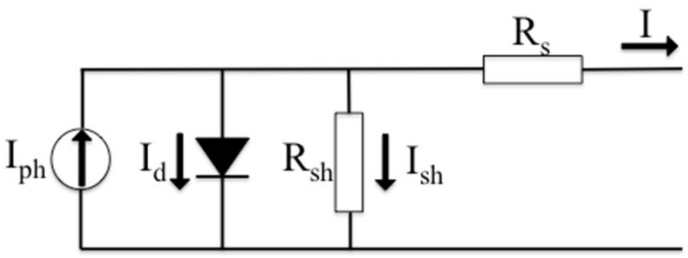

Figure 4.17 Traditional equivalent circuit model for solar cells.

Since only semiconductors with symmetric contacts are expected to have symmetric and power law voltage-dependent SCL current, the metal-semiconductor-metal (MSM) structure in CIS thin-film solar cells may exist in certain localized regions. Any pinholes in the thin window and buffer layers can cause the top metal to contact directly the CIS absorber layer, thus causing shunts. Additionally, considering the nonuniform distribution of Cu, In, and Se in the CIS film prepared by the method of selenization of SEL precursors, the electronic properties vary through the large area, which means that certain regions may behave as intrinsic material. Thus, an MSM structure may have been formed, and this leads to SCL current. Comparing the SEM images of CIS thin films before KF PDT and after KF PDT in Figure 4.18, fewer pinholes were observed on the surface after KF PDT. In addition, KF PDT improved the surface smoothness, which enhanced the following deposition quality of thin window and buffer layer and then reduced the possibility of forming local MSM structure. The I–V measurements on a cell with the KF PDT treatment clearly indicate a sizable reduction of the SCL current, presumably due to a reduction of the density of pinholes. A large increase of the energy conversion efficiency is observed in such cells.

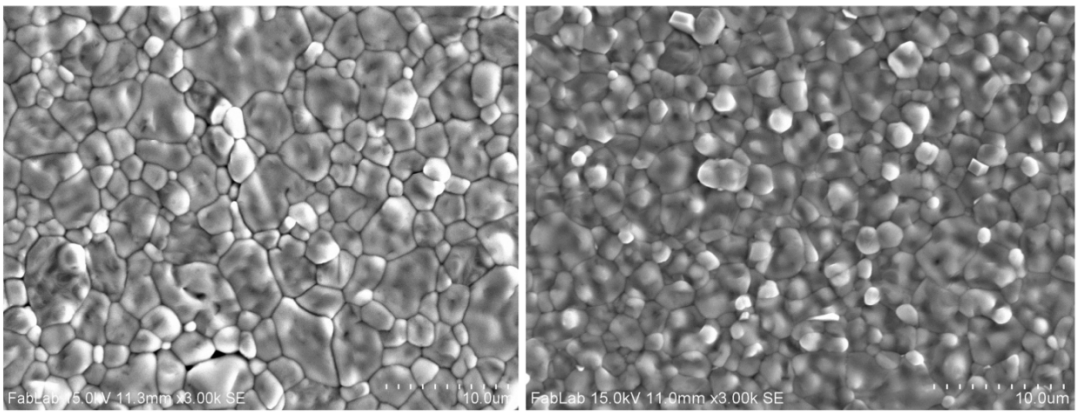

Figure 4.18 SEM images of CIS thin films. (a) Before KF PDT, (b) After KF PDT.

To further reduce this kind of shunt current, several potential ways will be tried in future experiments. Uniform CIS films are necessary to avoid SCL current. Therefore, during the selenization step, the Se pressure and temperature inside the graphite box should be controlled well to remain stable and even. This can be obtained by changing the partially closed graphite box to a totally closed graphite box with good sealing, and by reducing the slope of the heating to reduce the variance of temperature. A thin window and buffer layers with fewer pinholes are other key points. Depositing thicker CdS/ZnO layers is worth trying in future fabrication runs. In addition, the parameters of CBD and sputtering could be optimized to produce better quality CdS and ZnO layers separately.

Chapter 5 Conclusion and Perspectives

5.1 Summary of Accomplishments

We have demonstrated a very simple fabrication technique to produce high efficiency thin film solar cells. CIS chalcopyrite thin films have been obtained by a simple two-step process by selenization (annealing) of stacked elemental layers under selenium vapor in atmosphere. To optimize the quality of CIS thin films, morphological, chemical and structural properties were investigated and analyzed by SEM, EDS and XRD methods for different selenization time. Despite this simple fabrication approach, our short circuit current density is near record, at a value of 40.2 mA/cm^2, and was obtained without anti-reflection (AR) coating. An AR coating would typically raise the solar cell efficiency by about 1-2%. The highest efficiency CuInSe2 (CIS) solar cells have exhibited an efficiency of 15.4% at a short circuit current density of 41.2 mA/cm^2 [66]. We are able to reproducibly achieve above 12% conversion efficiency in our CIS cells, with the champion cell exhibiting near-record 14.7% efficiency. By the time of writing this proposal, this is the best published performance of CIS solar cells fabricated by the two-step selenization process using a graphite box.

Precise control of the Cu/In ratio in the precursor and Se amount provided during selenization of CIS ensures that single phase chalcopyrite CIS films and OVC surface were obtained. The performance of CIS solar cell is optimized at 0.95 Cu/In atomic ratio to avoid the formation of secondary Cu-Se binary compound (Cu_2Se), which works as a parallel shunt path in the CIS film.

Large grain size (> 2 μm), low pinhole density and good crystallinity are observed, which is the key to make high efficiency cells [67,68], when the selenization process is performed at 500 °C for 30 min leading to solar cells with ~10% efficiency.

The optimization of CdS thickness was carried by measuring the performance and EQE of CIS solar cell. Considering the tradeoff between the property of CIS/CdS interface and the absorption of the photons with shorter wavelength, the performance of CIS solar cell is optimized when the deposition time of CdS is 14 min, which approximately equals to a 60-nm thick CdS.

Moreover, as the device becomes smaller, the efficiency increases due to the better fill factor. The main reason is that the recombination is becoming less as I made the cell smaller. This is extrapolated from the fact that the reverse saturation current is decreasing. The number of defects that an electron could meet decreases before it is collected, which benefits from the shorter transport length of the electron. However, the shunt resistance became smaller, which is worse, when the area is smaller. Because the density of the shunt source is proportional to 1/d, smaller area means larger density of shunt path, which leads to smaller shunt resistance.

Using this approach, the impact of a KF PDT was explored. In this work, a CIS solar cell with a conversion efficiency of 14.7% was fabricated based on a high quality CIS film followed by KF PDT, a large improvement. Our work is consistent with the formation of a hole-blocking layer at the CdS/CIS interface after KF PDT, since the tunneling recombination (reverse saturation current) was greatly reduced. This reduction increased the open circuit voltage and energy conversion efficiency. The dark I-V characteristics of CIS solar cells before the KF PDT treatment show that the

shunt current leads to a symmetric I-V characteristics at low voltage and to a power law voltage dependence, which can be explained by the SCL current model and the likely formation of MSM shunts. Following a KF PDT, we observe an improvement of the surface smoothness and a reduction of the density of pinholes, which leads to decreased symmetric SCL shunt current. We discussed the possible physical origin of MSM shunts, and have proposed several methods to improve the performance of CIS solar cells in future work. We expect that this simple two-step process can be applied to CIGS solar cell fabrication.

Our results indicate that perhaps the CIS system is less sensitive to elaborate processing infrastructure and details than previously thought. This simple approach offers a very useful experimental platform from which to study a variety of thin film PV research topics.

5.2 Future Work

A promising approach for improving the performance of a low-bandgap solar cell without adding much cost is to deposit a high-bandgap solar cell on top to make a tandem solar cell. The first design principle to consider when making tandem solar cells is choosing the right bandgaps in order to optimize harvesting of the solar spectrum. It is well known that the bottom cell should have a bandgap around 1.1 eV and the top cell should have a bandgap around 1.7-1.8 eV [59]. Si and CIGS both have an ideal bandgap for the bottom cell. Recently, the efficiency of perovskite/silicon tandems in the four-terminal configuration has increased to

26.4% [60], and the two terminal tandems have improved to 23.6% [55]. Both mechanically stacked (four terminal) and monolithic (two terminal) Perovskite/CIS tandem solar cells can be implemented [62–64]. Our group has been devoted to make high performance thin film solar cells for over 5 years. We are able to fabricate both 14.7%-efficiency CIS solar cell with a two-step selenization method and 15.3%-efficiency Perovskite solar cell with a modified inter-diffusion method [65].

In the mechanically stacked approach, the two sub-cells operate independently with separate sets of terminals, which avoids electrical crosstalk and eliminate constraints associated with current matching and the need for a tunnel junction. A transparent and electrically insulating material serves as the interface layer in the tandem. Figure 4.19 shows the proposed structure with four terminals. The bottom sub cell uses exactly the same structure as the stand-alone CIS cell that we have developed in our laboratory. For the Perovskite top sub cell, we must use transparent electrodes for both side of it. Here, ITO is chosen. The two sub cells have slightly different size, where the top cell is relatively smaller. This is designed to have the Al/Ni contact recessed. Then, with excellent alignment technique and electrical expertise, high performance tandem solar cell can be achieved by optimizing the existing high-quality Perovskite and CIS solar cells via reducing optical losses in the structure.

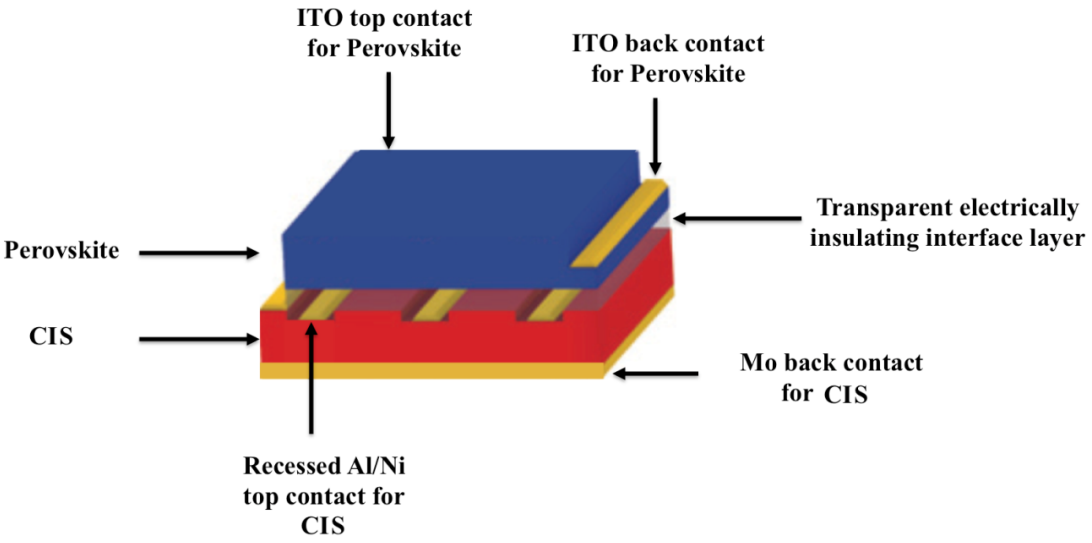

Figure 5.1 Four-terminal mechanically stacked Perovskite/CIS tandem

The second architecture is based on a monolithic two-terminal structure built in series, which contains a minimum number of layers to potentially lower optical losses and costs. It is expected that the efficiency of a monolithic tandem structure is higher than that of a mechanically stacked tandem cell because there are fewer transparent electrodes that parasitically absorb the light. Sophisticated optimization of a number of elements is required in this architecture, such as current matching, development of an appropriate recombination/tunneling layer. A Perovskite/CIS tandem solar cell is constructed based on the following structure: transparent conducting electrode (ITO)/PCBM/ $CH_3NH_3PbI_3$/PEDOT/ITO (or AZO)/CdS/CIGS/Mo/Soda lime glass. In this case, the tunnel junction consists of a PEDOT layer as the p recombination layer and an ITO or AZO layer as n recombination layer, as shown in Figure 4.20. There are several approaches to make the current matched between both sub cells.

First one is adjusting the thickness of $CH_3NH_3PbI_3$. Second, it is possible to modify the Perovskite band gap by tuning from $CH_3NH_3PbI_3$ to $CH_3NH_3PbBr_3$ to include a small proportion of Br in our perovskite structure. Finally, reducing the thickness of ITO, PEDOT and PCBM will decrease the losses and increase the short circuit current of CIS by letting more photon being absorbed in the bottom cell.

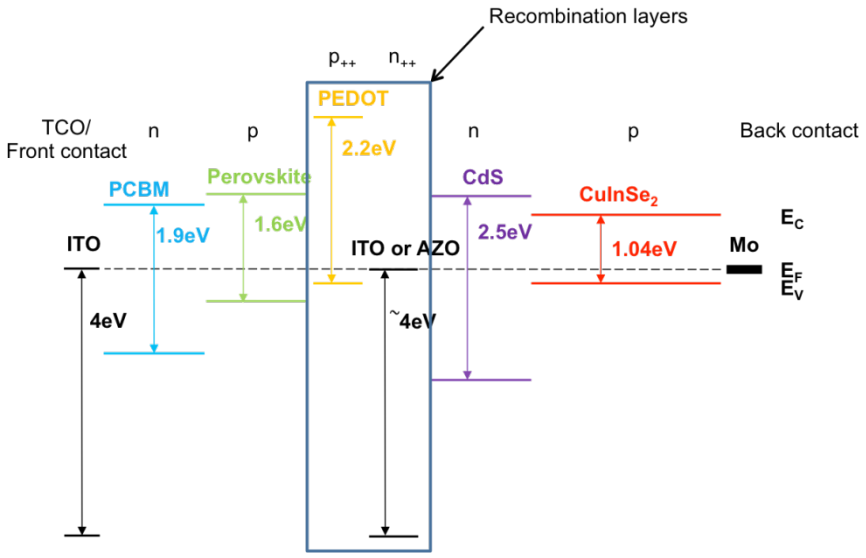

Figure 5.2 Band diagram for monolithically integrated Perovskite/CIGS tandem.

Part II Waveguide Bragg Gratings in Integrated Photonics

Since the first appearance of silicon transistors in the 1950s and the complementary metal-oxide-semiconductor (CMOS) in the 1960s, silicon has been the most important element in the microelectronic industry for over half a century. Meanwhile, photonic technology has revolutionized the communication industry since the invention of the laser in the early 1960s and the deployment of the first transatlantic fiber optic cable in the late 1980s. The human society has benefited from both technologies to enjoy products like mobile devices that fit into one's pocket, internet that is capable to transmit data at the speed of light, and etc.

The development of photonic devices relying on silicon based material as the optical medium, which combines the two great inventions of the last century, is paving the way for a monolithically integrated optoelectronic platform in a single chip [69–71]. Silicon photonics benefits from the silicon technology and the photonic technology,

and is expected to transmit and process big data with light on a small silicon chip. The first decade of this century has seen tremendous progresses in the field of silicon photonics with the successful development of high-performance components that are the key to realizing the great mission of silicon photonics: the on-chip optical data communication [72].

Among all silicon photonics platforms, the silicon nitride (Si_3N_4) planar waveguide platform provides benefits like low optical losses, transparency over a wide wavelength range (400-2350 nm), compatibility with CMOS and wafer-scale foundry processes, and high-power handling capabilities. When combined with SOI and III-V devices, the three platforms together open up a whole new generation of applications and system-on-chip applications [73]. The ability of ultra low-loss waveguide (<1 dB/m) that can handle high optical power can be engineered for linear and nonlinear optical functions, including ultrahigh Q resonators, optical filters, narrow linewidth and tunable lasers, optical signal processing circuits and quantum communications. However, there are still problems that need to be addressed before integrating thousands of individual components into a small silicon chip to form a functional silicon photonic system with unparalleled performances.

In this part of the thesis, waveguides Bragg gratings on silicon nitride planar waveguide platform are investigated to improve the performance of several silicon photonics components. Improvement of electron-beam lithography (EBL) and inductively coupled plasma (ICP) etching in fabrication process to achieve more accurate silicon photonic devices is presented in Chapter 6. Chapter 7 will discuss the basics of waveguide Bragg gratings and ABCD matrix method. We introduce an

efficient z-shape waveguide design to achieve 83-dB filtering of the pump field by suppressing another supported TM mode in the waveguide and avoiding scattered modes at output port in Chapter 8. A numerical model based on ABCD matrix method of Bragg grating is developed to optimize the structural design of Fabry-Perot cavity enhanced four-wave mixing (FWM) device. An FWM conversion efficiency of around -50 dB is observed inside a 1.8-mm long cavity, which is enhanced over 61 dB compared to a single straight waveguide with the same length, as is shown in Chapter 9. In Chapter 10, a 10-μm long complex waveguide Bragg grating (CWBG) with a slow down factor of 6 and an average transmission of 70% within bandwidth between 626 nm and 630 nm is demonstrated. Using this CWBG, to achieve π phase shit, it requires a temperature increase of about $\Delta T = 175℃$.

Chapter 6 Nano-Fabrication Process

The demanding accuracy requirement of silicon photonic devices is always challenging. The most straightforward and efficient way to achieve highly accurate silicon photonics devices is to improve the precision of the fabrication process. Every single step during the whole process is critical to reduce the dimensional errors of the resulting devices. As an example, in this chapter, we will demonstrate that, by minimizing the field stitching error in the electron-beam lithography (EBL) system and by introducing three-stage inductively coupled plasma (ICP) etching process to optimize the side wall smoothness, the fabrication accuracy of silicon photonic devices can be improved and high performance is thus achievable.

6.1 Field Stitching Error

In EBL system, the beam is formed and steered on the wafer to draw shapes contained in a single e-beam writing field. Any pattern larger than a single writing field will be written in segments, which are then stitched together by stage movement to generate the large area pattern. The system first moves the wafer stage so the e-beam column is centered on the first writing field, then writes the portion of the shape within that e-beam writing field. The system then moves the wafer stage one writing field spacing next to it, and begins writing the remainder of that shape. These stage movements have several implications on the design, due to imperfections called “Field Stitch Errors”. The beam will jump between neighboring writing fields, as shown in Figure 6.1, and this can cause the two writing fields to be stitched with an

offset. Precise stage movement is essential to minimize the stitching error, and this can be achieved by using laser interferometer-controlled stage.

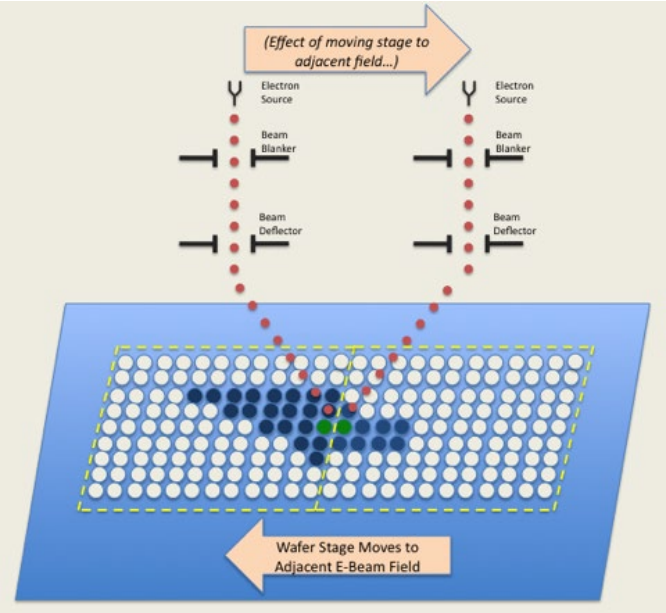

Figure 6.1 Demonstration of how two adjacent e-beam writing fields is “stitched” together.

In addition, electron beam deflection must be adjusted to match the stage movement, which is referred to as “writing field alignment.” The better the writing field alignment is, the smaller the placement error will be in positioning the beam at any pixel. The magnitude of this error increases when the beam is steered to pixels further from the e-beam column. This indicates that the error between adjacent pixels which are on opposite sides of a writing field boundary, such as the two green pixels in Figure 6.1, is a worst case. To expose large area nanostructures, a large writing field must be used; otherwise, the stage movement time would be impractically long. However, writing field alignment accuracy decreases with a larger writing field owing to its low magnification. So, for different types of structure, it is important to

choose the right size of the writing field, and sometimes even the combination of different writing field sizes. Figure 6.2 demonstrates a clear stitching error between two neighboring writing fields.

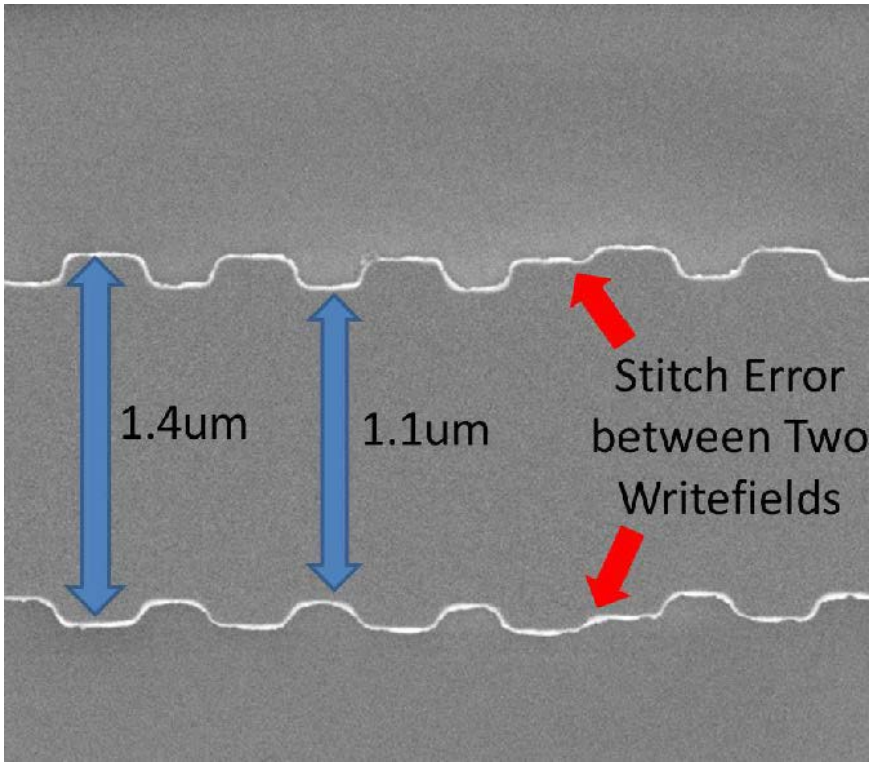

Figure 6.2 SEM figure of one Bragg grating structure
with clear field stitching error.

In our applications, the length of the waveguide Bragg gratings ranges from a few hundreds of microns to a few centimeters. In most cases, 250 μm × 250 μm writing fields is chosen to avoid severe field stitching error and keep the writing time within one hour. Proper settings and writing field alignment, together with coating a conductive aquaSAVE layer on top of the photoresist to reduce charging effect on top of the dielectric substrate, are also essential steps requiring careful attention. Two SEM figures of waveguide Bragg gratings are shown below in Figure 6.3, which both

contain two adjacent writing fields. As we can see, no obvious field stitching error exist, which is also true within the whole 2-cm long devices. An EBL patterning like this will be proper for subsequent experimental characterizations.

(a)

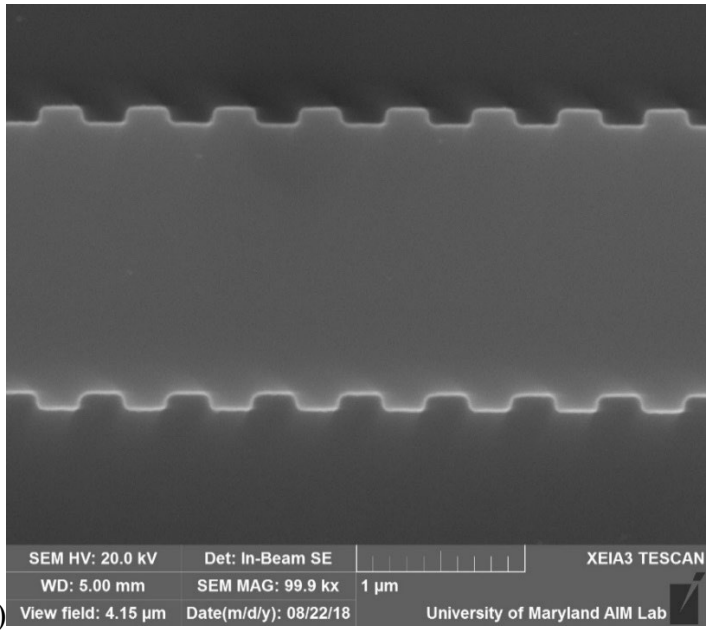

(b)

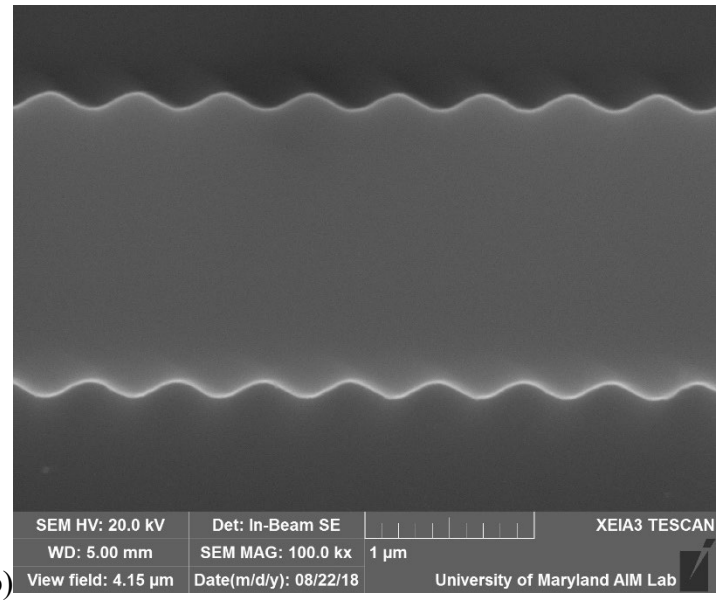

Figure 6.3 SEM figures of two waveguide Bragg gratings. (a) A square shape Bragg grating with narrow and wide width of 1.6 µm and 1.8 µm separately. (b) A sinusoidal shape Bragg grating with narrow and wide width of 1.6 µm and 1.8 µm separately.

6.2 Inductively Coupled Plasma Etching

Inductively coupled plasma (ICP) reactive ion etch is an anisotropic dry etching process used to remove material with the use of chemically reactive plasma under low pressure. ICP etching is a widely used technique to deliver high etch rates, high selectivity, low damage processing and provides excellent profile control. A cross-section of an ICP system (Oxford Instruments Plasmalab System 100, which used in this study) is illustrated in Figure 6.4. The ICP system contains two separate RF generators, providing individual control over ion energy and ion density. One RF source operates typically at 13.56 MHz and its power is coupled into the plasma chamber from outside to strike a plasma. And another auxiliary RF power is connected to the sample stage to generate a DC bias to accelerate the plasma ions from the plasma towards the sample surface. The RF source in the upper part of the chamber generates the plasma and the auxiliary RF power controls the bias voltage, that is, the ion energy.

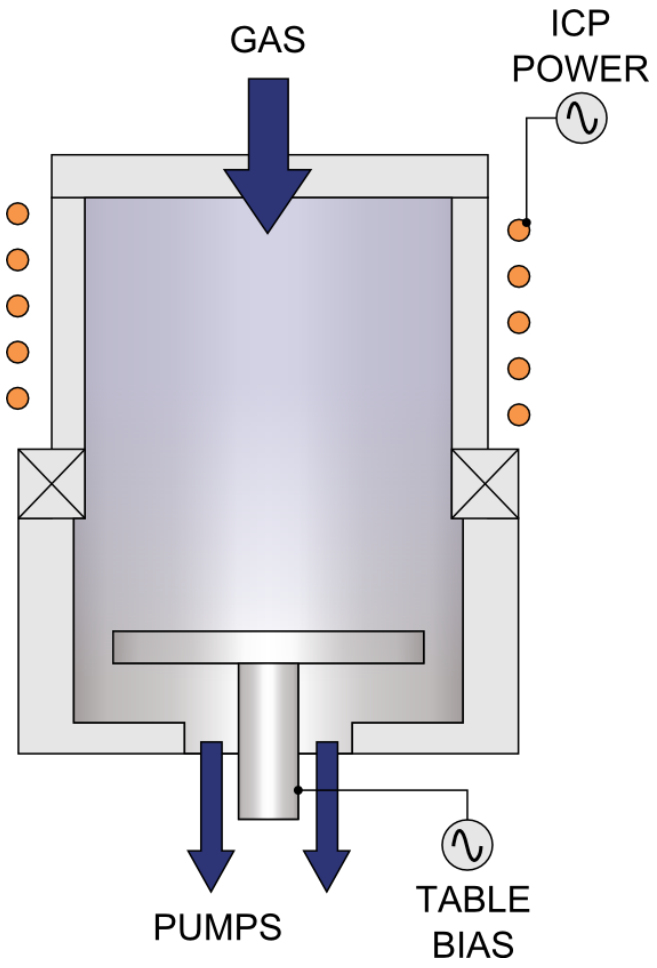

Figure 6.4 Schematic of an ICP machine illustrating the mechanical setup and the positioning of the electrodes and gas inlet and outlet. The top ICP electrode generates a plasma, while the substrate electrode creates a table bias to accelerate the ions[74].

Figure 6.5 shows a bowing plasma etching profile of a 300-nm etch depth silicon nitride layer on thermal silicon dioxide substrate. The parameters used in the etch recipe for silicon nitride are listed in Table 6.1. As we can see in the figures, the side wall of the silicon nitride layer is not vertical. There is a “ring” shape groove 100 nm away from the top surface along the whole layer. The decrease of the width difference between the narrow and the wide segments reduces the strength of the grating. Together with the changing of grating period, it strongly affects the accuracy of the

device. More importantly, the width of the waveguide is narrower than the desired dimension, which could significantly reduce the coupling efficiency of the inverse taper design that is optimized for the specific platform.

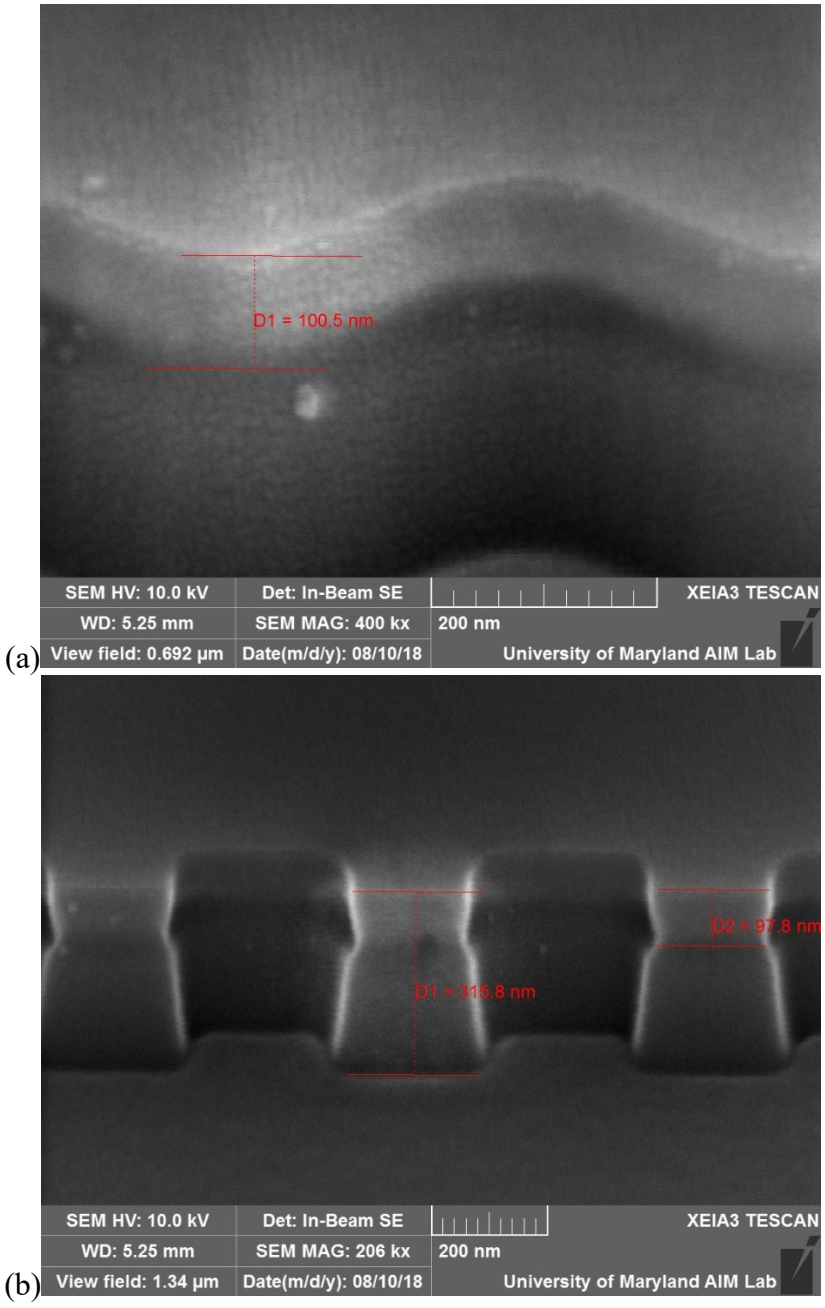

Figure 6.5 SEM figures of bowing plasma etching profile. (a) Tilted view of a sinusoidal shape Bragg grating. (b) Tilted view of a square shape Bragg grating.

Table 6.1 Parameter list for original ICP silicon nitride etch

ICP Etch Parameter	Value
SF_6 gas flow	10 sccm
CHF_3 gas flow	90 sccm
Pressure	15 mTorr
Chiller Temperature	5 ˚C
ICP power	500W
Auxiliary RF power	25W

The reason why the bowing etching profile is formed can be explained with a combination of two mechanism. First, during etching of silicon nitride in a pure fluorocarbon-based gas plasma, an etch-inhibiting fluorocarbon layer gradually forms on the silicon nitride surfaces. If thick enough, this layer can eventually inhibit etching in both the vertical and lateral directions [75]. During etching, the vertical and lateral etching rates evolve in time as the thickness of the fluorocarbon layer increases. Second, variation of the etch rate depending on the surface area of the material to be etched is known as a loading effect. This effect observed when the active species in the plasma are depleted rapidly by the reaction with etched material. It is affected by the lifetime of the active species as well as the chamber volume and feed gas flow rate [76]. The effect is stronger when the etching process is dominated

by the chemical etching with neutral atoms and weaker when the etching is driven by the ions [77]. The heavy fluorine ions are the main component for silicon nitride etching. But if the auxiliary RF power is not high enough, that is the ion energy is low, the etching rate can be lower when reaching the bottom of the side wall due to the lower density of fluorine ions. So, the fluorocarbon film formed during the etching reduces the etching rate at the upper part of the side wall, while the loading effect reduces the etching rate at the lower part of the side wall. Based on these two effects acting together, the bowing etching profile is formed.

To etch anisotropic vertical nanostructures, both fluorocarbon films and loading effect needs to be avoided. When sidewall passivation layers are formed during etching, they can be controlled by a careful balance of the etching chemistry [78–80]. Oxygen can be added to reduce fluorocarbon depositions when etching silicon nitride in fluorocarbon-based gas chemistries. It can be bound to carbon and reduces the fluorocarbon film formation, or an oxygen plasma step can be added to remove the fluorocarbon layer and restores the bare nitride surface. Simply increasing the auxiliary RF power, which increases the energy of fluorine ions, can reduce the loading effect.

Finally, by considering that the formation of the bowing etching profile is an effect due to a relatively deep etching, a three-stage etching strategy combined with added oxygen gas flow and higher auxiliary RF power can be developed to minimize the dimensional error of the fabricated devices as shown in Figure 6.6. The improved parameters used in the etch recipe are listed in Table 6.2.

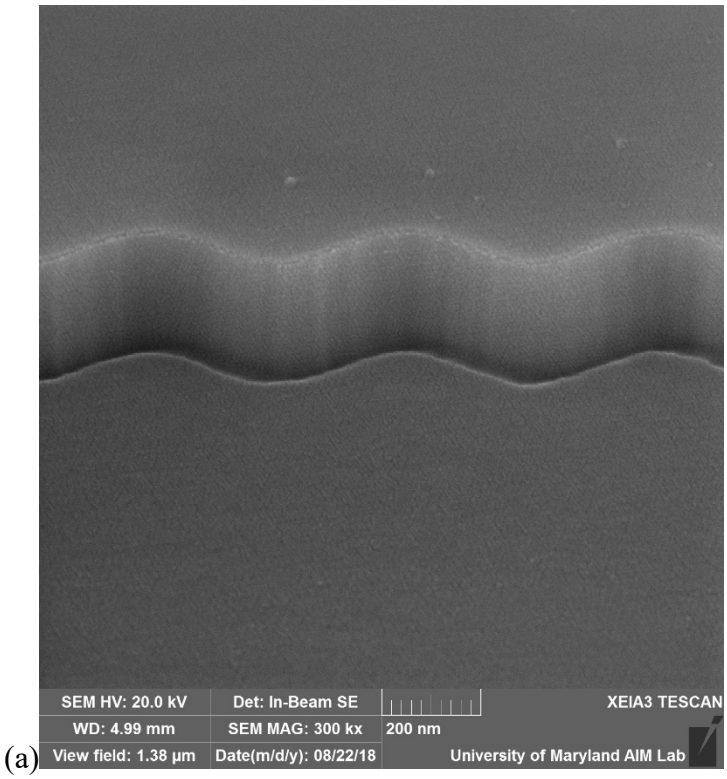

(a)

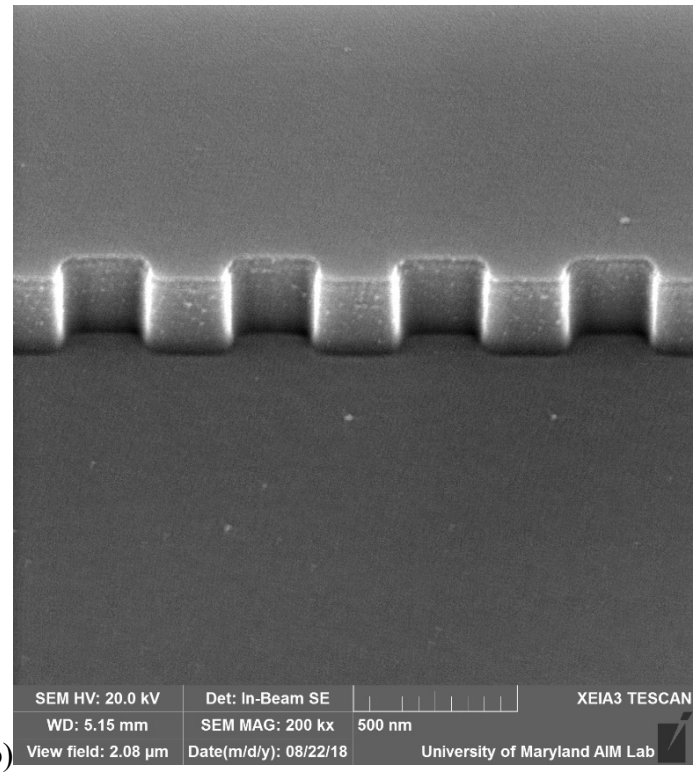

(b)

Figure 6.6 SEM figures of vertical etching profile. (a) Tilted view of a sinusoidal shape Bragg grating. (b) Tilted view of a square shape Bragg grating.

Table 6.2 Parameter list for improved ICP silicon nitride etch

ICP Etch Parameter	Value
O_2 gas flow	5 sccm
SF_6 gas flow	30 sccm
CHF_3 gas flow	60 sccm
Pressure	15 mTorr
Chiller Temperature	5 ˚C
ICP power	500W
Auxiliary RF power	100W

In this chapter, we have shown two examples where more accurate silicon photonics devices can be achieved by improved nanofabrication techniques with more precision. The improvement of fabrication tools and techniques is absolutely the most important way to improve the device performance. In particular, we show that structures over centimeters long could be patterned by EBL without obvious field stitching error, by doing proper setting and alignment. Also a simple three-stage etching strategy combined with optimized ICP recipe was proposed to avoid the bowing etching profile. By use of this approach, Bragg grating nanostructures with vertical profile constructed on 300-nm silicon nitride layer are fabricated.

Chapter 7 Waveguide Bragg Gratings

The propagation of electromagnetic radiation in periodic media exhibits many interesting and useful phenomena. In this chapter, we will discuss some general properties of wave propagation in waveguide Bragg gratings. This chapter will start from some basic concepts of Bragg gratings, followed by employing the ABCD matrix method to study the transmission and reflection of optical waves in such a structure. Provided that complex filter shapes can be achieved in the grating-based structures, we then introduce a novel silicon photonics grating structure, namely the complex waveguide Bragg gratings (CWBG), in which basically any spectral shape filter can be realized.

7.1 Basics of Bragg Gratings

The waveguide Bragg grating that we will focus on in this work is an optical waveguide device with a periodic variation of the refractive index along the propagation direction, as shown in Figure 7.1, where the waveguide with corrugated grating on sides of a period Λ in space are patterned by EBL. Constructive interference between different reflections occurs when the optical path difference is an integral number of wavelength λ_0/n_{eff} in the waveguide, that is the period of the grating satisfy the following Bragg condition,

$$\Lambda = \frac{m\lambda_0}{2n_{eff}}, \text{ m} = 1, 2, 3,\ldots \tag{7.1}$$

where λ_0 is the vacuum wavelength of light, and n_{eff} is the overall effective index of the waveguide where light propagates which includes both the average effective index and the effective index variation. This waveguide Bragg grating can also be considered as a diffraction grating which diffracts the forward-travelling wave into backward-traveling wave. A large reflectance may be reached in some wavelength range centered at a certain wavelength which fulfills the Bragg condition.

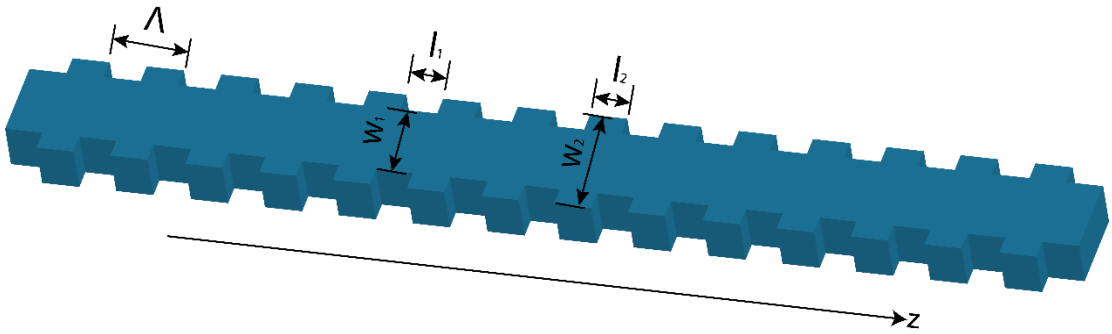

Figure 7.1 Schematic illustration of a typical periodic waveguide Bragg grating.

The waveguide Bragg grating showed in Figure 7.1 can be considered as the simplest periodic medium, which is made of alternating layers with different refractive indices. With the variation of width in layers, the effective refractive index varies as well, and the relationship between which is calculated by FIMMWAVE, a robust and fully vectorial mode solver developed by Photon Design. Then the refractive index profile is given by

$$\mathrm{n(z)} = \begin{cases} n_2, & 0 < z < l_2 \\ n_1, & l_2 < z < \Lambda \end{cases} \tag{7.2}$$

with

$$\mathrm{n(z)} = \mathrm{n(z + \Lambda)} \tag{7.3}$$

where l_2 is the length of the layer with refractive index n_2, $l_1 = \Lambda - l_2$ is the length of the layer with refractive index n_1, the z axis is along the propagation direction.

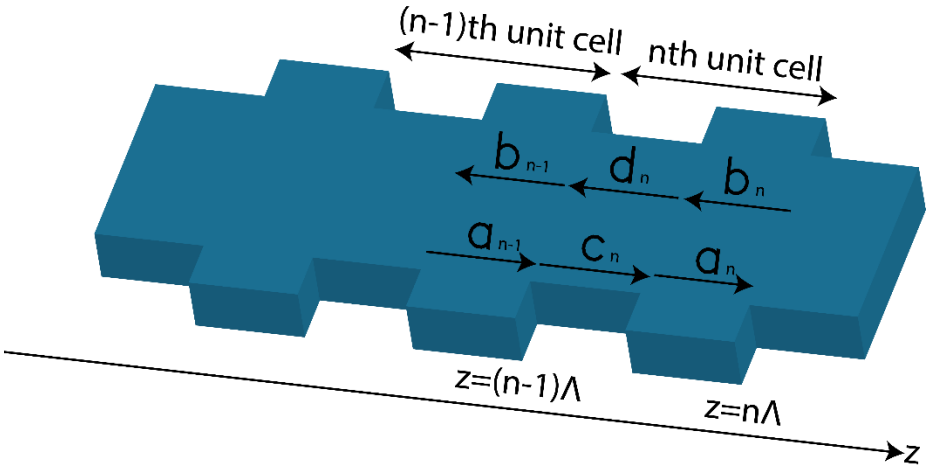

Figure 7.2 Complex amplitudes of the forward-travelling and backward-travelling plane waves in each layer.

Since the optical wave is guided within the waveguide, we can consider the light to propagate only in the z direction. A general solution to the wave equation can be formed by writing:

$$\vec{E}\,(z,t) = \vec{E}(z)e^{i\omega t} \tag{7.4}$$

The electric field within each layer can be expressed as a sum of a forward-traveling (+z) and a backward-travelling (-z) plane wave, see Figure 7.2,

$$\vec{E}(z) = \begin{cases} a_n e^{-ik_{1z}(z-n\Lambda)} + b_n e^{+ik_{1z}(z-n\Lambda)}, & n\Lambda - l_1 < z < n\Lambda \\ c_n e^{-ik_{2z}(z-n\Lambda+l_1)} + d_n e^{+ik_{2z}(z-n\Lambda+l_1)}, & (n-1)\Lambda < z < n\Lambda - l_1 \end{cases} \tag{7.5}$$

with

$$k_{1z} = \frac{n_1 \omega}{c} \tag{7.6}$$

$$k_{2z} = \frac{n_2 \omega}{c} \tag{7.7}$$

where n stands for the *n*th period, and a_n, b_n, c_n and d_n are constants that are related by the continuity conditions at the interfaces. Without loss of generality, we consider a TE-like mode, imposing the continuity of E_x and H_y at the interfaces $z = (n-1)\Lambda$ and $z = n\Lambda - l_1$, we obtain

$$\begin{gathered} a_{n-1} + b_{n-1} = c_n e^{ik_{2z}l_2} + d_n e^{-ik_{2z}l_2} \\ ik_{1z}(a_{n-1} - b_{n-1}) = ik_{2z}(c_n e^{ik_{2z}l_2} - d_n e^{-ik_{2z}l_2}) \\ c_n + d_n = a_n e^{ik_{1z}l_1} + b_n e^{-ik_{1z}l_1} \\ ik_{2z}(c_n - d_n) = ik_{1z}(a_n e^{ik_{1z}l_1} - b_n e^{-ik_{1z}l_1}) \end{gathered} \tag{7.8}$$

These four equations then can be rewritten as two matrix equations

$$\begin{bmatrix} 1 & 1 \\ ik_{1z} & -ik_{1z} \end{bmatrix} \begin{bmatrix} a_{n-1} \\ b_{n-1} \end{bmatrix} = \begin{bmatrix} e^{ik_{2z}l_2} & e^{-ik_{2z}l_2} \\ ik_{2z}e^{ik_{2z}l_2} & -ik_{2z}e^{-ik_{2z}l_2} \end{bmatrix} \begin{bmatrix} c_n \\ d_n \end{bmatrix} \tag{7.9}$$

$$\begin{bmatrix} 1 & 1 \\ ik_{2z} & -ik_{2z} \end{bmatrix} \begin{bmatrix} c_n \\ d_n \end{bmatrix} = \begin{bmatrix} e^{ik_{1z}l_1} & e^{-ik_{1z}l_1} \\ ik_{1z}e^{ik_{1z}l_1} & -ik_{1z}e^{-ik_{1z}l_1} \end{bmatrix} \begin{bmatrix} a_n \\ b_n \end{bmatrix} \tag{7.10}$$

The matrix notation indicates that the complex amplitudes of the forward-travelling and backward-travelling wave in each layer can be represented by a column vector. Adjacent column vectors are related by the continuity conditions at the interface. Note that the matrix elements for TM waves are slightly different from those of the TE waves, due to the different continuity conditions at the interface. At this point, we will treat these equations as two different problems, one is the simple periodic Bragg gratings as shown in Figure 7.1, another one is the complex waveguide Bragg gratings (CWBG).

7.2 Periodic Waveguide Bragg Gratings

In the periodic waveguide Bragg gratings, the alternating layers with two different refractive indices can be treated as a unit cell. The unit-cell translation matrix, which matrix relates the complex amplitudes of the plane waves in layer with index n_1 of a unit cell to those of the equivalent layer in the next unit cell, can be obtained by eliminating the column vector $\begin{bmatrix} c_n \\ d_n \end{bmatrix}$ in equation (7.9) and (7.10),

$$\begin{bmatrix} a_{n-1} \\ b_{n-1} \end{bmatrix} = \begin{bmatrix} A & B \\ C & D \end{bmatrix} \begin{bmatrix} a_n \\ b_n \end{bmatrix} \tag{7.11}$$

The matrix elements are

$$\begin{cases} A = e^{ik_{1z}l_1}[\cos k_{2z}l_2 + \frac{i}{2}(\frac{k_{2z}}{k_{1z}} + \frac{k_{1z}}{k_{2z}}) \sin k_{2z}l_2] \\ B = e^{-ik_{1z}l_1}[\frac{i}{2}(\frac{k_{2z}}{k_{1z}} - \frac{k_{1z}}{k_{2z}}) \sin k_{2z}l_2] \\ C = e^{ik_{1z}l_1}[-\frac{i}{2}(\frac{k_{2z}}{k_{1z}} - \frac{k_{1z}}{k_{2z}}) \sin k_{2z}l_2] \\ D = e^{-ik_{1z}l_1}[\cos k_{2z}l_2 - \frac{i}{2}(\frac{k_{2z}}{k_{1z}} + \frac{k_{1z}}{k_{2z}}) \sin k_{2z}l_2] \end{cases} \tag{7.12}$$

Wave propagation in a periodic medium is very similar to the motion of electrons in crystalline solids. In fact, the formulation of the Kronig-Penney model used in elementary energy band theory of solids is mathematically identical to that of the electromagnetic radiation in periodic layered media. According to the Bloch theorem, the electric field vector of a normal mode of propagation in a periodic Bragg grating is of the form

$$\vec{E} = \vec{E}_K(z)e^{-iKz}e^{i\omega t} \tag{7.13}$$

Where $\vec{E}_K(z)$ is a periodic function with period Λ, that is

$$\vec{E}_K(z) = \vec{E}_K(z + \Lambda) \tag{7.14}$$

The constant K is known as the Bloch wavenumber. The subscript *K* indicates that the function $\vec{E}_K(z)$ depends on *K*. From equation (7.5), in terms of the column vector representation, the above periodic condition (7.13) for the Bloch wave is simply

$$\begin{bmatrix} a_n \\ b_n \end{bmatrix} = e^{-iK\Lambda} \begin{bmatrix} a_{n-1} \\ b_{n-1} \end{bmatrix} \tag{7.15}$$

Then, considering the equation (7.11), the column vector of the Bloch wave satisfies the following eigenvalue problem:

$$\begin{bmatrix} A & B \\ C & D \end{bmatrix} \begin{bmatrix} a_n \\ b_n \end{bmatrix} = e^{iK\Lambda} \begin{bmatrix} a_n \\ b_n \end{bmatrix} \tag{7.16}$$

The phase factor exp(*iKΛ*) is thus the eigenvalue of the unit-cell translation matrix $\begin{bmatrix} A & B \\ C & D \end{bmatrix}$ and is given by

$$\cos(\mathrm{K}\Lambda) = \frac{1}{2}(A + D) \tag{7.17}$$

Regimes where $|(A + D)/2| < 1$ correspond to real *K* and thus to propagating Bloch waves; when $|(A + D)/2| > 1$, however, $\mathrm{K} = m\pi/\Lambda + iK_i$, which has an imaginary part K_i so that the Bloch wave is evanescent. These are the so-called photonic band gaps of the periodic Bragg grating.

For a periodic Bragg grating that consists of N unit cells, based on this unit-cell translation matrix, the column vector at the last period that represents the electrical field is related to that of the zeroth unit cell of the equivalent layer by

$$\begin{bmatrix} a_0 \\ b_0 \end{bmatrix} = \begin{bmatrix} A & B \\ C & D \end{bmatrix}^N \begin{bmatrix} a_N \\ b_N \end{bmatrix} \tag{7.18}$$

Since the unit-cell translation matrix is unimodular, the *N*th power of it can be simplified by using the following matrix identity,

$$\begin{bmatrix} A & B \\ C & D \end{bmatrix}^N = \begin{bmatrix} AU_{N-1} - U_{N-2} & BU_{N-1} \\ CU_{N-1} & DU_{N-1} - U_{N-2} \end{bmatrix} \tag{7.19}$$

where

$$U_N = \frac{\sin(N+1)\mathrm{K}\Lambda}{\sin \mathrm{K}\Lambda} \tag{7.20}$$

with

$$\mathrm{K} = \frac{1}{\Lambda}\cos^{-1}\left[\frac{1}{2}(A+D)\right] \tag{7.21}$$

Then, the reflection and transmission coefficients are given by

$$r_N = \left(\frac{b_0}{a_0}\right)_{b_N=0} = \frac{CU_{N-1}}{AU_{N-1}-U_{N-2}} \tag{7.22}$$

$$t_N = \left(\frac{a_N}{a_0}\right)_{b_N=0} = \frac{1}{AU_{N-1}-U_{N-2}} \tag{7.23}$$

separately, where $r_N = |r_N|\exp(-i\Psi)$ contains both the reflectance $|r_N|^2$ and the phase shift Ψ of the optical beam upon reflection, and $t_N = |t_N|\exp(-i\Phi)$ contains both the transmittance $|t_N|^2$ and the phase shift Φ of the optical beam upon transmission.

7.3 Complex Waveguide Bragg Gratings

In the complex waveguide Bragg gratings, there is no alternating layers with two different refractive indices. As shown in Figure 7.3, the refractive index profile along the propagation direction are generated to achieve targeted reflection or transmission

spectrum in different applications, such as integrated optical filter for any spectrum [81,82], enhanced thermo-optical interaction by slow light effect, and etc. In this case, it is not necessary to eliminate any column vector in equation (7.9) or (7.10) to simplify the model. In fact, using a sequence of equations derived from equation (7.9) or (7.10) to add up the layers is the most straightforward method.

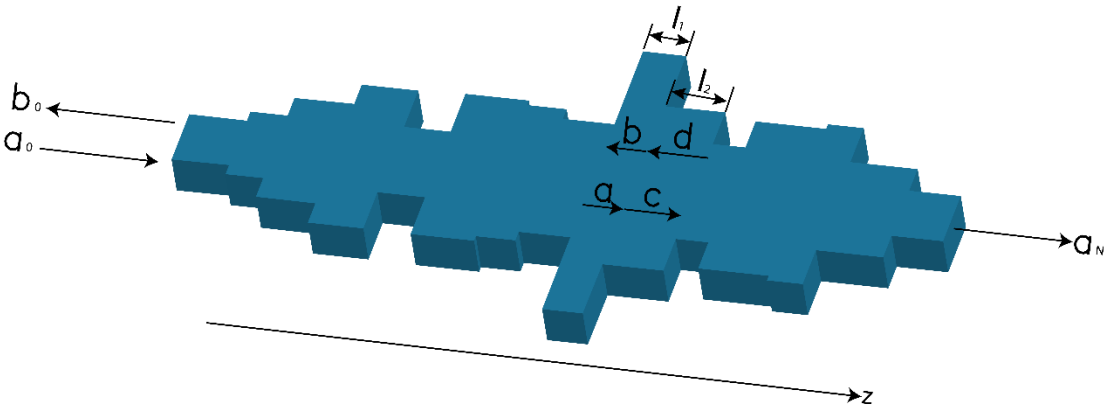

Figure 7.3 Schematic illustration of a complex waveguide Bragg grating.

From discussion in section 7.1, we note that, the complex amplitudes of the two plane waves in each layer is related to its adjacent layer by the continuity conditions at the interface. For TE waves, we have

$$\begin{bmatrix} 1 & 1 \\ ik_{1z} & -ik_{1z} \end{bmatrix} \begin{bmatrix} a \\ b \end{bmatrix} = \begin{bmatrix} e^{ik_{2z}l_2} & e^{-ik_{2z}l_2} \\ ik_{2z}e^{ik_{2z}l_2} & -ik_{2z}e^{-ik_{2z}l_2} \end{bmatrix} \begin{bmatrix} c \\ d \end{bmatrix} \tag{7.24}$$

where a and b are the forward-travelling and backward-travelling field amplitude at layer 1 in Figure 7.2, c and d are the forward-travelling and backward-travelling field amplitude at layer 2. By using the Cayley–Hamilton theorem to inverse the matrix on the left side, we obtain

$$\begin{bmatrix} a \\ b \end{bmatrix} = \begin{bmatrix} A & B \\ C & D \end{bmatrix} \begin{bmatrix} c \\ d \end{bmatrix} \tag{7.25}$$

where

$$\begin{cases} A = \frac{1}{2k_{1z}}(k_{2z} + k_{1z})e^{ik_{2z}l_2} \\ B = -\frac{1}{2k_{1z}}(k_{2z} - k_{1z})e^{-ik_{2z}l_2} \\ C = -\frac{1}{2k_{1z}}(k_{2z} - k_{1z})e^{ik_{2z}l_2} \\ D = \frac{1}{2k_{1z}}(k_{2z} + k_{1z})e^{-ik_{2z}l_2} \end{cases} \tag{7.26}$$

We note that equation (7.11) calculates *a* and *b* from the information of *c* and *d*, given the effective index and width in these two layers. Let us call $\begin{bmatrix} A & B \\ C & D \end{bmatrix}$ the transfer matrix T. Then, the overall transfer matrix of the complex grating is

$$T = T_N T_{N-1} T_{N-2} \cdots T_2 T_1 \tag{7.27}$$

Therefore

$$\begin{bmatrix} a_0 \\ b_0 \end{bmatrix} = T \begin{bmatrix} a_N \\ b_N \end{bmatrix} = \begin{bmatrix} T_{11} & T_{12} \\ T_{21} & T_{22} \end{bmatrix} \begin{bmatrix} a_N \\ b_N \end{bmatrix} \tag{7.28}$$

Then, the reflection and transmission coefficients are given by

$$r_N = \left(\frac{b_0}{a_0}\right)_{b_N=0} = \frac{T_{21}}{T_{11}} \tag{7.29}$$

$$t_N = \left(\frac{a_N}{a_0}\right)_{b_N=0} = \frac{1}{T_{11}} \tag{7.30}$$

The transfer matrix T is wavelength dependent, and the wavelength information is already embedded in the k_{1z} and k_{2z} parameters. In Figure 7.4, two examples are presented to demonstrate the calculated spectrum by using the transfer matrix T. One is a quarter-wave phase-shifted Bragg gratings, Figure 7.4 (a). A transmission peak is observed in the photonic band gap, a characteristic spectrum of the phase-shifted Bragg gratings.

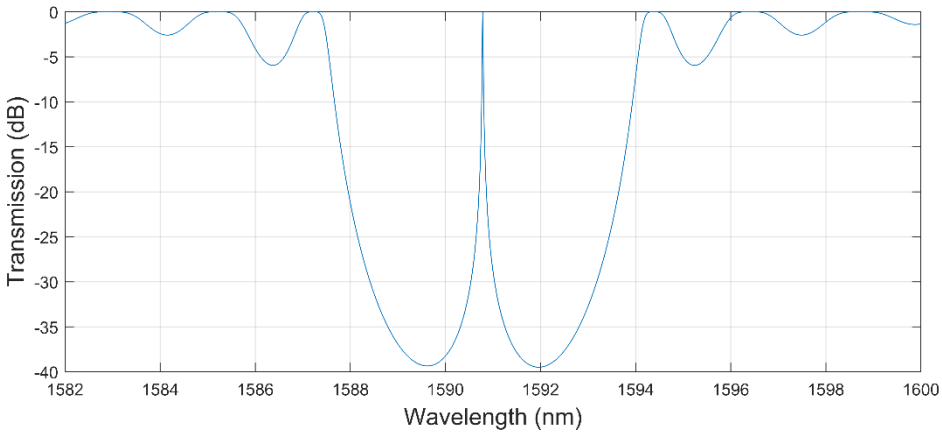

(a)

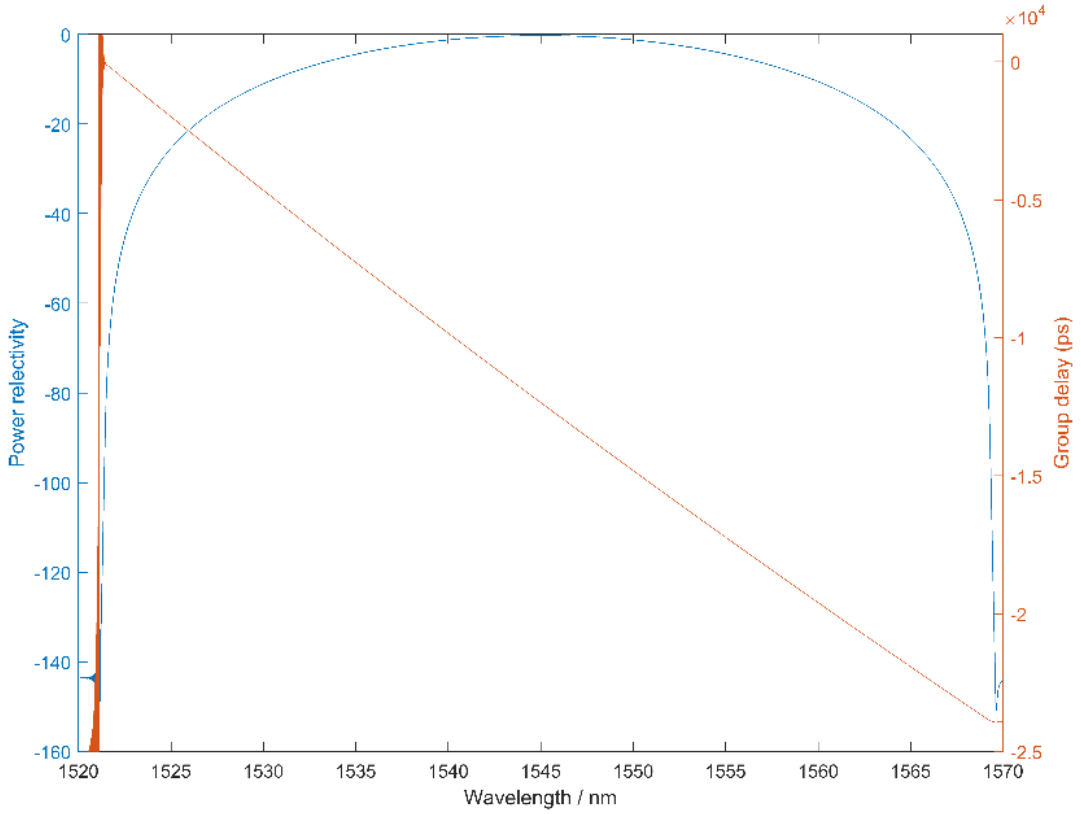

(b)

Figure 7.4 (a) Transmission spectrum of a quarter-wave phase-shifted Bragg grating. (b) Transmission and group delay of a complex Bragg grating.

Another example is a complex Bragg grating with over 400 ps/nm dispersion from 1520 nm to 1570 nm, Figure 7.4 (b). As we already know, the phase shift of the optical beam upon reflection and transmission is contained in the above complex reflection and transmission coefficient. So, the group delay can be derived from the phase shift by taking the derivative of it, which is of particular interest in some applications. The group delay in this example is very linear, and the wavelength ambiguity is smaller than 1 pm.

Chapter 8 High Rejection Ratio Pump Filter

Integrated photonic circuits have become an important approach to generate quantum light, such as entangled photon pairs and heralded single photons as resources for quantum information processing [83,84]. Photon-pair generation using the nonlinear optical process of spontaneous four-wave mixing (SFWM) by integrated photonic structures, like waveguides and micro-resonators, has been widely studied [85,86]. Due to its lower nonlinear losses originating from two-photon absorption (TPA) and free carrier absorption compared to silicon, and reasonably high nonlinear coefficient, silicon nitride is a promising platform for photon-pair generation via SFWM. Despite the high nonlinear coefficient, it still requires a strong laser field to pump silicon nitride to generate photon-pairs, which makes the filtering of the pump field essential to isolate the weaker signal and idler fields. In general, it requires an extinction ratio larger than 100 dB. However, it has never been achieved without using off-chip filters. Efficient on-chip rejection of the pump light is a challenge in quantum optics.

An integrated high rejection ratio pump filter using a simple periodic waveguide Bragg grating will be demonstrated in this chapter. We will introduce an efficient z-shape waveguide design to achieve 83 dB filtering of the pump field by suppressing another supported TM mode in the waveguide and avoiding scattered modes at the output port.

8.1 Waveguide and Bragg Grating Design

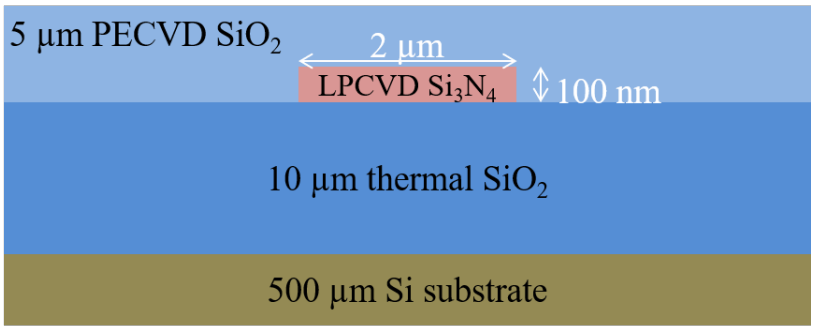

Figure 8.1 Waveguide cross section illustration.

As shown in Figure 8.1, on top of the 500 μm silicon substrate, a 10 μm thermal silicon dioxide (SiO_2) layer is formed as the lower cladding of the waveguide. The waveguide core, which is formed by low pressure chemical vapor deposition (LPCVD) silicon nitride (Si_3N_4) and patterned by a 100 keV Elionix ELS-G100 e-beam system, is chosen to be 2 μm × 100 nm due to its reasonable confined mode and low propagation loss [87]. Then, another 5 μm SiO_2 is deposited by plasma-enhanced chemical vapor deposition (PECVD) as the upper cladding layer. A fiber-to-waveguide coupler with ultra-high butt coupling efficiency (98% in theory and 96% in experiment by using UHNA3 fiber) based on an inversed taper is used at both ends of the waveguide [88], see Figure 8.2.

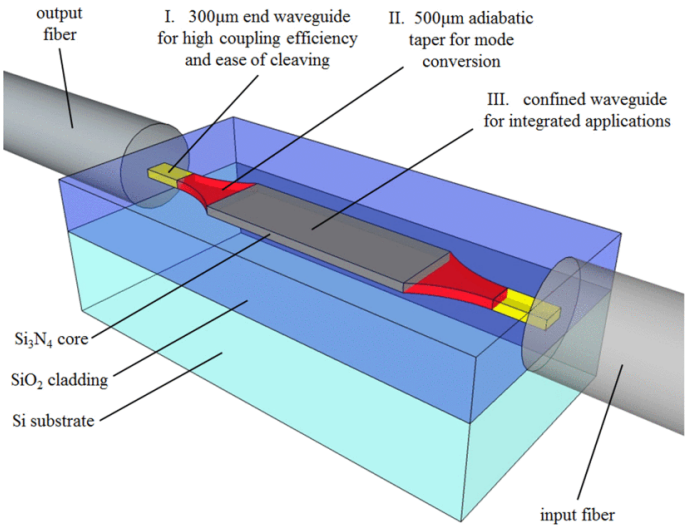

Figure 8.2 Diagram of the Si_3N_4 /SiO_2 fiber-to-waveguide coupler [88].

A single grating period is formed by two segments (w_1 = 2 μm, w_2 = 4 μm) with Λ = 0.536 μm, see Figure 8.3. The total length of the Bragg gratings is 1072 μm, which correspond to 2000 periods.

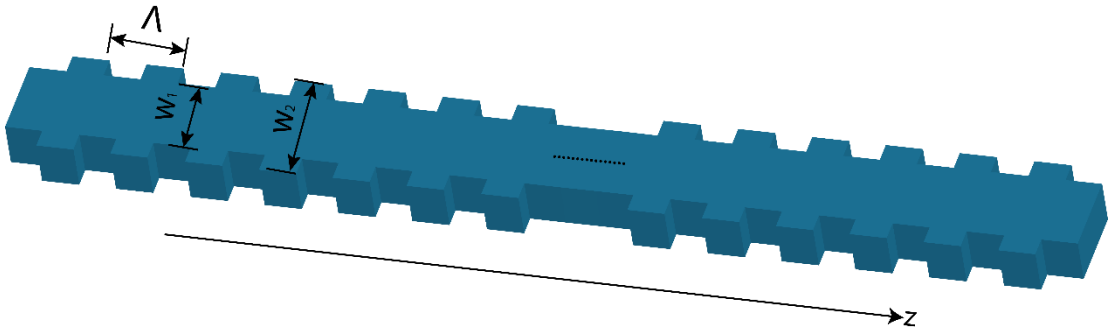

Figure 8.3 Illustration of the periodic Bragg grating.

We will discuss several factors that would prevent observing deep bottom level inside the photonic band gap of the Bragg gratings, such as direct coupling of the leakage

light from input to output fibers, second guided mode in the waveguide, scattering to cladding modes due to mode mismatch and spontaneous emission of the laser source.

8.2 Coupling between Input and Output Fibers

Even with our high-efficiency fiber to waveguide coupler design, small amount of the power will not be coupled into the waveguide, which will be either reflected, or coupled into cladding modes. The signal that carried in the cladding modes will propagate along the chip and finally couple with the output fiber. Let us define the distance between the input and output fibers in the perpendicular direction to its propagation direction as the “offset” value. When the input and output fibers point to each other, this means there is no offset, see Figure 8.4 (a) for details.

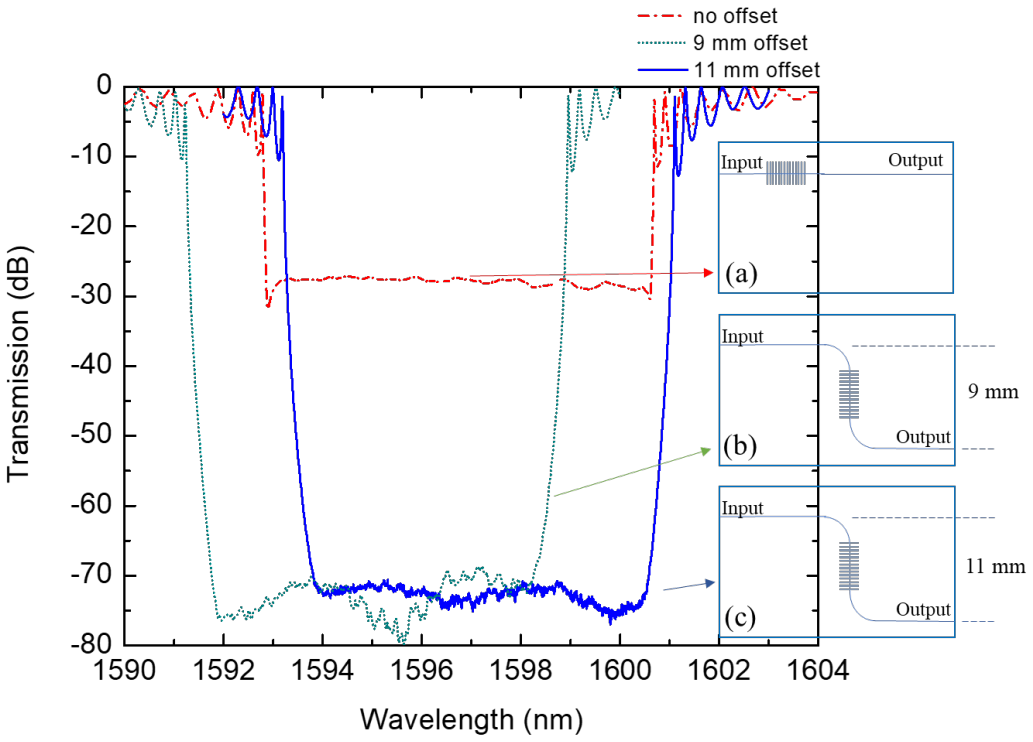

Figure 8.4 Transmission spectra of (a) no offset between the input and output fibers, (b) and (c) the offset between the input and output fibers is 9 mm and 11 mm separately.

The width of the chip shown in Figure 8.4 is 15 mm. The only difference between the device (a), (b) and (c) in the above figure is the offset values. To control another parameter, the bending losses of TE and TM modes, which will be discussed in the following section, some bending curvatures are intentionally added in the device (a) to emphasize the effect of the offset value. Based on the measured transmission spectra, we can conclude that, the ratio between the background light coupled directly from the input to the output fibers and the total input power in device (a) is around -30 dB. Comparing devices (b) and (c), it is clear that the transmission inside the band gap is similar. This indicates that the limitation that prevents us to observe smaller

signal is not the coupling between the input and output fibers when the offset is beyond 9 mm.

So, unless we can implement a 100% coupling efficiency design, it is necessary to introduce some offset between the input and output fibers in order to minimize the coupling of transmitted light.

8.3 Guided TM Mode

The waveguide design shown in Figure 8.1 supports both fundamental TE and TM modes. To better control the polarization in the waveguide, we use a PM1550 fiber instead of the UHNA3 fiber. The fiber-to-waveguide butt coupling efficiency of the PM1550 fiber is slightly smaller than that of the UHNA3 fiber due to its larger mode size. The coupling efficiency of the TE mode is 80.3%, while the coupling efficiency of the TM mode is 84%, which means that when the light is coupled from the input fiber, both modes will be excited. Keysight 81600B, the tunable laser source in our setup, has a typical polarization extinction ratio of 16 dB, and the TE mode is in the slow axis and in line with the connector key. Also, the misalignment between the slow axis of the input fiber and the on-chip waveguide is inevitable, since the angle of the input fiber is manually controlled. Let us assume that we can minimize the angle error to 1 degree, which is already quite impressive. In this case, we still face about 17.6 dB polarization extinction ratio. From the above, we can conclude that the TM mode in the waveguide will carry around -16 dB of the total power coupled from the input fiber.

The TE mode and TM mode will react differently to the same Bragg grating due to the different mode size and the effective refractive index. For example, in the platform we introduced in section 8.1, if we design a periodic Bragg grating to have a photonics band gap centered at 1600 nm wavelength for the TE mode, we will usually see the TM mode with a band gap shifted to the higher energy side. This means that, without suppression or filtering of the TM mode, there will be around -16 dB power transmitted within the photonic band gap. This type of background level is not acceptable to measure any small signals in integrated phonics, like photon-pair generation via spontaneous four-wave mixing.

Several methods can be implemented to significantly improve the polarization extinction ratio of the device. Depending on the properties of the TE and TM modes in the platform, different methods should be considered.

8.3.1 Bend Mode Loss

In the 100-nm thick and 2-um wide Si_3N_4 waveguide with SiO_2 cladding on both the bottom and top, the easiest way to suppress TM mode is to use the fact that the TE and TM modes have different bending loss as the bending radius changes. Figure 8.5 plots the transmission of TE and TM modes as a function of the bending radius when they propagate through a 90-degree bend structure as shown in the inserted figure.

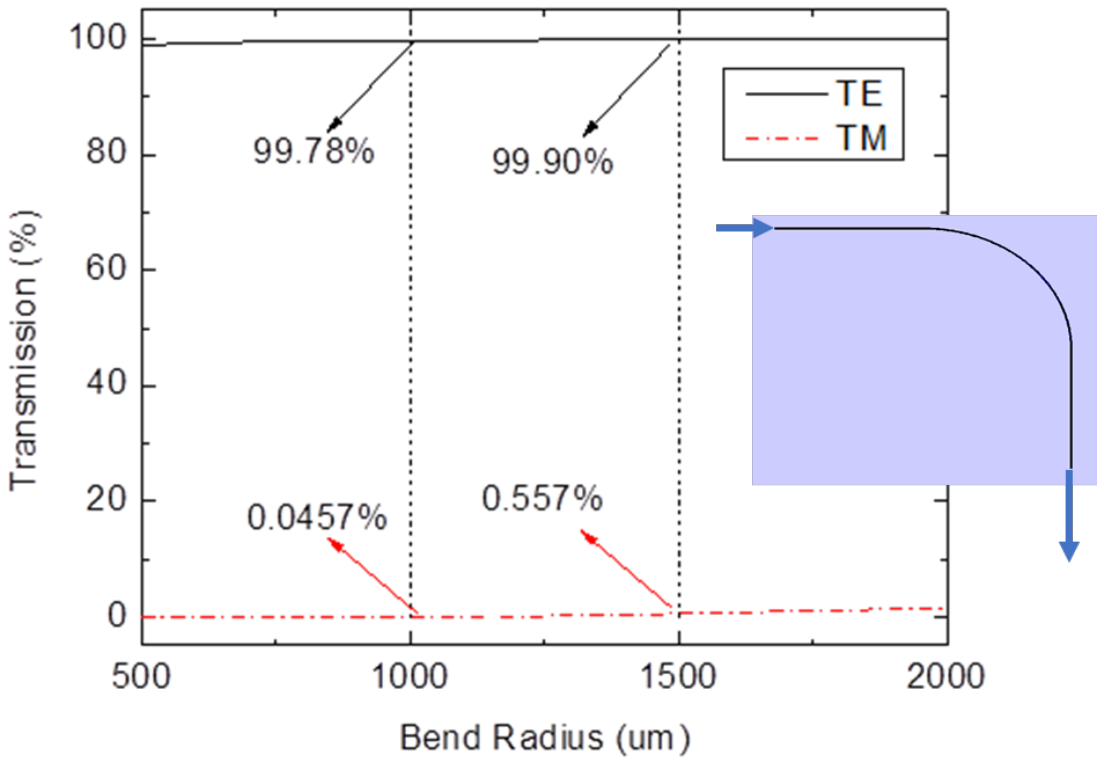

Figure 8.5 Calculated transmission of TE and TM modes as a function of the bending radius when they propagate through a 90-degree bending structure in 100-nm thick and 2-um wide Si_3N_4 waveguide.

This method is very useful if the size of the TM mode is much larger than that of the TE mode. Based on the simulation results of FIMMWAVE, the effective mode size of TM mode is 10.12 μm^2, while the effective mode size of TE mode is 4.34 μm^2. The TM mode is much more weakly guided comparing to TE mode, which makes it easy to bend the light to the outer side (right side in Figure 8.6) when propagating along a bending curvature. Figure 8.6 shows the simulated TE and TM bend modes when the light is propagated along a bend of 1000 μm bending radius. As we can see,

the TE mode is still confined well inside the Si_3N_4 core, while the TM modes is radiating to the right side.

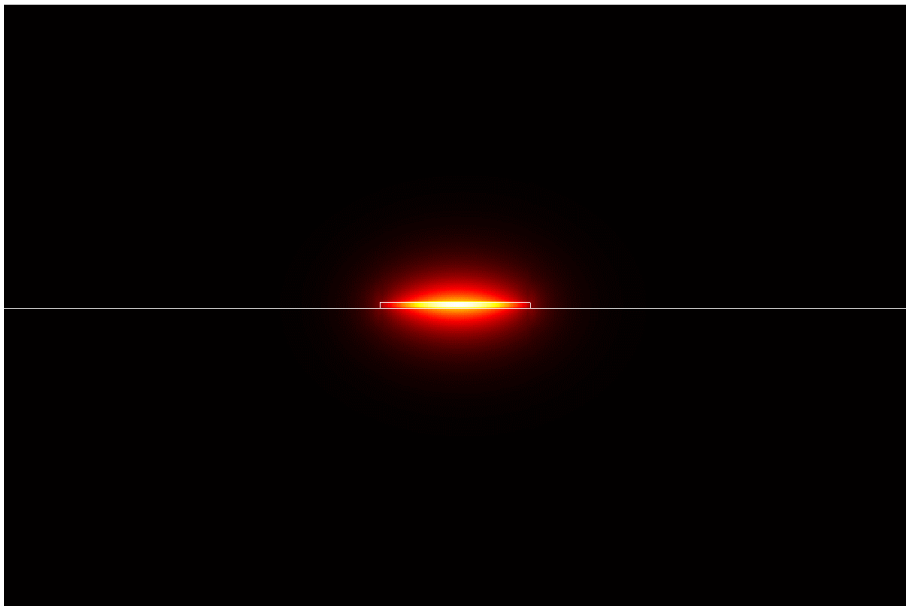

(a)

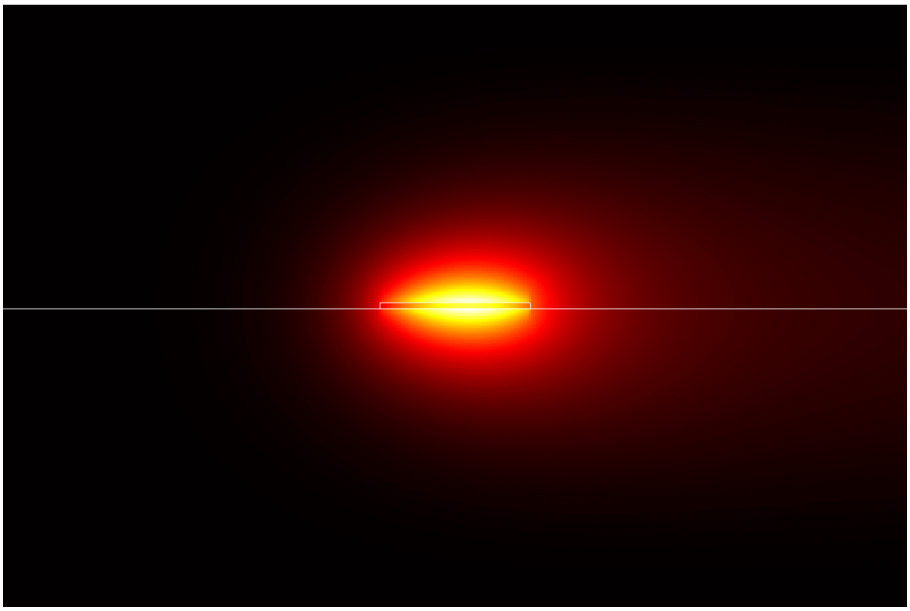

(b)

Figure 8.6 The simulated (a) TE and (b) TM bend modes when propagated along a bend of 1000 μm bending radius.

Two samples have been made to compare the performance of the bending structures. We cannot use a device without any bending curvature. In this case we must consider two factors: 1) the coupling between the input and output fibers and 2) the guided TM mode. So, we choose to add bend curvatures with bending radius of 1000 µm and 1500 µm separately (see insert in Figure 8.7).

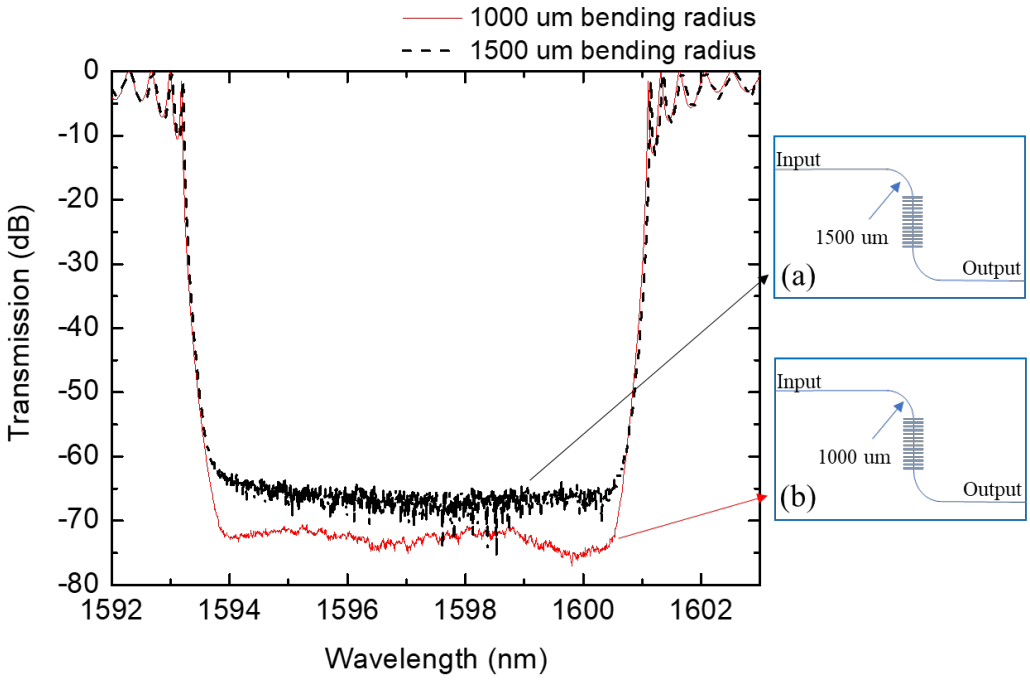

Figure 8.7 Transmission spectra of (a) a device with bending radius of 1500 µm (b) a device with bending radius of 1000 µm.

From the simulation data in Figure 8.5, the two 90-degree bend curvatures with bending radius of 1000 µm will provide an additional 67 dB polarization extinction ratio, while that with bending radius of 1500 µm will provide an additional 46 dB polarization to the extinction ratio. It is worth mention that, TE mode losses in both structures are negligible. With the additional 16 dB extinction ratio provided by the

tunable laser source and manual rotation of the PM1550 fiber, we expect total 62 dB and 83 dB polarization extinction ratio separately for device (a) and (b). In these devices, offset between input and output fibers is set to 11 mm to reduce the direct coupling between them. As we can see in Figure 8.7, the bottom level inside the photonic band gap of device (a) is around -63 dB, which agrees with the expectation. This means that the guided TM mode is still limiting the rejection ratio of our Bragg grating. On the other hand, device (b) doesn't have a band gap that is as low as predicted (-83 dB). Instead, only 73dB rejection ratio was observed. Same as discussed in Figure 4, this indicates that the limitation that prevents us from getting higher rejection ratios is not the guided TM mode, in particular, if we implement two 90-degree bending structures with radius of 1000 μm.

8.3.2 Pre-filtering the TM Grating

When the bend mode losses of TE and TM modes are very close, it is not practicable to use bending curvature to improve the polarization extinction ratio. For example, in the 300-nm thick and 1-um wide Si_3N_4 waveguide with SiO_2 cladding on both the bottom and top, both TE and TM modes are well confined. As we can see in Figure 8.8, if the bending radius is chosen to have a high TM bend mode loss, it will also suffer a relatively high TE bend mode loss.

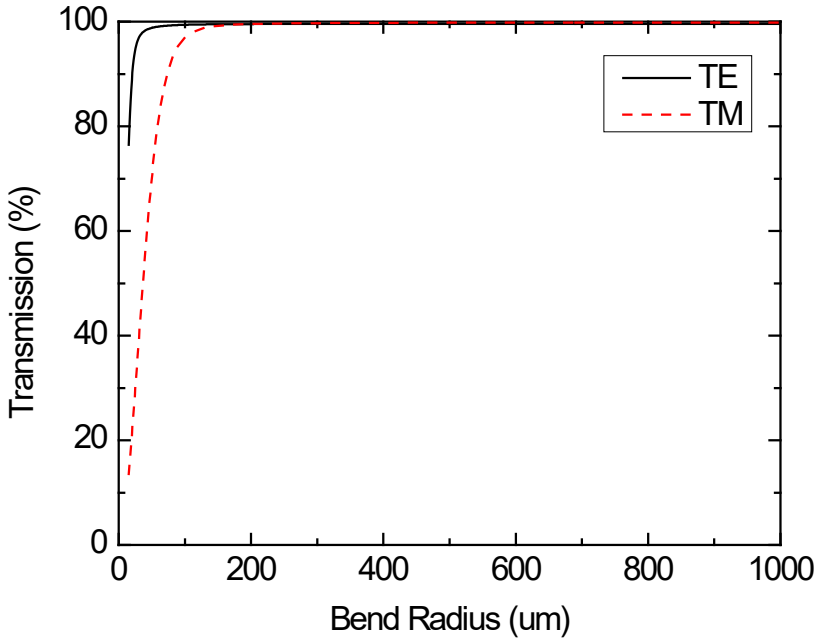

Figure 8.8 Calculated transmission of TE and TM modes as a function of the bending radius when they propagate through a 90-degree bending structure in 300-nm thick and 1-um wide Si_3N_4 waveguide.

In this situation, another periodic Bragg grating that is designed to filter the TM mode within the band gap is implemented. We are able to engineer this TM Bragg grating to provide a band gap that cover the wavelength range that we are interested, so that lower bottom level can be achieved at every wavelength within that range. The easier way to engineer the TM Bragg grating is that, first find a reasonable set of w_1 and w_2 value, then, with w_1 and w_2 being fixed, change the period of the grating to match the band gap. Figure 8.9 shows the transmission spectra of a device that implement a pre-filtering TM grating with TE or TM input. Only the wavelength range where both band gap of TE and TM gratings are covered shows high rejection ratio. Outside this region, the transmission averages -16 dB within the photonic band gap of the TE and

TM grating. It is interesting to notice that the shapes of both transmission spectra are similar in the two circled area in Figure 8.9. In fact, this is evidence which proves that the polarization extinction ratio of our setup itself, including the tunable laser source and manual rotation of the PM1550 fiber, is around 16 dB.

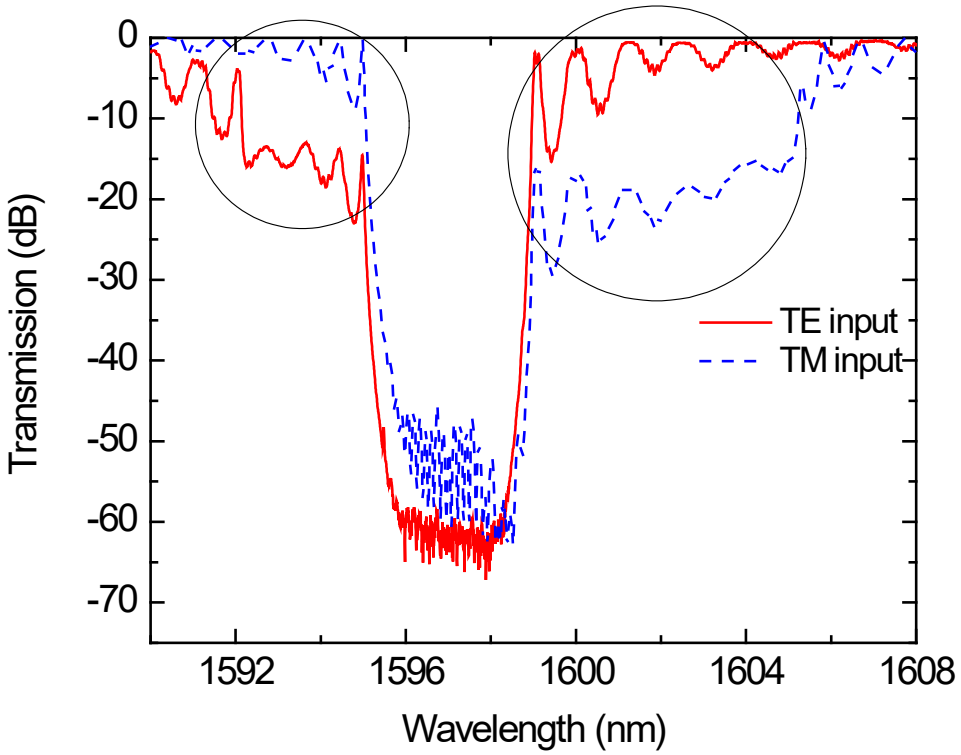

Figure 8.9 Transmission spectra of a device that implementing a pre-filtering TM grating with TE or TM input.

8.4 Mode Mismatch

To further improve the rejection ratio of the periodic Bragg grating, we studied the mode mismatch between the fundamental mode in the straight waveguide and Bloch mode in the grating. Within the photonic band gap, according to equation (7.13), the evanescent field inside the Bragg grating is

$$\vec{E} = \vec{E}_K(z)e^{-iKz}e^{i\omega t}$$

where $K = m\pi/\Lambda + iK_i$. The imaginary part K_i is the attenuation constant. In this case, the field can be expressed as $e^{-i\beta_{Bragg}z}\exp(-K_i z)$, where $\beta_{Bragg} = m\pi/\Lambda$ is the effective propagation constant in the periodic Bragg grating. The field inside the straight waveguide region can be represented as $e^{-i\beta_{wg}z}$. It is well known that mode mismatch at the interface will introduce coupling loss due to scattering [89,90].

By simulating the electrical field propagating through a Bragg grating using the FDTD method (see Figure 8.10), we realize that the field scattered by the waveguide-grating interface has certain propagation directions. The relation between the direction of the grating and the position of output port will affect the transmitted signal collected at the output fiber, and further affect the rejection ratio. Based on this observation, a new z-shape device design is introduced here, as shown in Figure 8.11(b). The transmission spectra of both the new and the normal structure are measured and plotted in Figure 8.11. With the implementation of the z-shape design, the rejection ratio has improved from 73 dB to 83 dB, which indicates that the output fiber receives a smaller amount of scattered light originating from the interface, since it is located along the normal line to the grating at its center.

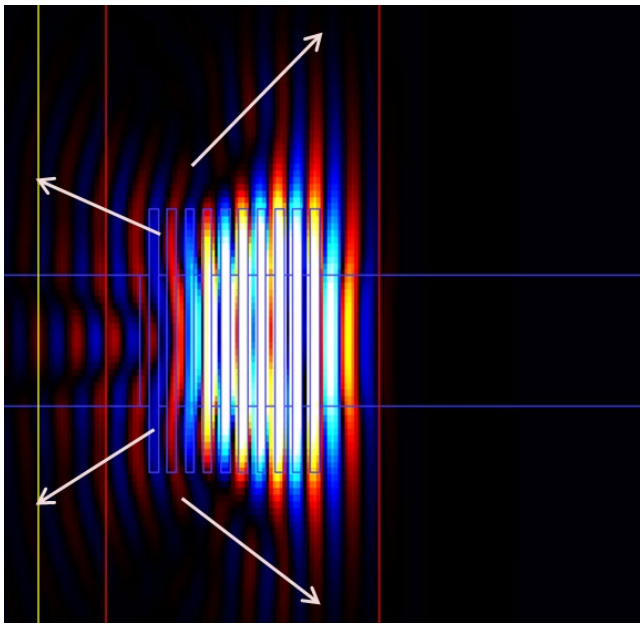

Figure 8.10 FDTD simulation result of electrical field propagation through waveguide/Bragg grating interface.

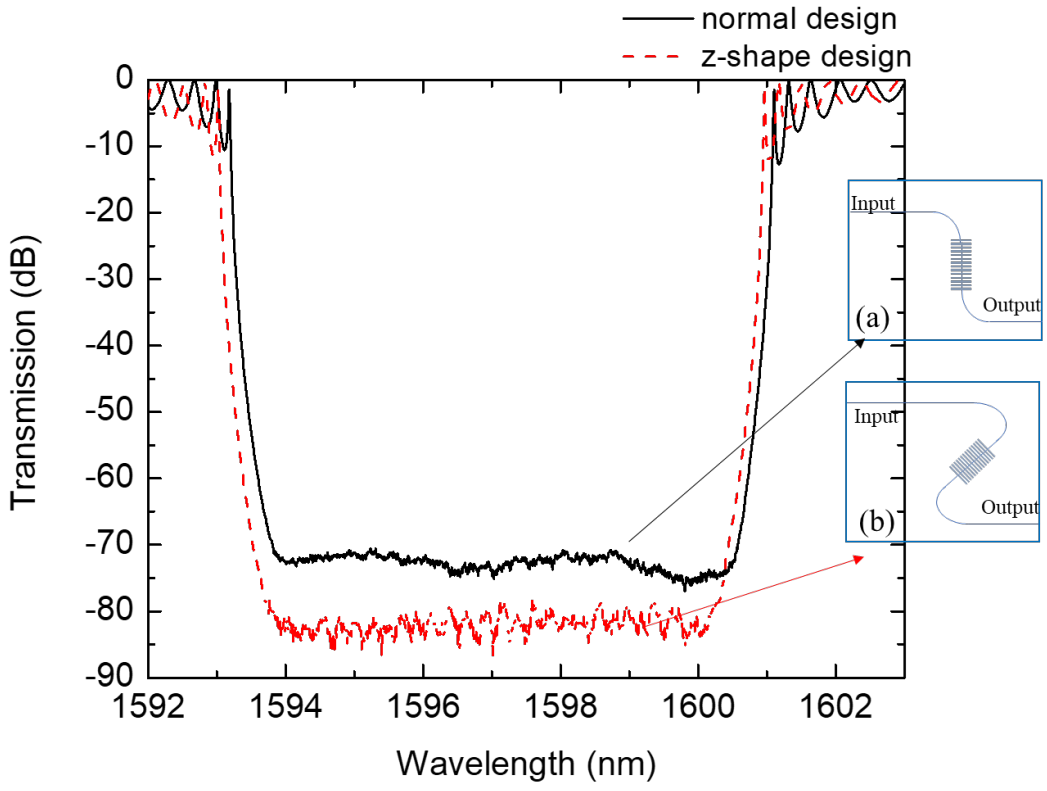

Figure 8.11 Transmission spectra of (a) a device with normal design (b) a device with z-shape design.

8.5 Potential Improvement

To better control the scattered light on the chip, phase matching between the grating and the waveguide, $\beta_{Bragg} = \beta_{wg}$, is necessary. It will minimize the scattering loss at the waveguide-grating interface. A tapered grating can be inserted at each waveguide-grating interface, see Figure 8.12, to adiabatically convert the Bloch mode into the waveguide mode.

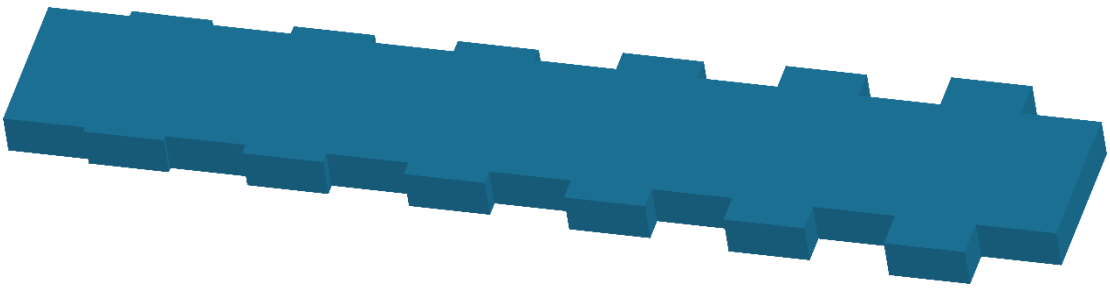

Figure 8.12 Schematic illustration of a taper Bragg grating.

Chapter 9 Fabry-Perot Cavity Enhanced Four-Wave Mixing

In the recent past decades, four-wave mixing (FWM) has become an important optical parametric process that has attracted increased interest. The effect of FWM has enabled useful applications for all-optical signal processing such as high-speed sampling, switching, wavelength conversion, amplification and comb generation [91–95]. The FWM effect can be dramatically increased when using resonates, without compromising speed because of their small dimensions (or the order of micrometers) [95–97].

There is also a great amount of interest in exploring nonlinear materials as an alternative to silicon, since the nonlinear losses originating from two-photon absorption (TPA) and free carrier absorption at telecom wavelengths limit the maximum power that can be sent in silicon. Silicon nitride stands out as one of the promising candidates as it can take advantage of the mature technologies of the CMOS processing platform for integrated optics, which makes the mass production possible and thus tremendously reduces processing costs. The availability of low-loss dielectric waveguide (<1 dB/m) is critical for light propagation and processing in integrated photonics circuits. The nonlinear Kerr coefficient of silicon nitride is one order of magnitude greater than the one in silicon dioxide, a more efficient Kerr process can be achieved. In addition, due to the smaller refractive index contrast with silicon dioxide, silicon nitride is a more appropriate material for dispersion engineering than silicon, since typical fabrication inaccuracies will have lower impact on dispersion.

This chapter will study the Fabry-Perot cavity enhanced FWM, from analytical derivations and experimental demonstrations. A numerical model based on previously presented ABCD matrix method of Bragg grating will be developed to optimize the structural design of Fabry-Perot cavity enhanced FWM device.

9.1 Waveguide and Bragg Grating Design

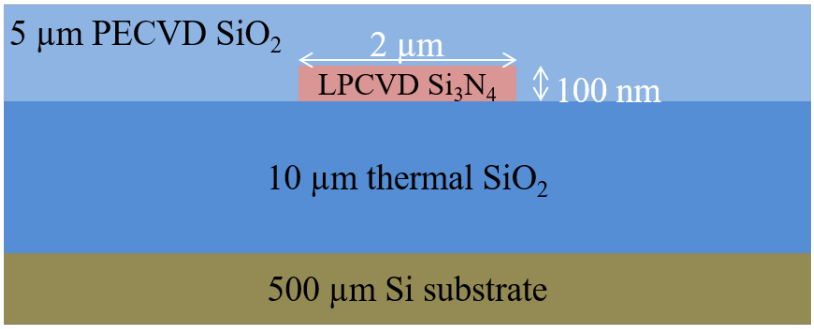

Figure 9.1 Waveguide cross section illustration.

As shown in Figure 9.1, we use a silicon nitride waveguide core cross section with a height of 100 nm and a width of 2 μm. The propagation loss is as low as 0.1 dB/cm [87]. A 10 μm thermal silicon dioxide layer works as the lower cladding of the waveguide, while another 5 μm silicon dioxide is deposited by plasma-enhanced chemical vapor deposition (PECVD) as the upper cladding layer. A fiber-to-waveguide coupler with ultra-high butt coupling efficiency (98% in theory and 96% in experiment by using UHNA3 fiber) based on an inversed taper is used at both ends of the waveguide [88], see Figure 8.2.

The dimension of the silicon nitride waveguide core not only leads to a low propagation loss, but also to a relatively low dispersion. As we know, in resonating systems, the FWM effect can be optimized only when the input and generated waves are matched to the resonator cavity's longitudinal modes. In practice, chromatic dispersion will lead to a mismatch between the converted frequency and the resonant frequency of the cavity. So, in most nonlinear applications, including FWM, the most suitable dispersion is low and anomalous. The chromatic dispersion, D, can be shown as,

$$\mathrm{D} = -\frac{\lambda}{c}\frac{d^2 n_{eff}}{d\lambda^2} \tag{9.1}$$

where λ is the wavelength, c is the speed of light, and n_{eff} is the effective refractive index. n_{eff} is calculated for the TE mode of the designed silicon nitride waveguide by FIMMWAVE. The contribution of material dispersion to the total dispersion is calculated by using the silicon nitride refractive index dependence on wavelength in Equation (9.1). A simple geometrical optimization can be applied to achieve dispersion engineering [98,99]. Figure 9.2 shows the dispersion value of the fundamental TE mode in silicon nitride waveguide at wavelength of 1590 nm, as a function of the width and height of the core. To achieve zero or anomalous dispersion, the height of the core is required to be at least 700 nm, together with a width wider than 1 um. However, depositing thick films of stoichiometric silicon nitride without forming cracks can be a challenging task due to the buildup of stress. So far, in our lab, high quality silicon nitride thin film can be deposited by LPCVD as thick as 300 nm.

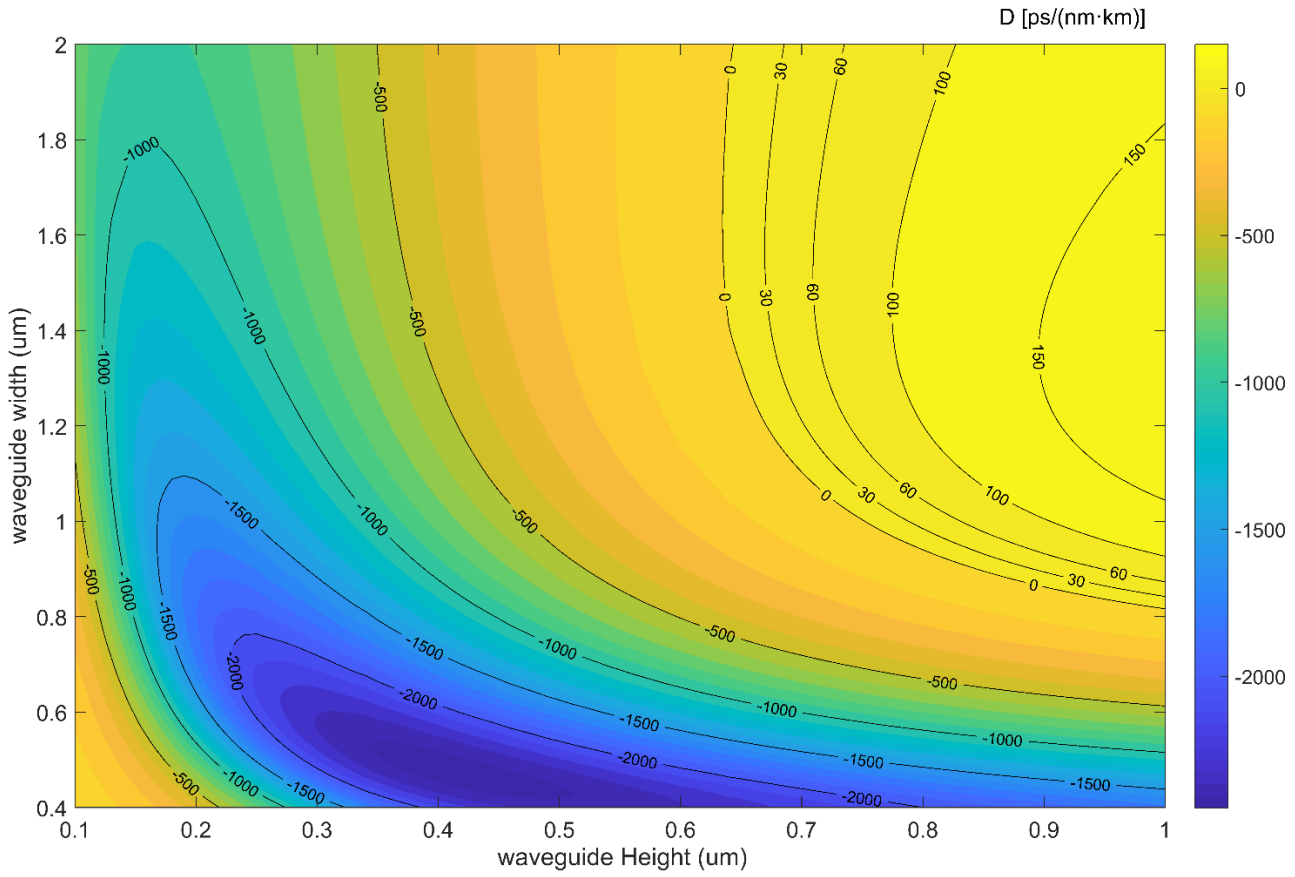

Figure 9.2 Dispersion of fundamental TE mode in silicon nitride waveguide at wavelength of 1590 nm, as a function of the width and height of the core.

By comprehensively considering the propagation loss, dispersion engineering and the number of propagating modes supported, a silicon nitride waveguide core with a height of 100 nm and a width of 2 μm is chosen.

9.2 Four-Wave Mixing in Fabry-Perot Cavity

9.2.1 Four-Wave Mixing without Enhancement

We first consider the FWM effect inside a waveguide that has a length of L without the field enhancement. The field amplitudes of the pump wave E_p, the signal wave E_s, and the converted FWM wave E_c satisfy the following nonlinear propagation equations, for $\lceil E_p \rceil \gg \lceil E_s \rceil \gg \lceil E_c \rceil$ (small-signal analysis) [100],

$$\frac{\partial E_p}{\partial z} = -\frac{\alpha_p}{2} E_p \tag{9.2}$$

$$\frac{\partial E_s}{\partial z} = -\frac{\alpha_s}{2} E_s \tag{9.3}$$

$$\frac{\partial E_c}{\partial z} = -\frac{\alpha_c}{2} E_c + i\gamma E_p^2 E_s^* e^{i\,\Delta k z} \tag{9.4}$$

where E_s^* is the complex conjugate of E_s, and

$$\Delta k = 2k_p - k_s - k_c \tag{9.5}$$

where k_p, k_s, k_c are the propagation constants of the pump, the signal and the converted wave respectively. The nonlinear coefficient γ is related to the Kerr coefficient n_2, effective mode size A_{eff} and the converted frequency ω_c by,

$$\gamma = \frac{n_2 \omega_c}{A_{eff} c} \tag{9.6}$$

For relatively small pump-signal frequency detuning in our case, we can assume a constant propagation loss coefficient, that is $\alpha \approx \alpha_p \approx \alpha_s \approx \alpha_c$. Since there is no converted wave generated at $z = 0$, where the pump and signal are sent in, by applying boundary conditions $E_p(z = 0) = E_{p0}$, $E_s(z = 0) = E_{s0}$, $E_c(z = 0) = 0$,we get

$$E_p = E_{p0}e^{-\frac{\alpha}{2}z} \tag{9.7}$$

$$E_s = E_{s0}e^{-\frac{\alpha}{2}z} \tag{9.8}$$

$$E_c = \frac{i\gamma E_{p0}^2 E_{s0}}{\alpha - i\Delta k}(1 - e^{-\alpha z + i\Delta k z})e^{-\frac{\alpha}{2}z} \tag{9.9}$$

Equation (9.9) is the solution of a first order linear Ordinary Differential Equation (ODE). Thus, by the definition of FWM conversion efficiency,

$$\eta = \frac{P_c^{out}}{P_s^{in}} = \left|\gamma P_p L'\right|^2 \tag{9.10}$$

where,

$$L'^2 = L^2\, exp(-\alpha L)\left|\frac{1 - exp(-\alpha L + i\Delta k L)}{\alpha L - i\Delta k L}\right|^2 \tag{9.11}$$

9.2.2 Field Enhancement in a Fabry-Perot Cavity

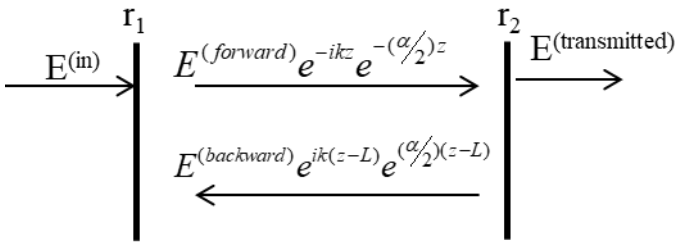

Figure 9.3 Electric fields in a Fabry-Perot resonator.

Figure 9.3 illustrates the electric fields in a Fabry-Perot resonator when an electric field $E^{(in)}$ is incident upon mirror 1. Inside the cavity, there are the forward-traveling wave and the backward-traveling wave, which can be represented as follow:

$$E^{(forward)} = t_1 E^{(in)} + r_1\, exp(-\alpha L/2 - ikL) E^{(backward)} \tag{9.12}$$

$$E^{(backward)} = r_2\, exp(-\alpha L/2 - ikL) E^{(forward)} \tag{9.13}$$

r_1, r_2 are the electric-field mirror reflectivities, and t_1, t_2 are the electric-field mirror transmittivities. They satisfy $|r|^2 + |t|^2 \approx 1$, neglecting the propagation loss due to the mirrors. Solving the above equation, we get,

$$\left|\frac{E^{(forward)}}{E^{(in)}}\right| = \left|\frac{t_1}{1 - r_1 r_2\, exp(-\alpha L - i2kL)}\right| \tag{9.14}$$

$$\left|\frac{E^{(backward)}}{E^{(in)}}\right| = \left|\frac{E^{(forward)}}{E^{(in)}} \cdot r_2 e^{-i2kL} e^{-\alpha L/2}\right| \tag{9.15}$$

According this solution, the field enhancement of the pump, the signal and the converted wave can be expressed as,

$$\begin{aligned} FE_i^2 &= \left|\frac{E^{(forward)}}{E^{(in)}}\right|^2 + \left|\frac{E^{(backward)}}{E^{(in)}}\right|^2 \\ &= \left|\frac{t_1}{1 - r_1 r_2\, exp(-\alpha L - i2k_i L)}\right|^2 \left(1 + \left|r_2 e^{-\alpha L/2}\right|^2\right) \end{aligned} \tag{9.16}$$

where *i* can be substituted by *p, s,* and *c*. The field enhancement is maximized at resonant frequencies, that is

$$2k_i L = 2m\pi, \quad m = any\ integer \tag{9.17}$$

So, the small-signal FWM conversion efficiency enhanced by a Fabry-Perot cavity is finally given by

$$\eta = \left|\gamma P_p L'\right|^2 FE_p^4 FE_s^2 FE_c^2 \tag{9.18}$$

It contains all the physics of both FWM and the resonator. The first factor, $\left|\gamma P_p L'\right|^2$, is the FWM conversion efficiency in a straight waveguide with a physical length of L. The effective length L' contains both the phase mismatch and the propagation loss. The last three factors, $FE_p^4 FE_s^2 FE_c^2$, state the field enhancement inside the cavity for the pump, the signal, the converted wave, respectively. The enhancement comes equally from light recirculation and energy buildup.

9.3 Numerical Model Based on ABCD Matrix Method

9.3.1 Numerical Model

In chapter 7, we introduced the ABCD matrix method, which is capable to calculate the complex transmission and reflection spectrum of any type of Bragg gratings. Considering that, in the FWM conversion efficiency Equation (9.18), the reflectivity and transmittivity of the two mirrors is the only unknown variables, it would be perfectly suitable to use the ABCD matrix to bridge the physical parameters to them.

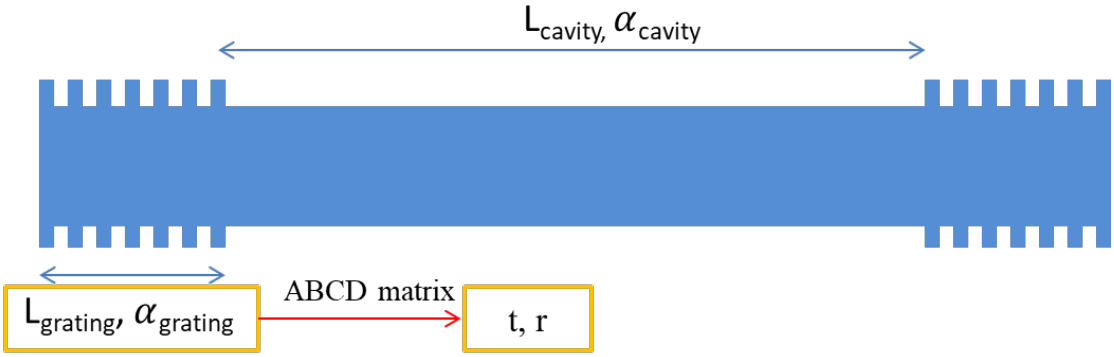

Figure 9.4 Fabry-Perot cavity with two identical periodic Bragg gratings on two sides. Use ABCD matrix to convert $L_{grating}$ and $\alpha_{grating}$ to t and r.

As shown in Figure 9.4, the model is a Fabry-Perot cavity with two identical periodic Bragg gratings on the two sides. The two Bragg gratings work as mirrors. And the reflectivity and transmittivity depend on the geometrical design of them. The width difference between w_1 and w_2, see Figure 7.1, determines the bandwidth of the photonic band gap. The number of periods, equivalently the length of the grating, affects the reflectivity. To measure the small losses, $\alpha_{grating}$ and α_{cavity}, we use a novel approach developed in our lab [87]. This method is based on measuring the transmission of a Fabry-Perot cavity formed by two highly reflective Bragg gratings and a uniform waveguide between the two gratings whose length can be varied to increase the loss fitting accuracy. A theoretical model based on an ABCD matrix method is developed and used for the final loss value fitting. Also, as we discussed in section 8.4, the scattering loss due to the mode mismatch between the waveguide and the cavity contributes to the grating loss.

In the following, without loss of generality, we will optimize the physical parameters with gratings formed by two segments (w_1 = 2 μm, w_2 = 3 μm) with Λ = 0.536 μm. The grating loss $\alpha_{grating}$ and cavity loss α_{cavity} was measured to be 2.0 dB/cm and 0.3 dB/cm respectively. Based on $L_{grating}$, $\alpha_{grating}$, Equation (7.22) and (7.23) were used to calculate the reflectivity r and transmittivity t. Then, with the known L_{cavity} and α_{cavity}, the FWM conversion efficiency was calculated by Equation (9.18),

9.3.2 Optimization via the Model

Let us take a close look to Equation (9.18)

$$\eta = \left|\gamma P_p L'\right|^2 FE_p^4 FE_s^2 FE_c^2$$

where

$$\gamma = \frac{n_2 \omega_c}{A_{eff} c}$$

$$L'^2 = L^2\, exp(-\alpha L)\left|\frac{1 - exp(-\alpha L + i\Delta kL)}{\alpha L - i\Delta kL}\right|^2$$

$$FE_i^2 = \left|\frac{t_1}{1 - r_1 r_2\, exp(-\alpha L - i2k_i L)}\right|^2 (1 + \left|r_2 e^{-\alpha L/2}\right|^2)$$

The nonlinear coefficient γ is just related to the Kerr coefficient n_2, effective mode size A_{eff} and the converted frequency ω_c, which are properties of the material and waveguide design. The possible improvement in this term is via changing the waveguide design, to increase the confinement factor. Since the Kerr coefficient of silicon nitride is 10 times better than that of silicon dioxide, better confinement means larger nonlinear coefficient. We will show some simulation results about this in the section 9.5.

With fixed pump power, the left part, $\left|L'\right|^2 FE_p^4 FE_s^2 FE_c^2$, is the value that can be optimized by careful engineering. The loss α in the formula corresponds to α_{cavity} and L corresponds to L_{cavity}. So, in fact, L' and FE are only related to $L_{grating}$, $\alpha_{grating}$, L_{cavity}, α_{cavity} in our model. Meanwhile, the losses $\alpha_{grating}$ and α_{cavity} can be assumed to be a fixed value using the same grating and waveguide design, which means that to optimize the FWM conversion efficiency, we need to find the best set of $L_{grating}$ and L_{cavity}.

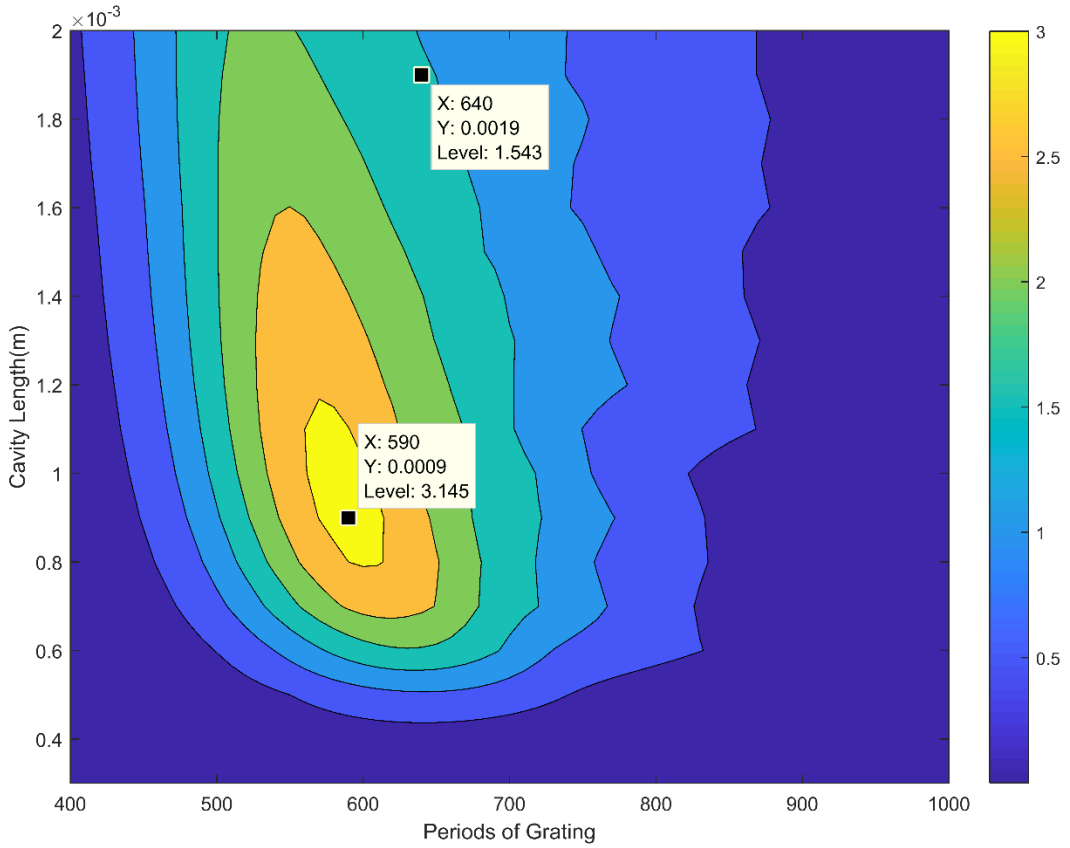

Figure 9.5 Calculated $\left|L'\right|^2 FE_p^4 FE_s^2 FE_c^2$ as a function of cavity length and number of grating periods with $\alpha_{grating} = 2\ dB/cm$, $\alpha_{cavity} = 0.3\ dB/cm$.

Figure 9.5 shows the simulated result based on the loss value we got experimentally. The grating loss is 2 dB/cm, and the cavity loss is 0.3 dB/cm. The X axis is the number of periods of grating on each side. The Y axis is the cavity length. The point located at x = 640, y = 0.0019, has a value of 1.543 m^2 . As we can see, we could improve the result by 2 times, if changing the number of periods to 590 and cavity length to 0.0009 m.

Theoretically, the device could have the same grating loss and cavity loss, which can be achieved by using an adiabatic taper grating to avoid the mode mismatch at the

grating-cavity interface. When the grating loss is changed to 0.3 dB/cm, and the cavity loss is kept at 0.3 dB/cm, the calculated $\left|L'\right|^2 FE_p^4 FE_s^2 FE_c^2$ is plotted in Figure 9.6. Apparently, overall improvement occurs as expected. The optimal value increases to $26.53\ m^2$.

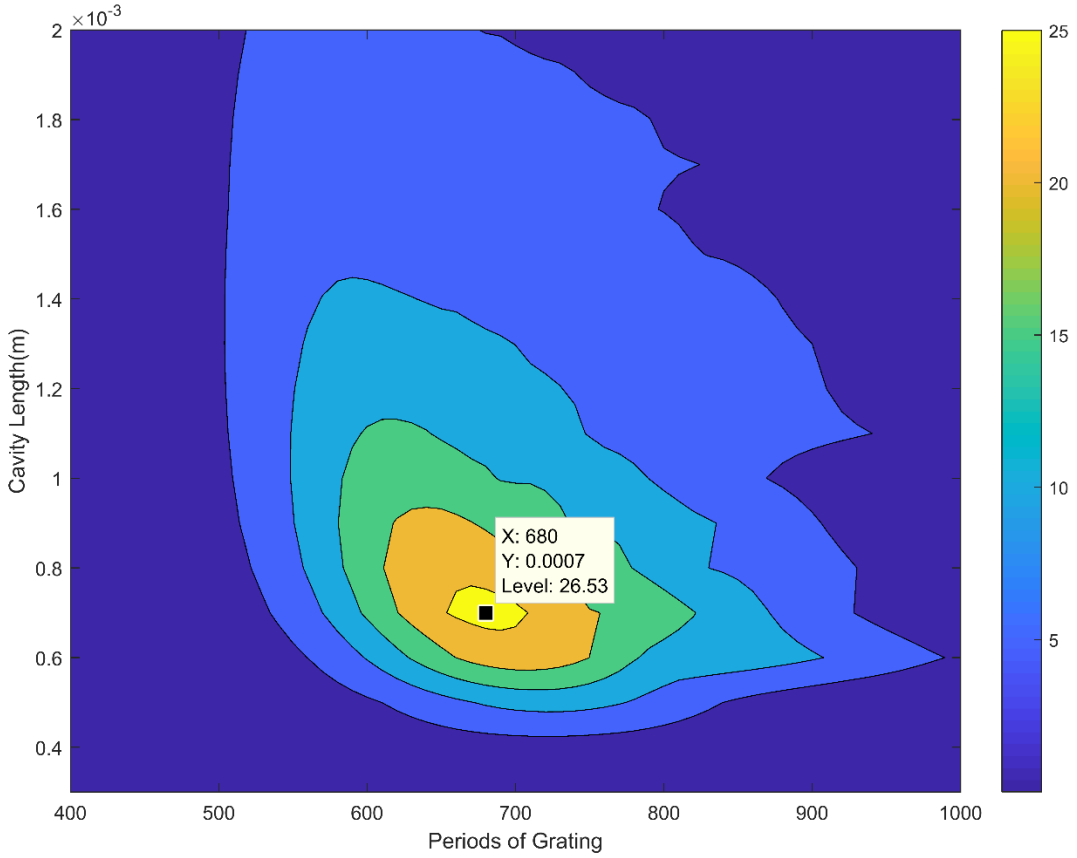

Figure 9.6 Calculated $\left|L'\right|^2 FE_p^4 FE_s^2 FE_c^2$ as a function of cavity length and number of grating periods with $\alpha_{grating} = 0.3\ dB/cm$, $\alpha_{cavity} = 0.3\ dB/cm$.

To further explore the potential of the enhancement, a few more optimization calculation has been done with different values of grating and cavity losses. Using the same silicon nitride waveguide design that has a core cross section with a height of

100 nm and a width of 2 μm, the smallest loss that has been demonstrated experimentally in our lab is around 0.1 dB/cm. Based on this value, calculated $\left|L'\right|^2 FE_p^4 FE_s^2 FE_c^2$ values are shown in Figure 9.7.

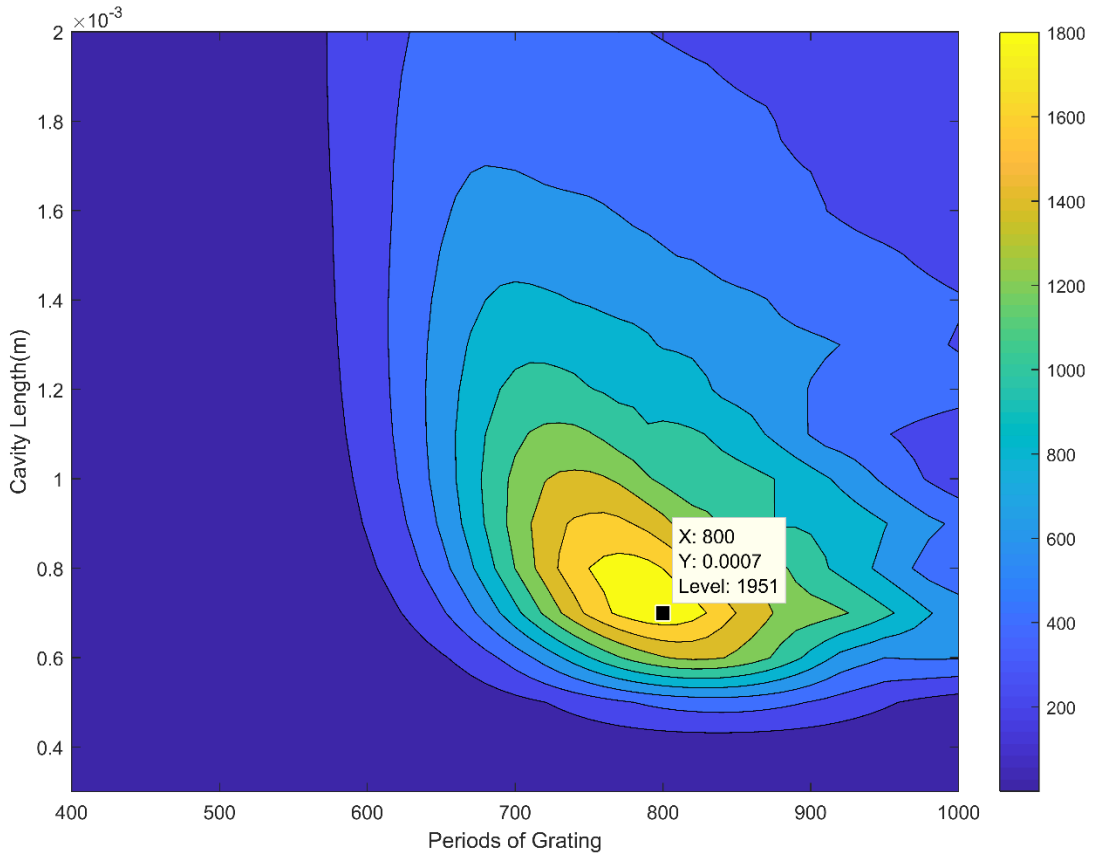

Figure 9.7 Calculated $\left|L'\right|^2 FE_p^4 FE_s^2 FE_c^2$ as a function of cavity length and number of grating periods with $\alpha_{grating} = 0.1\ dB/cm$, $\alpha_{cavity} = 0.1\ dB/cm$.

The maximum $|L|^2 IE_P^2 IE_s IE_c$ is $1591\ m^2$. Compared to the original experimental data, it sees a 30 dB improvement.

9.4 Observation of Four-Wave Mixing

The FWM conversion efficiency is measured by using the setup sketched in Figure 9.8. Two tunable CW lasers are used to generate the pump and signal, where both waves are controlled in polarization independently. The wavelength of both tunable lasers are tuned to match one of the resonator cavity's longitudinal modes. After the polarization controllers (PC), the polarization states of both waves are aligned to TE. After combing pump and signal in the 3-dB coupler both waves are launched into the silicon nitride waveguides. The spectra of the FWM are measured by using an optical spectrum analyzer (OSA) at the output of the waveguide.

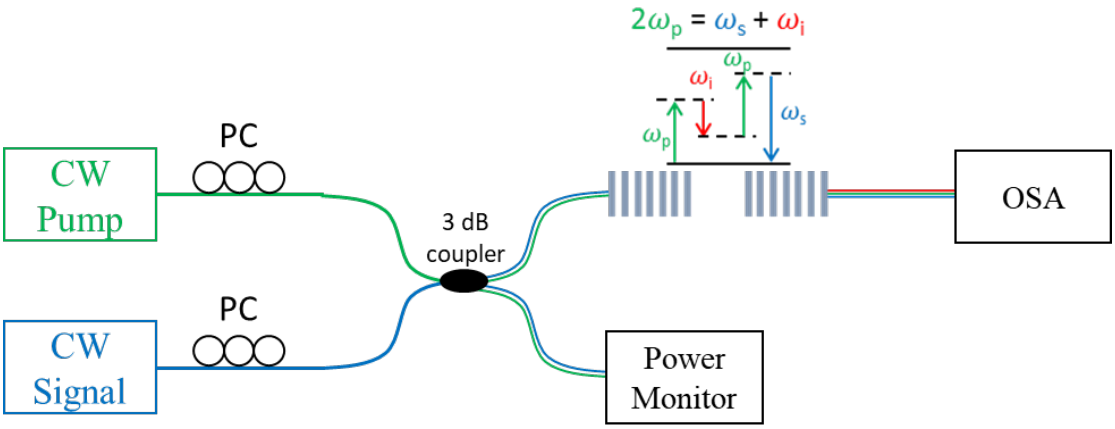

Figure 9.8 Schematic of measurement setup for Four-Wave Mixing experiments (CW = continuous wave; PC = polarization controller; OSA = optical spectrum analyzer).

In the experiments, pump and signal waves were placed with about 0.83 nm wavelength separation (pump 1590.1 nm, signal 1589.2 nm) to minimize the impact of dispersion in the FWM process. In fact, according to the transmission spectrum of the Fabry-Perot device (Figure 9.9), the spacing between the resonance peaks of the

pump and signal waves is 837.2010 pm, while the spacing between the peaks of the pump and converted signal is 837.0525 pm. The difference is negligible.

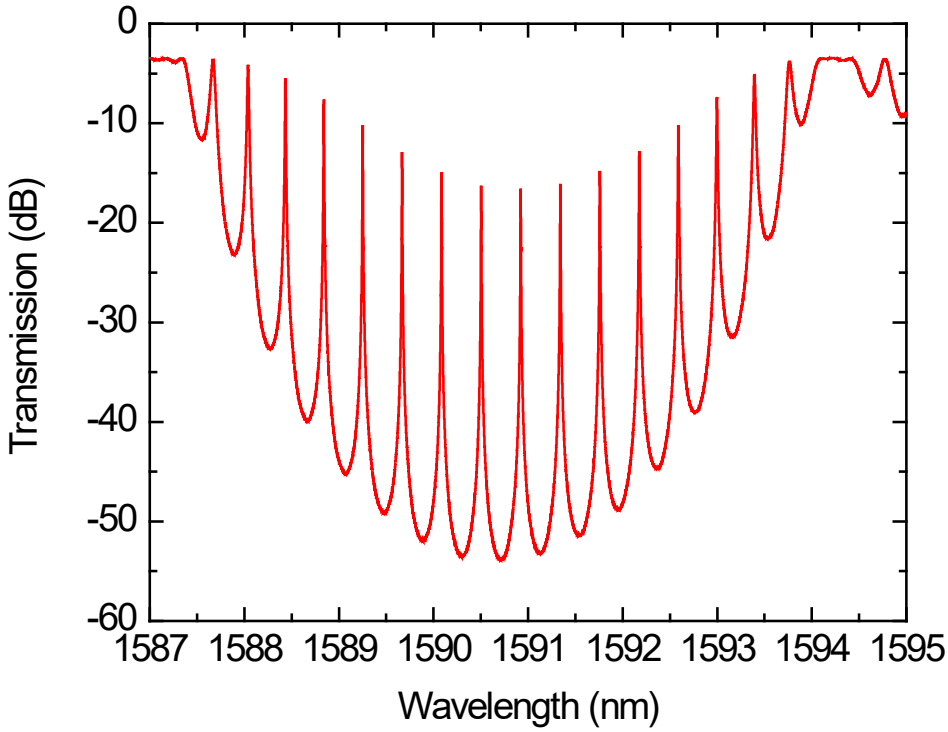

Figure 9.9 Transmission spectrum of Fabry-Perot enhanced FWM device.

The pump power and the signal power were kept at 13 dBm and 3 dBm respectively. At the output the converted wave was tracked with an OSA, as shown in Figure 9.10. The FWM conversion efficiency, defined as P_c^{out}/P_s^{out}, is measured to be -50 dB.

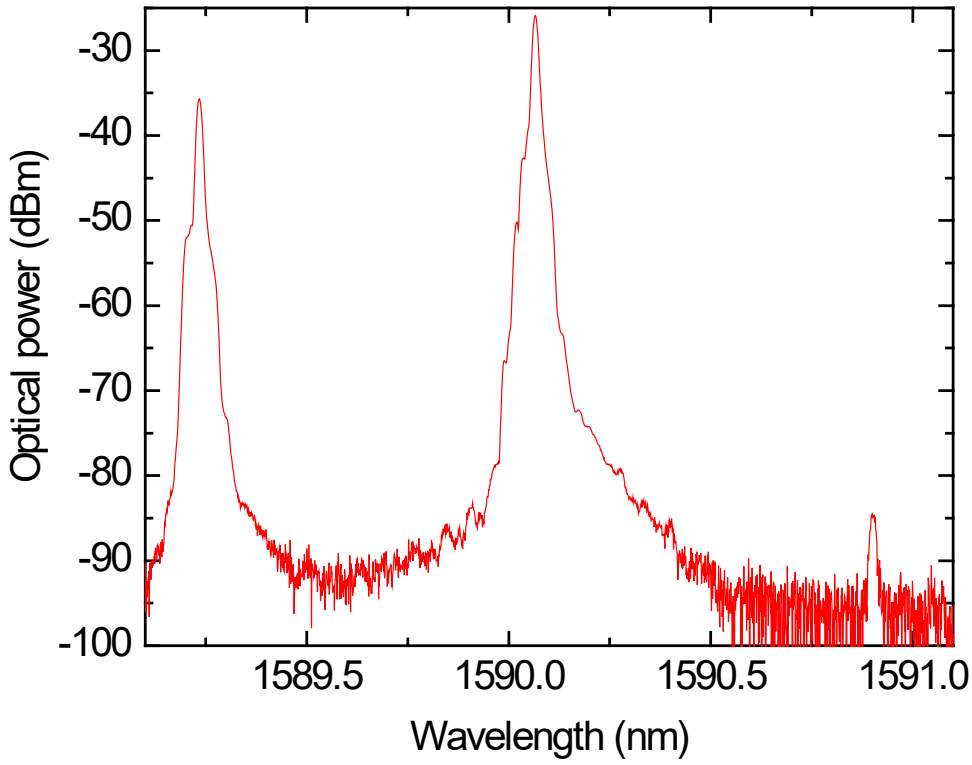

Figure 9.10 The output optical spectrum of Fabry-Perot enhanced FWM device.

We used the model developed in the previous section to theoretically calculate the conversion efficiency. It is necessary to consider the Kerr coefficient of both silicon nitride and silicon dioxide, since the confinement factor of the waveguide in this case is only 0.104. Most of the power is distributed in the silicon dioxide cladding instead of the silicon nitride core. So, the nonlinear coefficient γ is calculated by

$$\gamma = \frac{n_2^{SiN}\omega_c}{A_{eff}^{SiN}c} \cdot F + \frac{n_2^{SiO}\omega_c}{A_{eff}^{SiO}c} \cdot (1 - F) \tag{9.19}$$

where $A_{eff}^{SiN} \approx 0.2\,\mu m^2$, $A_{eff}^{SiO} \approx 3.64\,\mu m^2$, $F = 0.104$, $n_2^{SiN} = 2.5 \times 10^{-19}\,m^2W^{-1}$,$n_2^{SiO} = 2.6 \times 10^{-20}\,m^2W^{-1}$, which gave us $\gamma \approx 0.5429\,(W \cdot m)^{-1}$.

Also, we have $P_p \approx 6\ dBm$, $L' \approx 1.93\ mm$. The value of the pump power is a result of considering the losses due to a 3-dB coupler, fiber-to-waveguide coupling and several FC\APC connectors. Thus, we got $\left|\gamma P_p L'\right|^2 \approx -107.6\ \mathrm{dB}$. The calculated intensity enhancement factor, which equals to FE^2, as a function of wavelength was calculated and plotted in Figure 9.11. Then, we got $FE_p^4 FE_s^2 FE_c^2 = 34^2 \times 34 \times 34 \approx 61.3\ dB$. Finally, considering the 3 dB loss due to the symmetric structure, the calculated FWM conversion efficiency was -49.3 dB, which agrees with the measured conversion efficiency -50 dB. This indicates that over 61 dB enhancement was achieved compared to a single straight waveguide with similar length as the cavity.

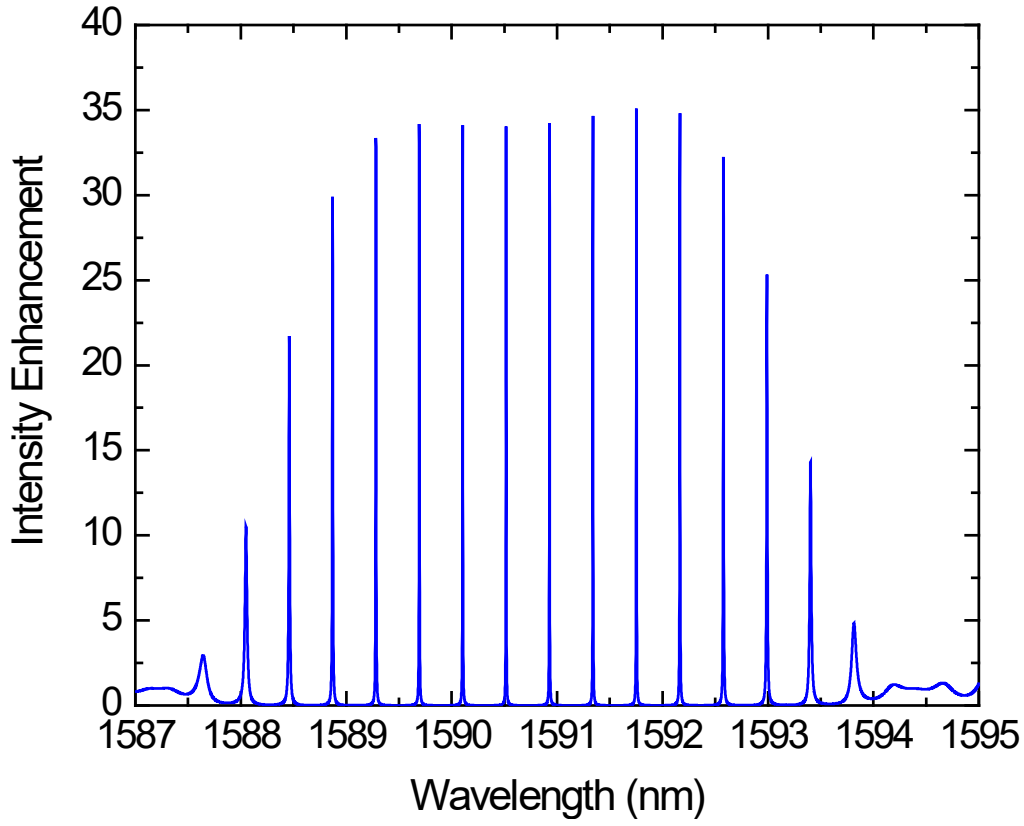

Figure 9.11 The field enhancement factor as a function of wavelength.

9.5 Potential Improvement

As mentioned in section 9.3, if the confinement factor of the waveguide can be further improved, both the nonlinear coefficient γ and the FWM conversion efficiency η will be increase. Here, we will show some simulated data of different waveguide structure. The nonlinear coefficient is calculated by Equation (9.19),

$$\gamma = \frac{n_2^{SiN}\omega_c}{A_{eff}^{SiN}c} \cdot F + \frac{n_2^{SiO}\omega_c}{A_{eff}^{SiO}c} \cdot (1 - F)$$

As we can see, the potential improvement of the nonlinear coefficient is from 3 to 4.8 dB, corresponding to an improvement of the FWM conversion efficiency from 6 to 9.6 dB.

Table 9.1 Calculated nonlinear coefficient for different waveguide structure.

Core thickness /nm	Core width / μm	Confinement Factor	A_{eff}^{SiN} / μm^2	A_{eff}^{SiO} / μm^2	γ $/(W \cdot m)^{-1}$
100	2	0.1042	~0.2	~3.638	0.5429
300	1	0.4805	~0.3	~0.666	1.6713
	2	0.5654	~0.6	~0.591	1.0119
400	1	0.6304	~0.4	~0.437	1.6526
	2	0.7038	~0.8	~0.311	0.9721
500	1	0.7275	~0.5	~0.312	1.5353

Chapter 10 Optical Phased Array for Virtual Reality Applications

In recent years, we have seen unprecedented growth in the technology supporting virtual and augmented reality (VR and AR) environments. This growth stems from (a) advances in commodity lightweight sensors, (b) unprecedented computational power, enabled by multi-core processors in increasingly compact devices, and (c) increasing availability of consumer wearable virtual and augmented reality displays, such as the Oculus Rift, Meta Glasses, Samsung Gear VR, Sony Morpheus and Microsoft Hololens. The potential applications have just started to be explored for these new technologies, which promise to fundamentally transform both how we use information and interact with the world around us.

10.1 Introduction

The recent surge in the use of 3D displays and content has been unfortunately accompanied by a rise in psychophysical problems associated with their viewing. Popular press has reported a number of viewers complaining about 3D movies causing headaches, nausea, blurred vision, and other symptoms of visually-induced motion sickness. Studies have identified the vergence-accommodation conflict to be the cause of many psychophysical problems [101] including discomfort [102], induced binocular stress [103,104], difficulty in fusing two images into a stereo pair [104], and misperception of scene geometry [105,106]. Figure 10.1 shows the difference between natural viewing and stereo viewing. In natural viewing, the viewer adjusts the vergence of the eyes to look at an object and thereby perceive a single

focused image rather than two. The viewer's eyes also focus in order to perceive a sharp rather than blurred image. Vergence and accommodative distance are equal to one another. In stereo viewing, virtual display plane, or focal plane, is located at a fixed distance. The virtual objects can be located either in front or, if it is not at infinity, behind it. Accommodative distance is fixed at the distance from the eyes to the display plane, while vergence distance varies depending on the distance being simulated on the display. To see the object singly and clearly, the viewer must counteract the neural coupling between vergence and accommodation to accommodate to a different distance than the distance to which he/she must converge. Unfortunately, the decoupling of vergence distance from the focal plane at the display screen (also known as the vergence-accommodation mismatch) is inherent for all VR and AR displays in the market today. We will develop natural-to-senses VR and AR 3D displays that will directly address the vergence-accommodation mismatch.

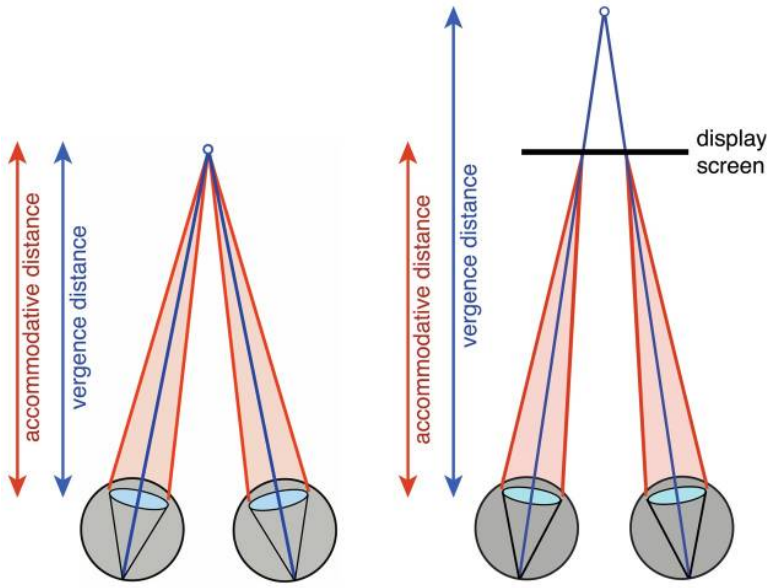

Figure 10.1 Diagram of natural and stereo viewing [107]

In a pinhole camera, all the light rays enter the camera through a single point and the entire image is in sharp focus. In contrast, human eyes have varying aperture (adjustable pupil size) and a variable focus (adjustable curvature of the flexible eye lens). As a result, instead of a cone of light rays that meets at a point (as in a pinhole camera), a bundle of light rays passes through the pupil and the lens before impinging on the retina and creating an image of the external world. This spatio-angular distribution of light rays (and its generalizations) is referred to as the light field [108–110]. To create a true natural-to-senses display, we need to reproduce the entire light field entering the pupil of each eye. While optical phased arrays can be used to generate arbitrary radiation patterns, having them render images in the visible spectrum is non-trivial, as they require prohibitively high power for reasonable-resolution displays, and are unable to render changes to the light field display at interactive rates under computer control. Here, we take advantages of the design of optical phased arrays to address these challenges and sufficiently advance 3D graphics rendering to allow us to build an optical array-enabled multifocal display on a chip. Such a pair of chips can be mounted on a head-mounted display with appropriate optics to render a multifocal stereo 3D rendering. It would permit construction of electrically addressable holographic circuits. For instance, we could drive the phased-array with 3 different signals recorded with 3 different cameras looking at the same scene but using different focus. One can imagine walking in a city wearing a pair of holographic goggles and focusing on a particular building but not on the other buildings. One can also imagine targeted advertising with ads focused on, or a sign providing information on a particular building.

10.2 Optical Phased Array Design

To make optical phased array highly compact, low power consumption and scalable to visible light operation, we use silicon nitride core as a transparent waveguide for handling images, and use Complex Waveguide Bragg Grating (CWBG) to significantly reduce the size and power of the heating element for controlling the optical phase and amplitude.

The ability to generate arbitrary radiation patterns with large-scale phased arrays has long been a desirable goal. It would extend the functionality of phased arrays beyond conventional beam focusing and steering, communication and radar, and open up new opportunities in image processing, three-dimensional holography, and virtual reality. The far-field radiation field $E(\theta, \phi)$ of the phased array is the multiplication of the far field of an individual antenna element $S(\theta, \phi)$ and that of the array factor $F(\theta, \phi)$,

$$E(\theta, \phi) = S(\theta, \phi) \times F(\theta, \phi) \tag{10.1}$$

where θ and ϕ are the far-field azimuth angle and polar angle respectively. While the far field of an individual antenna is fixed, the array factor $F(\theta, \phi)$ is a system factor that is related to the Fourier transform of the near-field optical emission w_{mn} of all the pixels (where m and n are the pixel indices) in the phased array.

$$F(\theta, \phi) = \sum_{m=1}^{M} \sum_{n=1}^{N} w_{mn} \cdot e^{j2\pi(x_m u + y_n v)} = F(w_{mn}) \tag{10.2}$$

where M × N is the size of the array, and (x_m, y_n) describes the position of each antenna. The emitting amplitude and phase of the antenna is described by $|w_{mn}|$ and φ_{mn} respectively, so that $w_{mn} = \left|w_{mn} \cdot e^{j\varphi_{mn}}\right|$. Most phased arrays use only the phase φ_{mn} of each pixel to control the far-field radiation while the amplitude $|w_{mn}|$

for each pixel in the near-field is uniformly distributed. The Gerchberg-Saxon algorithm [111,112] is particularly appropriate to generate a specific far-field radiation pattern by assigning the optical phase of each pixel in the phased array. We used the Gerchberg-Saxton algorithm as an efficient way to find the optical phase φ_{mn} to generate a given radiation pattern $F(\theta, \phi)$.

Moreover, to prevent high-order radiation lobes in the far-field, each phased-array element should be smaller than half the wavelength of light in free space. But in practice, large pixel size (~12 μm) is required to obtain phase shifts as large as 2π, because even by using materials with large thermo-optic coefficients, a phase shift of π is accumulated over ~20 μm by increasing the material temperature by a few hundred degrees. To significantly reduce the pixel size, traditional phase shifter that simply uses the thermo-optic coefficient of the material should be replaced, since it has a physical limitation of the required length. In this study, we design CWBG with desired complex transmission coefficient by two methods, that is Layer Peeling/Adding algorithm and genetic algorithm. Figure 10.2 shows a typical 1-layer structure of the CWBG. The CWBG, which is implemented as a single-mode silicon nitride core and silicon dioxide cladding (Si_3N_4/SiO_2) waveguide grating with aperiodic varying waveguide widths, is capable of using the thermo-optic effect to control the phase and intensity of the transmitted light, which enable the possibility to significantly reduce the pixel size.

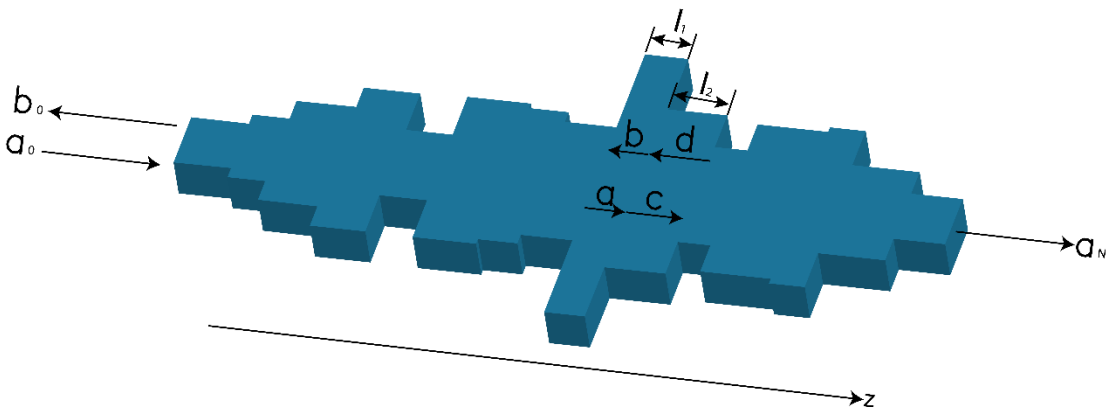

Figure 10.2 1-layer structure of CWBG on Si_3N_4/SiO_2 waveguide platform. The width of the CWBG varies in an aperiodic way.

Visible-light operation of an optical phased-array is a key milestone. However, the scaling up of the optical phased array to handle visible images is not trivial. The challenge is that silicon absorbs visible light, and is therefore not able to handle images in the visible part of the spectrum. Even though some previous results [113,114] in silicon are impressive and could be used for infrared applications, the amount of power required for a phase shift of π is as much as 8.5 mW. Since the area of each element is 10 μm x 10 μm, more than 8.5 kW/cm^2 of power would be required to be thermally dissipated. This is beyond the 4000 W/cm^2 that can be dissipated by spray cooling, a leading cooling technology. To make things worse, silicon nitride, a natural contender for making waveguides transparent in the visible, has a thermo-optic coefficient in the visible three times worse than silicon in the infrared. The thermo-optic coefficient of silicon is 1.8 x 10^{-4}/K at a wavelength of 1.55 μm and the thermo-optic coefficient of silicon nitride is 6.2 x 10^{-5}/K at 620 nm. The CWBG could successfully resolve this by reducing the power consumption to

achieve 2π phase shift. With carefully design, a complex transmission spectrum with linear phase change and constant amplitude within a very narrow wavelength range can be achieved. Thus, with only a small temperature increase of the CWBG, the phase of the output can change dramatically.

The final element required in each unit cell is the radiating element to free space. This element will allow constructive and destructive interference of the radiating electric field from all the unit cells. Using 3D-FDTD, the radiating element using a few period circular gratings was designed to diffract light from the waveguide to free space. By proper design of the grating, the up-down symmetry was broken and more light was diffracted toward the transparent substrate. When the optical chip is flip-chip bonded on the electronic chip, the light will finally be emitted toward free space.

10.2.1 Gerchberg-Saxton Algorithm

In this section, the implementation of Gerchberg-Saxton algorithm on the synthesis of optical phased array will be described.

If we only care about the amplitude distribution in the far field, we can get arbitrary pattern by using only one input parameter, the phase distribution φ_{mn} of the array. And we just keep the amplitude $|w_{mn}|$ evenly distributed throughout the phased array.

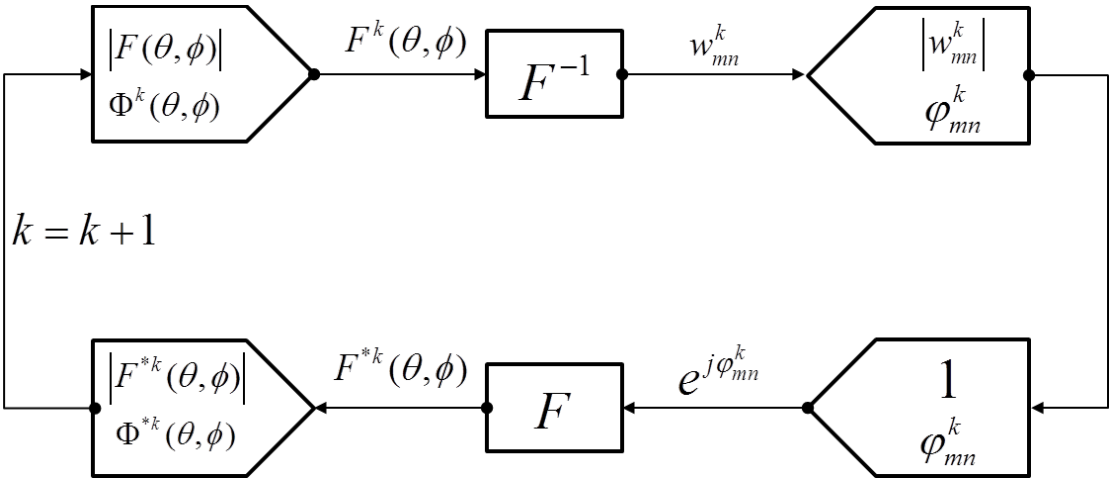

Figure 10.3 The block diagram of the Gerchberg-Saxton algorithm for phased array synthesis with uniform power distribution in near-field.

Figure 10.3 shows the iterative Gerchberg-Saxton algorithm to synthesize a far-field array factor of amplitude $|F(\theta,\phi)|$ with an evenly distributed power distribution within the phased array. The initial trial phase $\Phi^1(\theta,\phi)$ is set to 0 or any arbitrary values. At the k[th] iteration, the targeted amplitude $|F(\theta,\phi)|$ and a trial phase $\Phi^k(\theta,\phi)$ is inversely Fourier-transformed to find the corresponding near-field optical emission w_{mn}^k. Since we only care about the amplitude distribution of the far-field array factor, we can set the amplitude of the near-field emission to 1 while keep its phase φ_{mn}^k. Then the Fourier-transform is applied to the modified near-field emission distribution. After that, the resulting new far-field array factor $F^{*k}(\theta,\phi)$ is updated, and its phase $\Phi^{*k}(\theta,\phi)$ is passed to the $(k+1)^{th}$ iteration as the new trial phase $\Phi^{k+1}(\theta,\phi)$. After several iterations, the amplitude of $F^{*k}(\theta,\phi)$ generated by φ_{mn}^k converges to the designed pattern $|F(\theta,\phi)|$.

Through this algorithm, by controlling only the phase distribution in the near field, desired image can be produced in the far field. Figure 10.4 shows the simulated results of a 64 × 64 phased array to generate the UMD logo. As we can see, the near-field amplitude is evenly distributed, and the far-field phase is distributed arbitrarily.

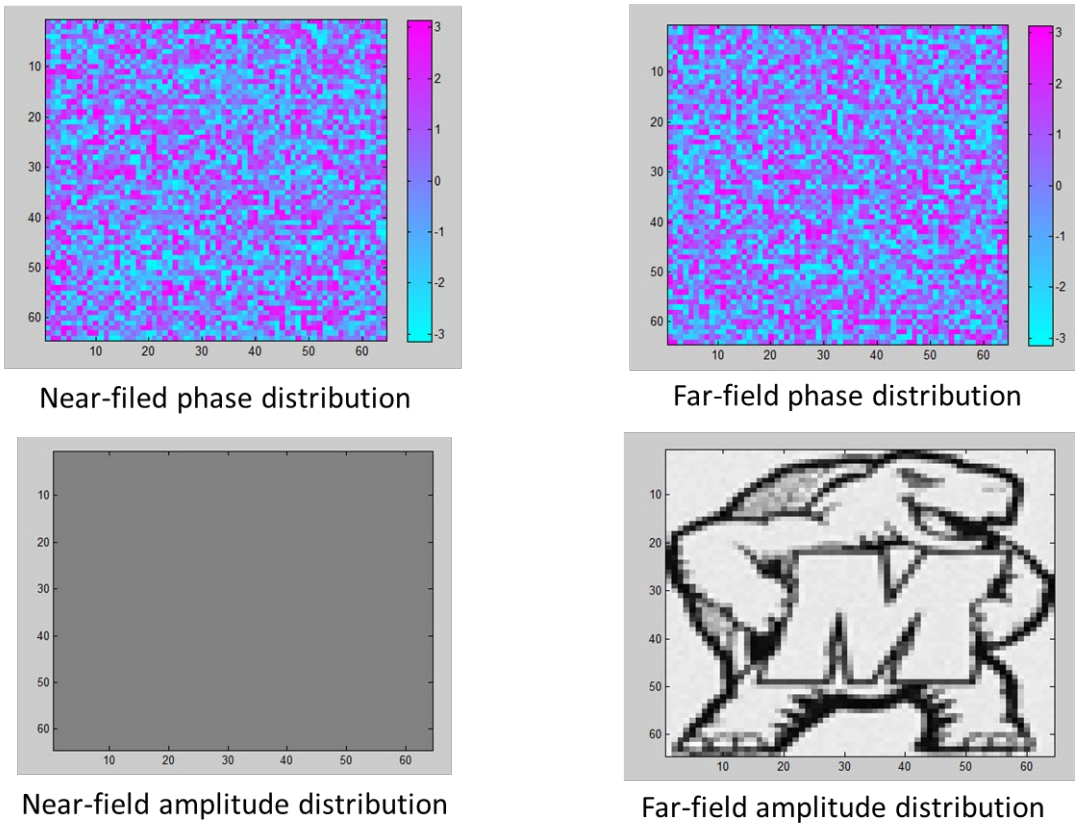

Figure 10.4 Simulated results of a 64 × 64 phased array to generate the UMD-logo.

We note that, if we want to apply a certain phase distribution in the far field, another input parameter is required to be controlled, which is the amplitude of each antenna element. In this case, no iteration is required in the algorithm; just one inverse Fourier-transform is needed. Figure 10.5 illustrates this simple algorithm. The

targeted amplitude $|F(\theta,\phi)|$ and phase $\Phi(\theta,\phi)$ is inversely Fourier-transformed to find the corresponding near-field optical emission w_{mn}^{k}.

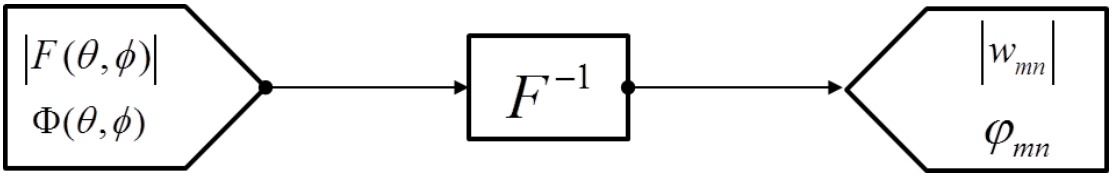

Figure 10.5 The block diagram for phased array synthesis with arbitrary amplitude and phase distribution in far-field pattern.

So both the amplitude and the phase distribution in the phased array matrix are controlled. Any designed image including its amplitude and phase information can be produced in the far field. Digital holography techniques can be used to design phased arrays that generate 3D holograms. This opens the possibility for 3D displays and TVs without requiring specialized glasses. Figure 10.6 shows the simulated results of a 64×64 phased array to generate the UMD-logo with circular phase front added to the image.

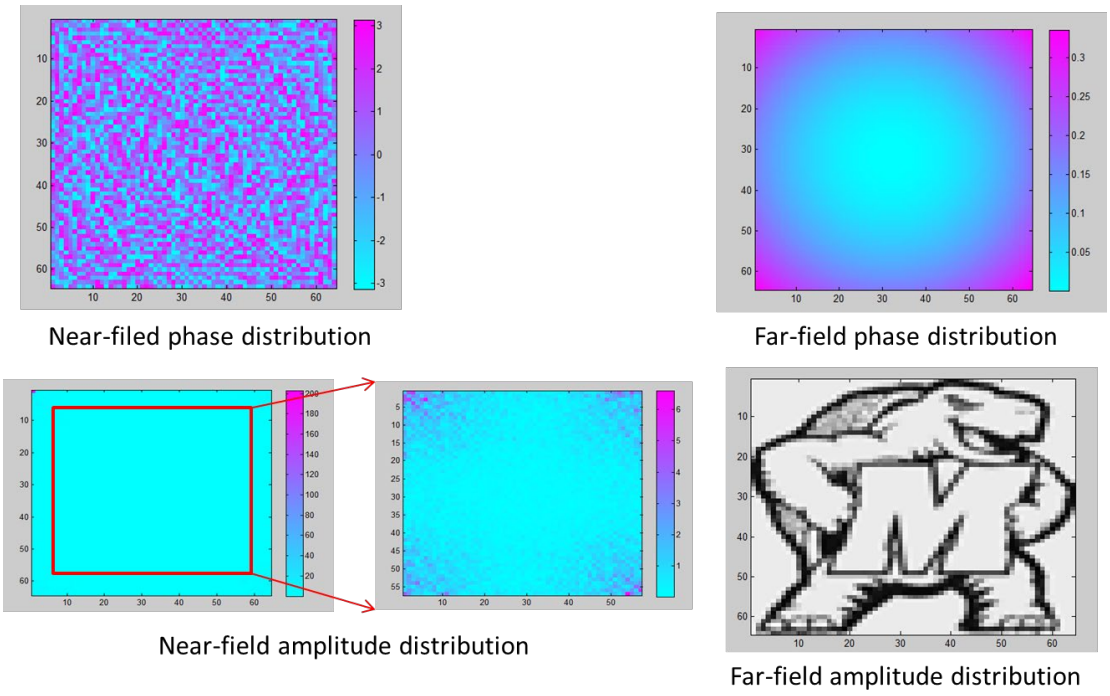

Figure 10.6 Simulated results of a 64 × 64 phased array to generate the UMD-logo with circular phase front added to the image.

10.2.2 Generation of CWBG with Specific Transmission Spectrum

When converting the phased array from an infrared to a visible wavelength image projection, even smaller pixel size is required. It becomes harder to use a simple waveguide tuned by the thermo-optic effect in the phased array as the phase shifter. Slow-light waveguide structures are required in order to impart a large optical phase shift over a short propagation distance. The slower the group velocity of the waveguide mode, the larger the optical phase shift that can be imparted over a fixed propagation distance. In this section, we will describe two methods to generate a CWBG with desired complex transmission spectrum to replace the simple waveguide as the phase shifter and attenuator, which is the Layer Peeling/Adding algorithm and the genetic algorithm. The goal of the synthesis is to find a CWBG that provides

significant slowdown of the light, while still having a relatively high transmission within a certain bandwidth. So that, the optical phase or amplitude of each pixel can be continuously tuned by the thermo-optic effect through an integrated heater with less power consumption.

Although the CWBG still relies on the thermo-optic effect, the underlying fundamental is totally different from just changing the optical path to produce a phase shift. Instead, in our approach the whole transmission spectrum is shifted by the thermo-optic effect to realize the required phase shift. Potentially, this will reduce the size of each pixel and also will reduce the power needed for a 2π phase shift.

10.2.2.1 Layer Peeling/Adding Algorithm

One thing needs to keep in mind is that it is much harder to realize a given complex filter function in transmission than in reflection. The fact that the transmission coefficient will satisfy the minimum-phase condition reduces the flexibility [115–117]. This leads to a unique relation between the amplitude and the phase responses in transmission, which strongly limits the possibilities. Also, no matter what the reflection phase response is, a Bragg grating with a given reflection amplitude response will correspond to the same complex transmission coefficient. This causes the result of the synthesis problem not to be unique.

Since there is a unique relation between the amplitude and the phase responses in transmission, it is generally impossible to realize an arbitrary complex transmission coefficient for all frequencies. We must limit the desired complex transmission spectrum to a finite bandwidth $\Omega = (\omega_1, \omega_2)$, and leave the response for $\omega \notin \Omega$

unspecified. By doing that, we can obtain a transfer function H(ω) that approximates the desired complex spectrum in Ω and also satisfies the required minimum-phase condition owing to its behavior outside Ω.

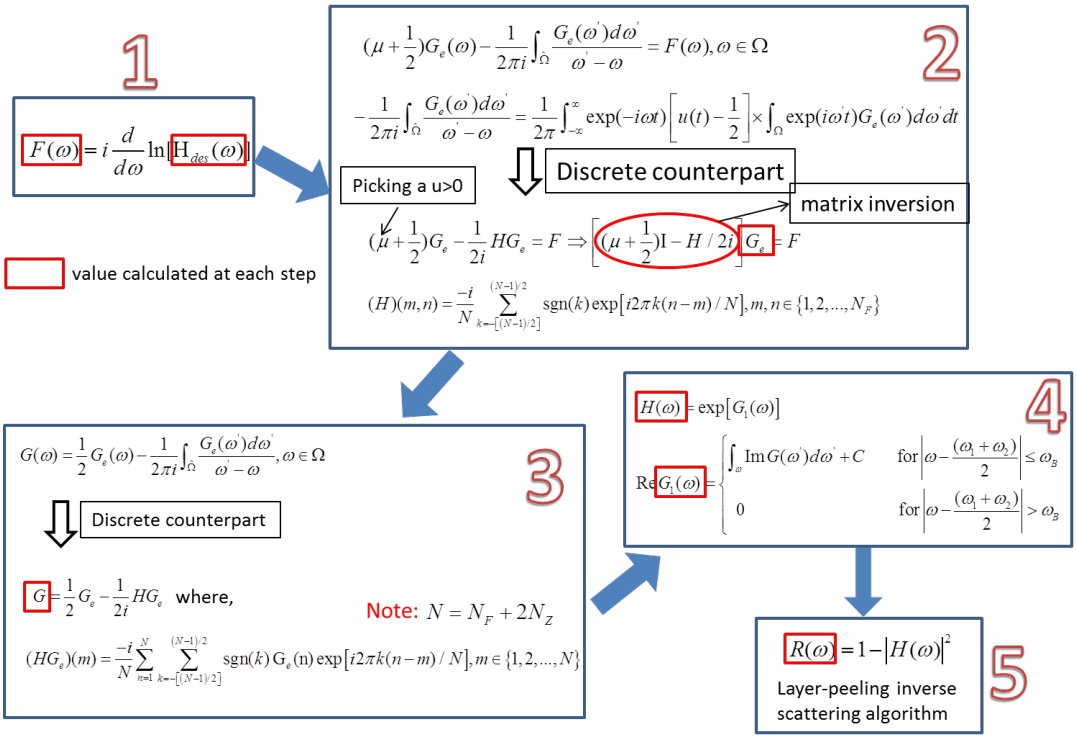

Figure 10.7 The flow of the synthesis algorithm of CWBG with a desired complex transmission spectrum.

Figure 10.7 shows the algorithm flow to synthesize CWBG with a desired complex transmission spectrum. There are 5 steps in this algorithm.

Step 1: Modified from the desired complex transmission spectrum $H_{des}(\omega)$, we get a new function F(ω). This helps to guarantee that |H(ω)| ≤ 1.

Step 2: Solve the Krein-Nudel'man problem numerically using the input function $F(\omega)$. The solution $G_e(\omega)$ has the same dimension of $F(\omega)$.

Step 3: Expand the frequency range of $G_e(\omega)$ by padding zeros outside Ω on both sides. Calculate $G(\omega)$ by a Hilbert transform of $G_e(\omega)$.

Step 4: Determine the transmission Coefficient $|H|$.

Step 5: Synthesize a CWBG with reflectivity $R(\omega) = 1 - |H(\omega)|^2$ and arbitrary phase response. This is done by the use of a Layer Peeling/Adding (LP/LA) inverse scattering algorithm [81,82].

The output of the LP/LA algorithm gives the coupling coefficient (also sometimes called the grating profile) of the grating directly, but that does not say anything about the detailed structure of the grating. To realize a physical grating, we need to obtain the profile of the effective index of refraction along the propagation direction. From the LP/LA algorithm, the grating profile is obtained initially, which can be related to the effective index variation along the grating. This range of the effective index variation is then mapped to a 1-layer waveguide structure with varying widths. It means that one specific waveguide width will correspond to one specific effective index.

Figure 10.8 shows the theoretically expected change of the effective index as the width of the Si_3N_4/SiO_2 waveguide varies, when the thickness of the waveguide is 50 nm, 100 nm, 200 nm and 300 nm respectively. When choosing the thickness of the waveguide, the resolution of the e-beam lithography system and the scattering losses of the waveguide should be balanced. Suppose that a range of 0.004 of effective index

is required. If the thickness of Si_3N_4/SiO_2 waveguide is 200 nm or 300 nm, in order to get an effective index change of 0.004, the width can only vary by ~50nm and ~20 nm, respectively. Simply dividing this number by 20, it gives a width step of 2.5 nm and 1 nm, respectively. It is impossible to write such small steps of the waveguide widths, even with the state-of-the-art lithography technology. On the other hand, if a Si_3N_4/SiO_2 waveguide thickness of 50 nm is used to fabricate the CWBG, then as can be seen in Figure 10.8 (a), the change of the effective index is only about 0.002 even when the width varies from 0.4 to 2 μm. Consequently, large scattering losses will occur if the thickness of the CWBG is only 50 nm.

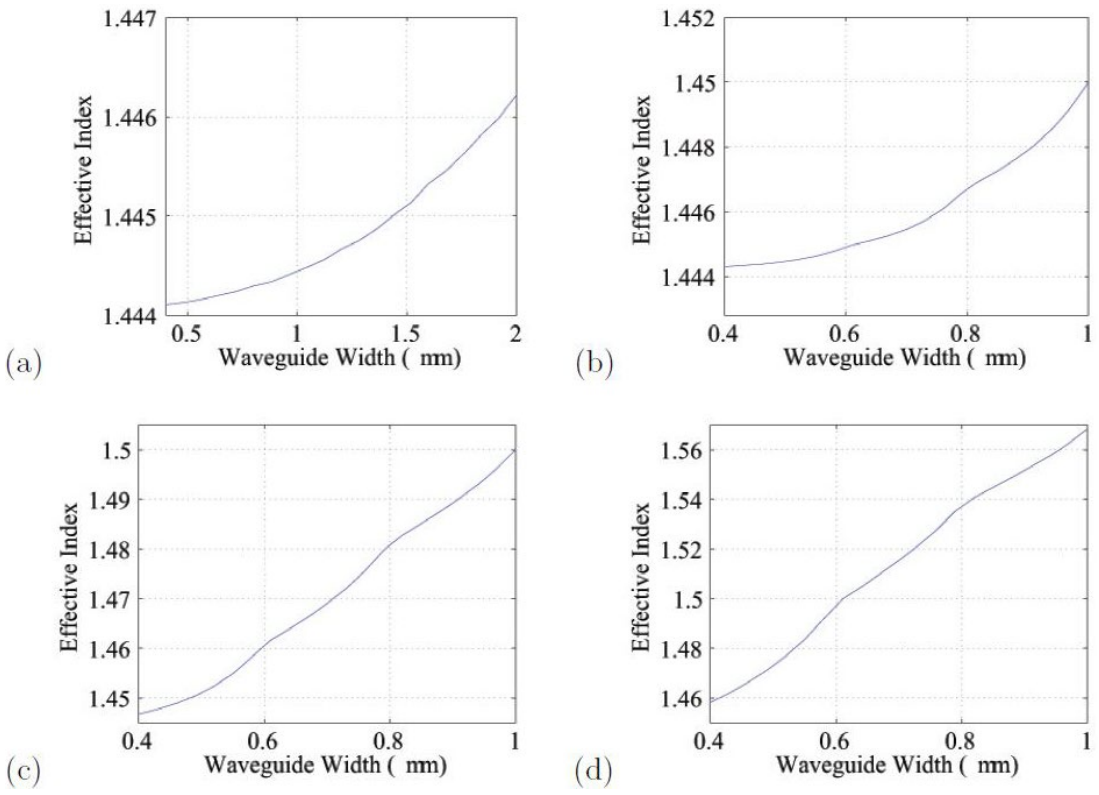

Figure 10.8 Theoretically expected effective index of the Si_3N_4/SiO_2 waveguide as the width and the thickness of the waveguide core vary. (a) core thickness 50nm. (b) core thickness is 100nm. (c) core thickness is 200nm. (d) core thickness is 300nm.

When working as a phase shifter, at a certain wavelength, the CWBG should provide different phase responses at different temperatures, while the amplitude response should remain the same. Similarly, when working as an attenuator directly, it should provide different amplitude responses at different temperatures, while the phase response should remain the same. Since we understand that the complex spectrum is shifted when applying the thermo-optic effect, for a phase shifter within a certain bandwidth, the amplitude response should be a constant value and the phase response should be a continuous function with value between 0 to 2π. And similarly, for the attenuator within a certain bandwidth, the amplitude response should be a continuous function with value between 0 to 1 and the phase response should be a constant value.

Apparently, if we can get a linear response as a continuous function for either the amplitude or the phase response, it will simplify other parts of the phased array system. The simulation results for two different applications are shown in the following.

Figure 10.9 shows the power transmission and phase response of the CWBG with a desired constant amplitude response and a linear phase response. The central part within the two lines is the desired spectrum, while the outside is generated by the algorithm to satisfy the minimum-phase condition. The bandwidth of Ω is 0.9 nm and centered at 630 nm. This complex spectrum performs like what we expected. Within the 0.9 nm bandwidth, the power transmission is kept constant at about 90%. And the phase response decreases linearly from 2 to -2 as the wavelength is varied from 629.55 nm to 630.45 nm. However, further improvement is required by increasing the tuning range of the phase response while maintaining the high power transmission.

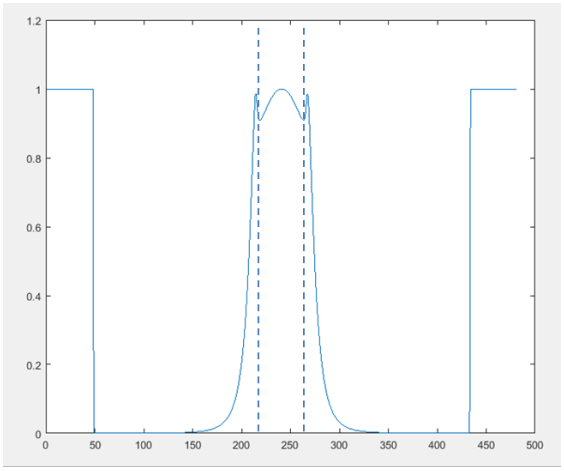

Figure 10.9 Power transmission and phase shift result of the CWBG with desired constant amplitude and linear phase response.

Figure 10.10 shows the power transmission and the phase response of the CWBG with the desired linear amplitude and constant phase response. This complex spectrum performs also like what we expected within the central part, while the outside is generated by the algorithm to satisfy the minimum-phase condition. The

bandwidth of Ω is 0.9 nm and centered at 630 nm. To further improve the grating performance, the tuning range of the amplitude response must be increased.

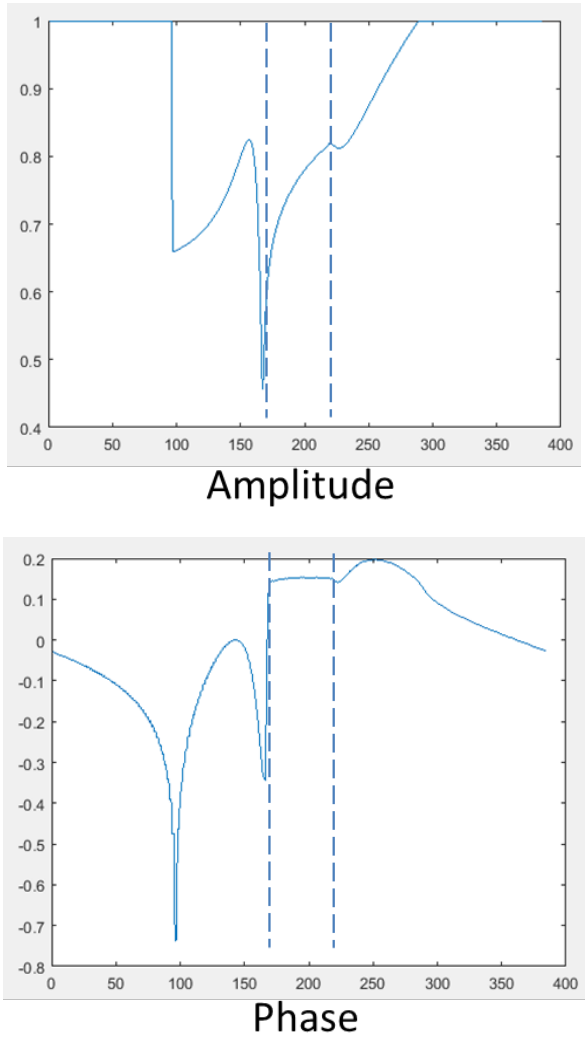

Figure 10.10 Power transmission and phase shift result of the CWBG with desired linear amplitude and constant phase response.

After putting substantial effort in the parameter searching, we found out that the outputs of the LP/LA algorithm has a common problem. That is, the requirement of

the total length of the grating is beyond our acceptable range. The shortest length is around 50 μm, while the grating can still satisfy the design goal. To overcome this problem, more parameters of the CWBG should be controlled independently. We will develop an optimization method using genetic algorithm, combing with the ABCD matrix method described in section 7.3, to generate the desired CWBG.

10.2.2.2 Genetic Algorithm

Genetic algorithm (GA) is a search method for solving both constrained and unconstrained optimization problems that follows the same principle as the evolution process of nature, see Figure 10.11.

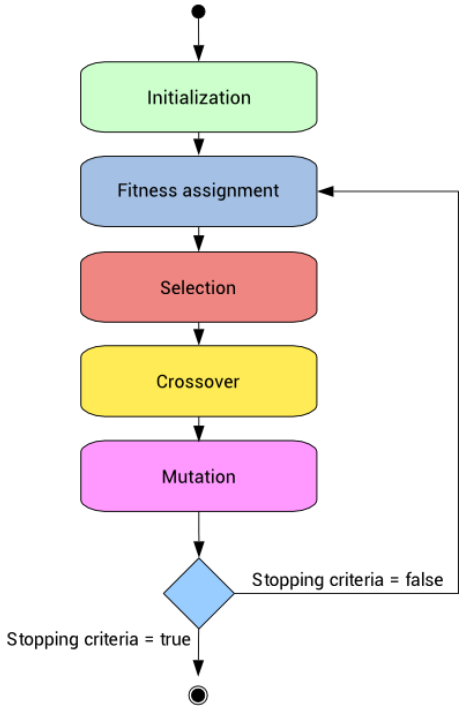

Figure 10.11 Flow chart of genetic algorithm.

GA is commonly used to generate high-quality solutions to optimization and search problems by relying on bio-inspired operators such as mutation, crossover and selection. The basic principles of GA were first laid down by Holland [118], and are well described in [119]. In our genetic algorithm, the evolution starts from a population of "individuals" that is randomly generated. Each individual represents a possible solution to the optimization problem. By calculating the value of the objective function, they are ranked after its fitness. Each candidate solution has a set of properties that can be mutated and altered. A new generation is made from the current generation by creating offspring from a pair of individuals. The more fit individuals are stochastically selected from the current population to reproduce. The two most common genetic operators are crossover and mutation. The new generation of candidate solutions is then used in the next iteration of the algorithm. By favoring the mating of the more fit individuals, we explore the more promising areas of the search space. Commonly, the algorithm terminates when either a maximum number of generations has been produced, or a satisfactory fitness level has been reached for the population. To maintain both the efficiency and the diversity of the algorithm, it requires careful selection of the parameters in initialization, selection, reproduction and termination.

Figure 10.12 Waveguide cross section illustration.

We are interested in optimizing the design of the CWBG to support slow-light modes over certain bandwidth by maximizing the n_g-transmission product. In this case, GA is used to design a phase shifter of 2π range within a relative short length, by maximizing the slow light effect. First, we obtain the effective refractive index at different width, by doing simulation in FIMMWAVE. The CWBG to be optimized here is based on silicon nitride core waveguide with a height of 300 nm, with silicon dioxide cladding on bottom and air cladding on top, see Figure 10.12. At 630 nm wavelength, the refractive index ranges from 1.495 with a width of 0.22 μm to 1.855 with a width of 0.7 μm. Based on these two values, we calculate the period of the periodic Bragg grating, which is 105 nm and 85 nm separately (just using lambda/4n). Then we consider the average length of each segment to be around 100 nm. So there will be 100 segments for a grating with length of 10 um. So, the number of inputs to the GA would be 200, since each segment has two parameters, one is the length, one is the width. For the width parameters, we will set upper and lower bound to 0.7 μm and 0.22 μm separately. And for the length parameters, we usually give the program more space to optimize. We will keep the segment length between 70 nm and 130 nm. Since the average length is still 100 nm, based on the GA output, optimized result

usually has a totally length around 10 μm. The width and length distributions of CWBG are the input parameters.

Then the performance of CWBG, i.e. Fitness assignment, was calculated by the ABCD matrix method. The output parameters of the GA can be chosen depending on different requirement. In the phased array application, we will optimize the average slow down factor between 626 nm and 630 nm wavelength. This wavelength range is determined by calculating the spectrum shift for 2π phase change. So, since the bandwidth is fixed, by optimizing the average slow down factor, we are optimizing the product of bandwidth and slowdown. Meanwhile, we also added the power transmission as another output of GA. Equation (7.28) and (7.30) were used to extract the slow down factor and the transmitted power of the CWBG.

Finally, a pareto front was plotted in real time. Figure 10.13 shows two pareto front plots, (a) shows optimized results of a 5-μm long CWBG, (b) shows optimized results of a 10-μm long CWBG. The trade-off between higher slow down and higher power transmission was observed. Longer CWBG tends to provide better slow down and higher transmission compared to shorter ones. For example, a 10-μm long CWBG with a slow down factor of 6 still has an average transmission of 70% within the bandwidth between 626 nm and 630 nm. Using this CWBG, to achieve π phase shit, it requires a temperature increase of about $\Delta T = 175℃$. The size of the unit cell in the phased array prevents us to have longer CWBG. But better performance is possible with less restrictions on width and length distribution of each segment.

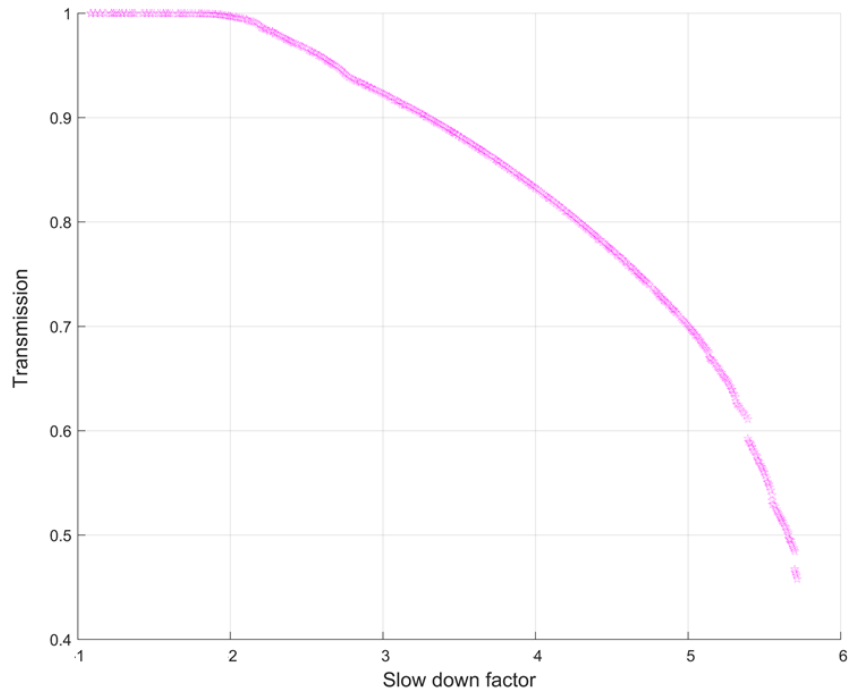

(a)

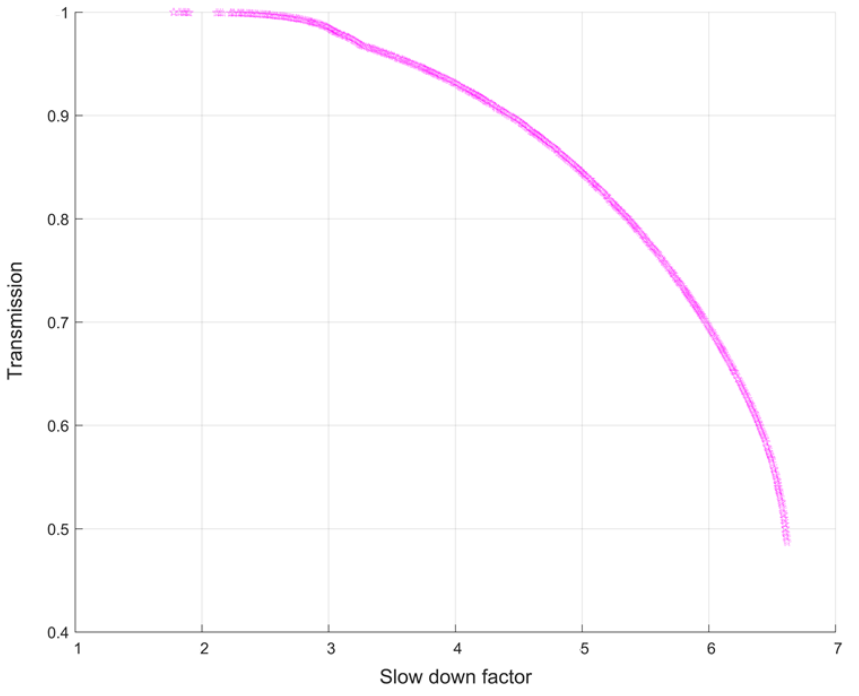

(b)

Figure 10.13 Pareto front plots: (a) optimized results of a 5-μm long CWBG; (b) optimized results of a 10-μm long CWBG.

Most part of the GA is compute-intensive and could be done in parallel. It will take advantage of the powerful GPU-accelerated computing. With the help of GPU, GA can be extended to longer gratings like a few hundred microns, even a few millimeters. It is able to synthesize more complicated structure and realize better performance. For example, if a desired optical transmission spectrum within a certain wavelength range is required, we can evaluate the individuals of the GA by defining an error function, which computes the difference between the calculated spectrum and desired spectrum, and then output a numerical value. Then, we let the GA to do the rest, to minimize this error value.

10.2.3 Nanoantenna

A compact and efficient optical nanoantenna is going to be optimized by using 3D-FDTD to diffract the guided light in the silicon nitride waveguide to the surrounding medium in which free-propagating light interferes in the far field. Preferably, the nanoantenna used in the optical phased array should have high emitting efficiency yet a small size to fit into the compact unit cell. Optical nanoantenna down to subwavelength size have previously been demonstrated in metal [120–122] since the large refractive index of metal results in strong light-matter interaction. However, to make the material systems compatible with current CMOS-compatible silicon photonic process, silicon-based dielectric nanoantenna is preferred.

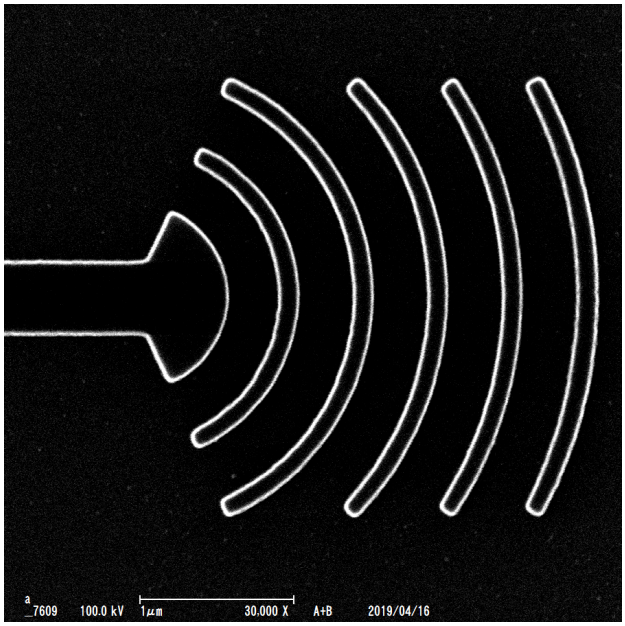

Figure 10.14 SEM pictures of the dielectric optical nanoantenna.

In our approach, the silicon nitride dielectric optical antenna is used. It has a silicon nitride core with a height of 300 nm, with silicon dioxide on bottom and air on top, see Figure 10.12. Due to the relatively large refractive index contrast between silicon nitride (n = 2) and air (n = 1), it creates a strong light-matter interaction and hence high emitting efficiency was achievable. The light emission efficiency of the nanoantenna was simulated with a rigorous three-dimensional (3D) finite-difference time-domain (FDTD) method by OmniSim. The asymmetric geometry of the optical nanoantenna naturally break the up-down symmetry for more downward emission. The optical antenna consists of 6-period circular gratings with a compact footprint of 2.8 μm × 3 μm, see Figure 10.14. The grating is designed to have a pitch of 0.48 μm, which is slightly detuned from the pitch of a second-order grating to avoid severe resonant back-reflections that would disturb the phased array system. Figure 10.15 plots the emitting efficiency as a function of the width of the gratings. The width was

optimized to be 0.1 μm, which has a large downward emission and the smallest reflection and transmission.

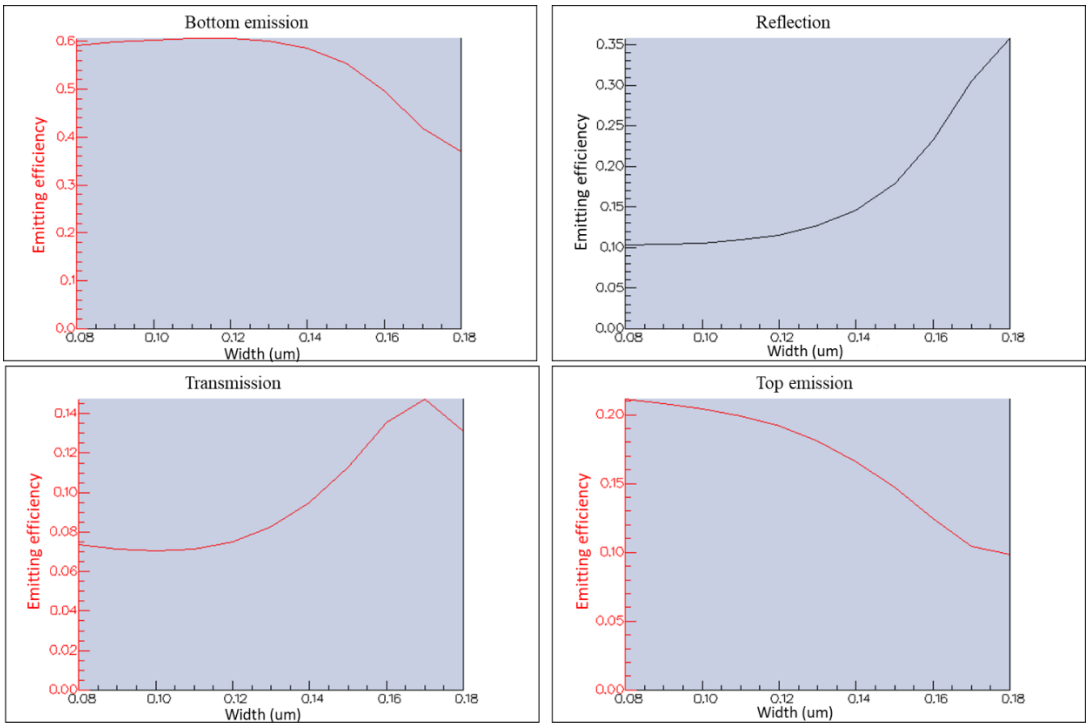

Figure 10.15 The optical emitting efficiency of the dielectric nanoantenna, calculated from the 3D-FDTD simulation.

The corresponding far-field radiation profile was calculated using the near-to-far-field transformation. Figure 10.16 shows the far field radiation profile of the downward emission. The far field radiation profile is viewed from the zenith of the far-field hemisphere. It gives us the power flowing through a unit area of the sphere as a function of spherical angle. The far-field emission is almost vertical, which is critical in the optical phased array application.

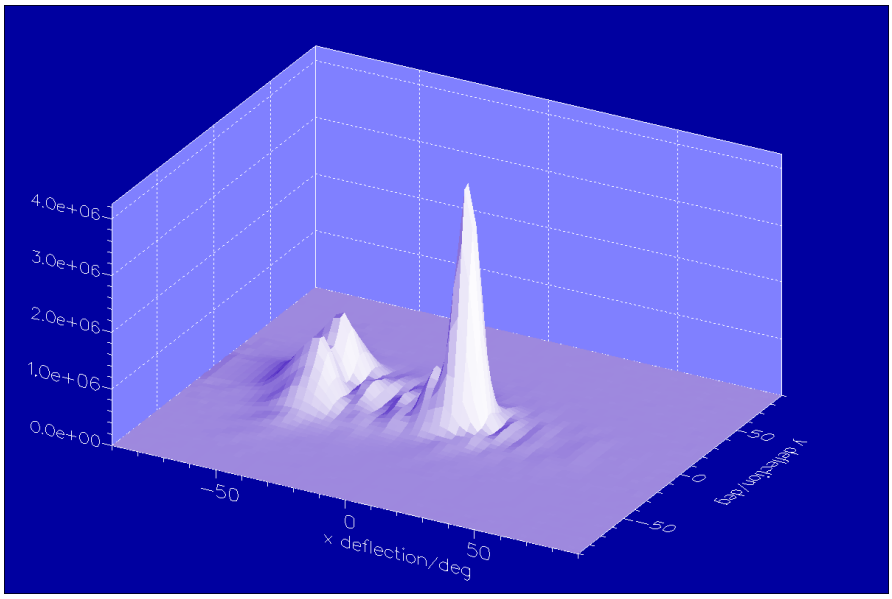

Figure 10.16 The downward far-field emission profile of the optical antenna, calculated by the near-to-far-field transformation.

10.2.4 Array Unit Design

Each array unit consists of a tunable thermo-optical phase shifter that is coupled into an optical antenna. It has a size of 12 μm × 12 μm. The array unit, as the building block of the optical phased array, is to be arrayed to form a large-scale silicon photonic phased array system, where the emitting phase of each array unit is accordingly adjusted. The schematic diagram of the array unit is shown in Figure 10.17, where two array units were put adjacent to each other. The upper part is the top view, and the lower part is the cross view. A directional coupler is designed individually to couple certain amount of the power into each array unit, so that the power is evenly distributed to the whole phased array. An IC chip is flip-bonded to our photonic chip to control the temperature that is applied to the phase shifter. With

the phase being manipulated, the nanoantenna emits light downward through the optical flat substrate to generate sophisticated optical far-field radiation.

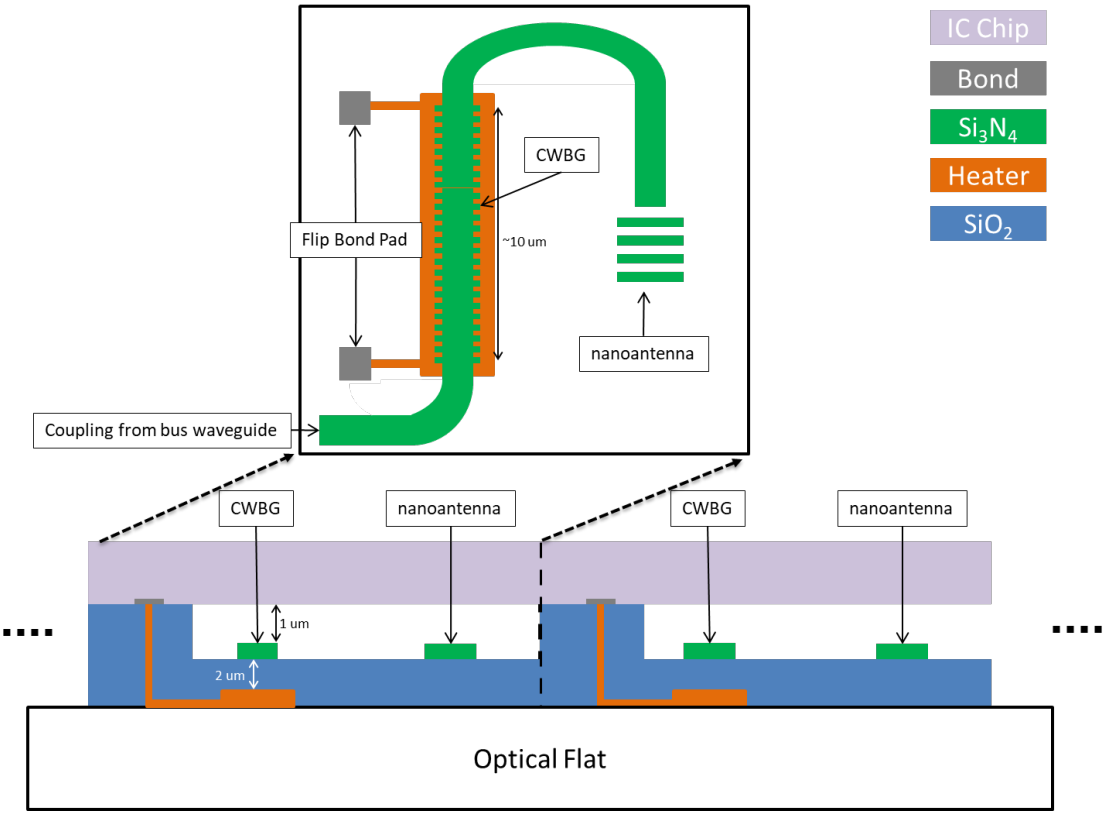

Figure 10.17 The schematic diagram of the array. The upper is the top view; the lower is the cross view, where two array units were put adjacent to each other.

Chapter 11 Conclusions and Perspectives

11.1 Summary of Accomplishments

This part focused on the improvement of the integrated photonic components that can be achieved, when implementing the waveguide Bragg gratings. High-rejection ratio pump filter, Fabry-Perot cavity enhanced four-wave mixing device and slow-light engineered complex waveguide Bragg grating are optimized based on several numerical models developed with ABCD matrix method and demonstrated experimentally.

First, we explored two fabrication steps to meet the demanding accuracy requirement of integrated photonic devices, since the most straightforward and efficient way to achieve highly accurate devices is to improve the precision of the fabrication process. To achieve accurate integrated photonic devices is extremely challenging due to the short wavelength of light and high refractive-index contrast that make the devices very sensitive to even nanometer scale dimensional errors. Every single step during the whole process is critical to reduce the dimensional errors of the resulting devices. Among all fabrication steps, we shared essential approaches to minimize the field stitching error in the electron-beam lithography and introduced three-stage inductively coupled plasma etching to optimize the side wall smoothness.

The filtering of the pump field is essential to isolate the weaker signal and idler fields in the photon-pair generation via SFWM. In general, it requires an extinction ratio larger than 100 dB. However, it has never been achieved without using off-chip filters. Efficient on-chip rejection of the pump light is challenging. An integrated high-

rejection ratio pump filter using a simple periodic waveguide Bragg grating was demonstrated. We introduced an efficient z-shape waveguide design to achieve 83-dB filtering of the pump field by suppressing another supported TM mode in the waveguide and avoiding scattered modes at the output port.

The effect of FWM has enabled useful applications for all-optical signal processing such as high-speed sampling, switching, wavelength conversion, amplification and comb generation. The FWM effect can be dramatically increased when using resonating systems, without compromising speeds because of its small dimensions. We analytically studied the Fabry-Perot cavity enhanced FWM. A numerical model based on ABCD matrix method of Bragg grating was developed to optimize the structural design of Fabry-Perot cavity enhanced FWM device. An FWM conversion efficiency of around -50 dB was observed inside a 1.8-mm long cavity, which was enhanced over 61 dB compared to a single straight waveguide with the same length.

The recent surge in the use of 3D displays and content has been unfortunately accompanied by a rise in psychophysical problems associated with their viewing. To create a true natural-to-senses display, we need to reproduce the entire light field entering the pupil of each eye. Optical phased arrays can be used to generate arbitrary radiation patterns. To reduce the power consumption and pixel size of the phase array, complex waveguide Bragg grating was successfully generated via genetic algorithm to support slow-light modes over certain bandwidth. A 10-μm long CWBG with a slow down factor of 6 and an average transmission of 70% within a bandwidth between 626 nm and 630 nm was demonstrated. Using this CWBG, to achieve a π phase shit requires a temperature increase of about $\Delta T = 175℃$.

11.2 Future Work

The scattering loss due to the mode mismatch between Bragg grating and straight waveguide directly affects the performance of both high-rejection ratio pump filter and Fabry-Perot cavity enhanced FWM device. To reduce the scattering loss, phase matching between the Bragg grating and waveguide, $\beta_{Bragg} = \beta_{wg}$, is necessary. It will minimize the scattering loss at the waveguide-grating interface. A tapered grating can be inserted at the waveguide-grating interface to adiabatically convert the Bloch mode into waveguide mode.

In practice, chromatic dispersion will lead to a mismatch between the converted frequency and the resonant frequency of the cavity. As shown in Figure 9.2, low and anomalous dispersion can be achieved by a simple geometrical optimization. Also, as mentioned in section 9.3, if the confinement factor of the waveguide can be further improved, both the nonlinear coefficient and the FWM conversion efficiency will be increase. So, a potential direction is to find a better waveguide geometry with less dispersion and higher confinement factor.

Bibliography

1. S. GmbH, "ZSW sets European CIGS efficiency record of 22%," http://www.pv-magazine.com/news/details/beitrag/zsw-sets-european-cigs-efficiency-record-of-22_100023961/.

2. S. GmbH, "Solar Frontier hits 22.3% on CIGS cell," http://www.pv-magazine.com/news/details/beitrag/solar-frontier-hits-223-on-cigs-cell_100022342/.

3. S. Jung, S. Ahn, J. H. Yun, J. Gwak, D. Kim, and K. Yoon, "Effects of Ga contents on properties of CIGS thin films and solar cells fabricated by co-evaporation technique," Current Applied Physics **10**, 990–996 (2010).

4. "High efficiency Cu(In,Ga)Se2-based solar cells: Processing of novel absorber structures (PDF Download Available)," https://www.researchgate.net/publication/2838567_High_efficiency_CuInGaSe2-based_solar_cells_Processing_of_novel_absorber_structures.

5. T. Dullweber, O. Lundberg, J. Malmström, M. Bodegård, L. Stolt, U. Rau, H. W. Schock, and J. H. Werner, "Back surface band gap gradings in Cu(In,Ga)Se2 solar cells," Thin Solid Films **387**, 11–13 (2001).

6. R. W. Birkmire and and E. Eser, "POLYCRYSTALLINE THIN FILM SOLAR CELLS:Present Status and Future Potential," Annual Review of Materials Science **27**, 625–653 (1997).

7. H.-W. Schock and R. Noufi, "CIGS-based solar cells for the next millennium," Prog. Photovolt: Res. Appl. **8**, 151–160 (2000).

8. D. Schmid, M. Ruckh, F. Grunwald, and H. W. Schock, "Chalcopyrite/defect chalcopyrite heterojunctions on the basis of CuInSe2," Journal of Applied Physics **73**, 2902–2909 (1993).

9. R. Klenk, "Characterisation and modelling of chalcopyrite solar cells," Thin Solid Films **387**, 135–140 (2001).

10. H. W. Schock and U. Rau, "The role of structural properties and defects for the performance of Cu-chalcopyrite-based thin-film solar cells," Physica B: Condensed Matter **308**, 1081–1085 (2001).

11. T. Negami, N. Kohara, M. Nishitani, T. Wada, and T. Hirao, "Preparation and characterization of Cu(In1−xGax)3Se5 thin films," Appl. Phys. Lett. **67**, 825–827 (1995).

12. C. Persson and A. Zunger, "Anomalous Grain Boundary Physics in Polycrystalline CuInSe2: The Existence of a Hole Barrier," Phys. Rev. Lett. **91**, 266401 (2003).

13. W. K. Metzger and M. Gloeckler, "The impact of charged grain boundaries on thin-film solar cells and characterization," Journal of Applied Physics **98**, 063701 (2005).

14. M. Gloeckler, J. R. Sites, and W. K. Metzger, "Grain-boundary recombination in Cu(In,Ga)Se2 solar cells," Journal of Applied Physics **98**, 113704 (2005).

15. A. Virtuani, E. Lotter, M. Powalla, U. Rau, J. H. Werner, and M. Acciarri, "Influence of Cu content on electronic transport and shunting behavior of Cu(In,Ga)Se2 solar cells," Journal of Applied Physics **99**, 014906-014906–11 (2006).

16. "Grain Boundary Evaluation of Cu(In1-xGax)Se2 Solar Cells," Jpn. J. Appl. Phys. **49**, 062301 (2010).

17. Y. Yan, R. Noufi, and M. M. Al-Jassim, "Grain-Boundary Physics in Polycrystalline ${\mathrm{CuInSe}}_{2}$ Revisited: Experiment and Theory," Phys. Rev. Lett. **96**, 205501 (2006).

18. T. Schlenker, M. L. Valero, H. W. Schock, and J. H. Werner, "Grain growth studies of thin Cu(In, Ga)Se2 films," Journal of Crystal Growth **264**, 178–183 (2004).

19. V. G. Karpov, A. D. Compaan, and D. Shvydka, "Effects of nonuniformity in thin-film photovoltaics," Appl. Phys. Lett. **80**, 4256–4258 (2002).

20. S. Wenger, S. Seyrling, A. N. Tiwari, and M. Grätzel, "Fabrication and performance of a monolithic dye-sensitized TiO2/Cu(In,Ga)Se2 thin film tandem solar cell," Appl. Phys. Lett. **94**, 173508 (2009).

21. K. Taretto, U. Rau, and J. H. Werner, "Numerical simulation of grain boundary effects in Cu(In,Ga)Se2 thin-film solar cells," Thin Solid Films **480**, 8–12 (2005).

22. A. Rockett, "The effect of Na in polycrystalline and epitaxial single-crystal CuIn1−xGaxSe2," Thin Solid Films **480**, 2–7 (2005).

23. S. Sadewasser, "Microscopic characterization of individual grain boundaries in Cu-III–VI2 chalcopyrites," Thin Solid Films **515**, 6136–6141 (2007).

24. U. Rau, K. Taretto, and S. Siebentritt, "Grain boundaries in Cu(In, Ga)(Se, S)2 thin-film solar cells," Appl. Phys. A **96**, 221 (2009).

25. C. Persson and A. Zunger, "Compositionally induced valence-band offset at the grain boundary of polycrystalline chalcopyrites creates a hole barrier," Appl. Phys. Lett. **87**, 211904 (2005).

26. M. J. Hetzer, Y. M. Strzhemechny, M. Gao, M. A. Contreras, A. Zunger, and L. J. Brillson, "Direct observation of copper depletion and potential changes at copper indium gallium diselenide grain boundaries," Appl. Phys. Lett. **86**, 162105 (2005).

27. J. Y. W. Seto, "The electrical properties of polycrystalline silicon films," Journal of Applied Physics **46**, 5247–5254 (1975).

28. A. M. Gabor, J. R. Tuttle, D. S. Albin, M. A. Contreras, R. Noufi, and A. M. Hermann, "High-efficiency CuInxGa1−xSe2 solar cells made from (Inx,Ga1−x)2Se3 precursor films," Applied Physics Letters **65**, 198–200 (1994).

29. U. P. Singh and S. P. Patra, "Progress in Polycrystalline Thin-Film Cu(In,Ga)Se2 Solar Cells," International Journal of Photoenergy **2010**, 1–19 (2010).

30. A. Goetzberger, C. Hebling, and H.-W. Schock, "Photovoltaic materials, history, status and outlook," Materials Science and Engineering: R: Reports **40**, 1–46 (2003).

31. R. Scheer, K. Diesner, and H.-J. Lewerenz, "Experiments on the microstructure of evaporated CuInS2 thin films," Thin Solid Films **268**, 130–136 (1995).

32. N. Amin, "Promises of Cu (In, Ga)Se2thin film solar cells from the perspective of material properties, fabrication methods and current research challenges," Journal of Applied Sciences **11**, 401–410 (2011).

33. J. Palm, V. Probst, A. Brummer, W. Stetter, R. Tölle, T. P. Niesen, S. Visbeck, O. Hernandez, M. Wendl, H. Vogt, H. Calwer, B. Freienstein, and F. Karg, "CIS module pilot processing applying concurrent rapid selenization and sulfurization of large area thin film precursors," Thin Solid Films **431**, 514–522 (2003).

34. K. Bindu, C. S. Kartha, K. P. Vijayakumar, T. Abe, and Y. Kashiwaba, "CuInSe2 thin film preparation through a new selenisation process using chemical bath deposited selenium," Solar Energy Materials and Solar Cells **79**, 67–79 (2003).

35. M. Lammer, U. Klemm, and M. Powalla, "Sodium co-evaporation for low temperature Cu(In,Ga)Se2 deposition," Thin Solid Films **387**, 33–36 (2001).

36. R. Kimura, T. Nakada, P. Fons, A. Yamada, S. Niki, T. Matsuzawa, K. Takahashi, and A. Kunioka, "Photoluminescence properties of sodium incorporation in CuInSe2 and CuIn3Se5 thin films," Solar Energy Materials and Solar Cells **67**, 289–295 (2001).

37. Leeor. Kronik, D. Cahen, and H. W. Schock, "Effects of Sodium on Polycrystalline Cu(In,Ga)Se2 and Its Solar Cell Performance," Adv. Mater. **10**, 31–36 (1998).

38. K. Zweibel, "Issues in thin film PV manufacturing cost reduction," Solar Energy Materials and Solar Cells **59**, 1–18 (1999).

39. R. N. Bhattacharya, W. Batchelor, K. Ramanathan, M. A. Contreras, and T. Moriarty, "The performance of CuIn1−xGaxSe2-based photovoltaic cells prepared from low-cost precursor films," Solar Energy Materials and Solar Cells **63**, 367–374 (2000).

40. M. E. Calixto, R. N. Bhattacharya, P. J. Sebastian, A. M. Fernandez, S. A. Gamboa, and R. N. Noufi, "Cu(In,Ga)Se2 based photovoltaic structure by electrodeposition and processing," Solar Energy Materials and Solar Cells **55**, 23–29 (1998).

41. R. N. Bhattacharya, W. Batchelor, J. E. Granata, F. Hasoon, H. Wiesner, K. Ramanathan, J. Keane, and R. N. Noufi, "CuIn1−xGaxSe2-based photovoltaic cells from electrodeposited and chemical bath deposited precursors," Solar Energy Materials and Solar Cells **55**, 83–94 (1998).

42. S. Taunier, J. Sicx-Kurdi, P. P. Grand, A. Chomont, O. Ramdani, L. Parissi, P. Panheleux, N. Naghavi, C. Hubert, M. Ben-Farah, J. P. Fauvarque, J. Connolly, O. Roussel, P. Mogensen, E. Mahé, J. F. Guillemoles, D. Lincot, and O. Kerrec, "Cu(In,Ga)(S,Se)2 solar cells and modules by electrodeposition," Thin Solid Films **480**, 526–531 (2005).

43. P. P. Prosini, M. L. Addonizio, A. Antonaia, and S. Loreti, "Electrodeposition of copper-indium alloy under diffusion-limiting current control," Thin Solid Films **288**, 90–94 (1996).

44. M. Ganchev, J. Kois, M. Kaelin, S. Bereznev, E. Tzvetkova, O. Volobujeva, N. Stratieva, and A. Tiwari, "Preparation of Cu(In,Ga)Se2 layers by selenization of electrodeposited Cu–In–Ga precursors," Thin Solid Films **511**, 325–327 (2006).

45. M. Kaelin, D. Rudmann, and A. N. Tiwari, "Low cost processing of CIGS thin film solar cells," Solar Energy **77**, 749–756 (2004).

46. V. K. Kapur, A. Bansal, P. Le, and O. I. Asensio, "Non-vacuum processing of CuIn1−xGaxSe2 solar cells on rigid and flexible substrates using nanoparticle precursor inks," Thin Solid Films **431**, 53–57 (2003).

47. D. L. Schulz, C. J. Curtis, R. A. Flitton, H. Wiesner, J. Keane, R. J. Matson, K. M. Jones, P. A. Parilla, R. Noufi, and D. S. Ginley, "Cu-In-Ga-Se nanoparticle colloids as spray deposition precursors for Cu(In, Ga)Se2 solar cell materials," Journal of Elec Materi **27**, 433–437 (1998).

48. T. Nakada, H. Ohbo, M. Fukuda, and A. Kunioka, "Improved compositional flexibility of Cu(In,Ga)Se2-based thin film solar cells by sodium control technique," Solar Energy Materials and Solar Cells **49**, 261–267 (1997).

49. F. Pianezzi, P. Reinhard, A. Chirilă, B. Bissig, S. Nishiwaki, S. Buecheler, and A. N. Tiwari, "Unveiling the effects of post-deposition treatment with different alkaline elements on the electronic properties of CIGS thin film solar cells," Physical Chemistry Chemical Physics **16**, 8843 (2014).

50. Y. M. Shin, C. S. Lee, D. H. Shin, H. S. Kwon, B. G. Park, and B. T. Ahn, "Surface modification of CIGS film by annealing and its effect on the band structure and photovoltaic properties of CIGS solar cells," Current Applied Physics **15**, 18–24 (2015).

51. G. P. Smestad, F. C. Krebs, C. M. Lampert, C. G. Granqvist, K. L. Chopra, X. Mathew, and H. Takakura, "Reporting solar cell efficiencies in Solar Energy Materials and Solar Cells," Solar Energy Materials and Solar Cells **92**, 371–373 (2008).

52. S. Dongaonkar, J. D. Servaites, G. M. Ford, S. Loser, J. Moore, R. M. Gelfand, H. Mohseni, H. W. Hillhouse, R. Agrawal, M. A. Ratner, T. J. Marks, M. S. Lundstrom, and M. A. Alam, "Universality of non-Ohmic shunt leakage in thin-film solar cells," Journal of Applied Physics **108**, 124509 (2010).

53. S. Dongaonkar, S. Loser, E. J. Sheets, K. Zaunbrecher, R. Agrawal, T. J. Marks, and M. A. Alam, "Universal statistics of parasitic shunt formation in solar cells, and its implications for cell to module efficiency gap," Energy Environ. Sci. **6**, 782–787 (2013).

54. J. H. Boyle, B. E. McCandless, W. N. Shafarman, and R. W. Birkmire, "Structural and optical properties of (Ag,Cu)(In,Ga)Se2 polycrystalline thin film alloys," Journal of Applied Physics **115**, 223504 (2014).

55. Y. Tauchi, K. Kim, H. Park, and W. Shafarman, "Characterization of (AgCu)(InGa)$Se_{bf\ 2}$ Absorber Layer Fabricated by a Selenization Process from Metal Precursor," IEEE Journal of Photovoltaics **3**, 467–471 (2013).

56. S. Soltanmohammad and W. N. Shafarman, "Reaction pathway analysis of Ag-alloyed Cu(In, Ga)Se2 absorber materials," in *2016 IEEE 43rd Photovoltaic Specialists Conference (PVSC)* (2016), pp. 2269–2273.

57. Marika Edoff, Tobias Jarmar, and William Shafarman, "High Voc in (Cu,Ag)(In,Ga)Se2 solar cells," PVSC 44 (n.d.).

58. S. Soltanmohammad, L. Chen, B. McCandless, and W. N. Shafarman, "Ag-Cu-In-Ga Metal Precursor Thin Films for (Ag,Cu)(In,Ga)Se2 Solar Cells," IEEE Journal of Photovoltaics **7**, 273–280 (2017).

59. T. J. Coutts, K. A. Emery, and J. Scott Ward, "Modeled performance of polycrystalline thin-film tandem solar cells," Prog. Photovolt: Res. Appl. **10**, 195–203 (2002).

60. T. Duong, Y. Wu, H. Shen, J. Peng, X. Fu, D. Jacobs, E.-C. Wang, T. C. Kho, K. C. Fong, M. Stocks, E. Franklin, A. Blakers, N. Zin, K. McIntosh, W. Li, Y.-B. Cheng, T. P. White, K. Weber, and K. Catchpole, "Rubidium Multication Perovskite with Optimized Bandgap for Perovskite-Silicon Tandem with over 26% Efficiency," Adv. Energy Mater. **7**, n/a-n/a (2017).

61. K. A. Bush, A. F. Palmstrom, Z. J. Yu, M. Boccard, R. Cheacharoen, J. P. Mailoa, D. P. McMeekin, R. L. Z. Hoye, C. D. Bailie, T. Leijtens, I. M. Peters, M. C. Minichetti, N. Rolston, R. Prasanna, S. Sofia, D. Harwood, W. Ma, F. Moghadam, H. J. Snaith, T. Buonassisi, Z. C. Holman, S. F. Bent, and M. D. McGehee, "23.6%-efficient monolithic perovskite/silicon tandem solar cells with improved stability," Nature Energy **2**, nenergy20179 (2017).

62. C. D. Bailie and M. D. McGehee, "High-efficiency tandem perovskite solar cells," MRS Bulletin **40**, 681–686 (2015).

63. C. D. Bailie, M. G. Christoforo, J. P. Mailoa, A. R. Bowring, E. L. Unger, W. H. Nguyen, J. Burschka, N. Pellet, J. Z. Lee, M. Grätzel, R. Noufi, T. Buonassisi, A. Salleo, and M. D. McGehee, "Semi-transparent perovskite solar cells for tandems with silicon and CIGS," Energy Environ. Sci. **8**, 956–963 (2015).

64. T. Todorov, T. Gershon, O. Gunawan, Y. S. Lee, C. Sturdevant, L.-Y. Chang, and S. Guha, "Monolithic Perovskite-CIGS Tandem Solar Cells via In Situ Band Gap Engineering," Adv. Energy Mater. n/a-n/a (2015).

65. Y. Yao, W.-L. Hsu, and M. Dagenais, "High Efficiency Perovskite Solar Cells by a Modified Low-Temperature Solution Process Inter-Diffusion Method," PVSC 44 (n.d.).

66. J. Hedstrom, H. Ohlsen, M. Bodegard, A. Kylner, L. Stolt, D. Hariskos, M. Ruckh, and H. Schock, "ZnO/CdS/Cu(In,Ga)Se2 thin film solar cells with improved performance," in *, Conference Record of the Twenty Third IEEE Photovoltaic Specialists Conference, 1993* (1993), pp. 364–371.

67. F. O. Adurodija, M. J. Carter, and R. Hill, "Synthesis and characterization of CuInSe2 thin films from Cu, In and Se stacked layers using a closed graphite box," Solar Energy Materials and Solar Cells **40**, 359–369 (1996).

68. J. López-García and C. Guillén, "Adjustment of the selenium amount provided during formation of CuInSe 2 thin films from the metallic precursors," Physica Status Solidi (A) Applications and Materials Science **206**, 84–90 (2009).

69. J. Leuthold, C. Koos, and W. Freude, "Nonlinear silicon photonics," Nature Photonics **4**, 535–544 (2010).

70. B. Jalali, "Teaching silicon new tricks," Nature Photonics **1**, 193–195 (2007).

71. G. T. Reed, "The optical age of silicon," Nature **427**, 595 (2004).

72. R. Soref, "The Past, Present, and Future of Silicon Photonics," IEEE Journal of Selected Topics in Quantum Electronics **12**, 1678–1687 (2006).

73. D. J. Blumenthal, R. Heideman, D. Geuzebroek, A. Leinse, and C. Roeloffzen, "Silicon Nitride in Silicon Photonics," Proceedings of the IEEE **106**, 2209–2231 (2018).

74. "Inductively Coupled Plasma Etching (ICP) - Plasma Technology," https://plasma.oxinst.com/campaigns/technology/icp-etching.

75. P. Kaspar, Y. Jeyaram, H. Jäckel, A. Foelske, R. Kötz, and S. Bellini, "Silicon nitride hardmask fabrication using a cyclic CHF3-based reactive ion etching process for vertical profile nanostructures," Journal of Vacuum Science & Technology B **28**, 1179–1186 (2010).

76. V. M. Donnelly and A. Kornblit, "Plasma etching: Yesterday, today, and tomorrow," Journal of Vacuum Science & Technology A **31**, 050825 (2013).

77. D. L. Flamm, D. N. K. Wang, and D. Maydan, "Multiple-Etchant Loading Effect and Silicon Etching in ClF3 and Related Mixtures," J. Electrochem. Soc. **129**, 2755–2760 (1982).

78. J. Dulak, B. J. Howard, and Ch. Steinbrüchel, "Etch mechanism in the reactive ion etching of silicon nitride," Journal of Vacuum Science & Technology A **9**, 775–778 (1991).

79. T. C. Mele, J. Nulman, and J. P. Krusius, "Selective and anisotropic reactive ion etch of LPCVD silicon nitride with CHF3 based gases," Journal of Vacuum Science & Technology B: Microelectronics Processing and Phenomena **2**, 684–687 (1984).

80. G. S. Oehrlein and Y. Kurogi, "Sidewall surface chemistry in directional etching processes," Materials Science and Engineering: R: Reports **24**, 153–183 (1998).

81. T. Zhu, Y. Hu, P. Gatkine, S. Veilleux, J. Bland-Hawthorn, and M. Dagenais, "Arbitrary on-chip optical filter using complex waveguide Bragg gratings," Appl. Phys. Lett. **108**, 101104 (2016).

82. T. Zhu, S. Veilleux, J. Bland-Hawthorn, and M. Dagenais, "Complex Waveguide Bragg Gratings For arbitrary spectral filtering," in *2016 IEEE Photonics Society Summer Topical Meeting Series (SUM)* (2016), pp. 211–212.

83. N. C. Harris, D. Grassani, A. Simbula, M. Pant, M. Galli, T. Baehr-Jones, M. Hochberg, D. Englund, D. Bajoni, and C. Galland, "Integrated Source of Spectrally Filtered Correlated Photons for Large-Scale Quantum Photonic Systems," Phys. Rev. X **4**, 041047 (2014).

84. C. Ma, X. Wang, V. Anant, A. D. Beyer, M. D. Shaw, and S. Mookherjea, "Silicon photonic entangled photon-pair and heralded single photon generation with CAR > 12,000 and $g^{(2)}$(0) < 0.006," Opt. Express, OE **25**, 32995–33006 (2017).

85. J. E. Sharping, K. F. Lee, M. A. Foster, A. C. Turner, B. S. Schmidt, M. Lipson, A. L. Gaeta, and P. Kumar, "Generation of correlated photons in nanoscale silicon waveguides," Opt. Express, OE **14**, 12388–12393 (2006).

86. S. Clemmen, K. P. Huy, W. Bogaerts, R. G. Baets, P. Emplit, and S. Massar, "Continuous wave photon pair generation in silicon-on-insulator waveguides and ring resonators," Opt. Express, OE **17**, 16558–16570 (2009).

87. Y. Hu, Y. Zhang, P. Gatkine, J. Bland-Hawthorn, S. Veilleux, and M. Dagenais, "Characterization of Low Loss Waveguides Using Bragg Gratings," IEEE Journal of Selected Topics in Quantum Electronics **24**, 1–8 (2018).

88. T. Zhu, Y. Hu, P. Gatkine, S. Veilleux, J. Bland-Hawthorn, and M. Dagenais, "Ultrabroadband High Coupling Efficiency Fiber-to-Waveguide Coupler Using Si_3N_4/SiO_2Waveguides on Silicon," IEEE Photonics Journal **8**, 1–12 (2016).

89. M. Palamaru and Ph. Lalanne, "Photonic crystal waveguides: Out-of-plane losses and adiabatic modal conversion," Appl. Phys. Lett. **78**, 1466–1468 (2001).

90. Q. Quan, P. B. Deotare, and M. Loncar, "Photonic crystal nanobeam cavity strongly coupled to the feeding waveguide," Appl. Phys. Lett. **96**, 203102 (2010).

91. M. A. Foster, A. C. Turner, J. E. Sharping, B. S. Schmidt, M. Lipson, and A. L. Gaeta, "Broad-band optical parametric gain on a silicon photonic chip," Nature **441**, 960 (2006).

92. R. L. Espinola, J. I. Dadap, R. M. Osgood, S. J. McNab, and Y. A. Vlasov, "C-band wavelength conversion in silicon photonic wire waveguides," Opt. Express, OE **13**, 4341–4349 (2005).

93. H. Fukuda, K. Yamada, T. Shoji, M. Takahashi, T. Tsuchizawa, T. Watanabe, J. Takahashi, and S. Itabashi, "Four-wave mixing in silicon wire waveguides," Opt. Express, OE **13**, 4629–4637 (2005).

94. J. S. Levy, A. Gondarenko, A. C. Turner-Foster, M. A. Foster, A. L. Gaeta, and M. Lipson, "Four-wave mixing in integrated silicon nitride waveguides," in *2009 Conference on Lasers and Electro-Optics and 2009 Conference on Quantum Electronics and Laser Science Conference* (2009), pp. 1–2.

95. A. Fülöp, C. J. Krückel, D. Castelló-Lurbe, E. Silvestre, and V. Torres-Company, "Triply resonant coherent four-wave mixing in silicon nitride microresonators," Opt. Lett., OL **40**, 4006–4009 (2015).

96. A. C. Turner, M. A. Foster, A. L. Gaeta, and M. Lipson, "Ultra-low power parametric frequency conversion in a silicon microring resonator," Opt. Express, OE **16**, 4881–4887 (2008).

97. P. P. Absil, J. V. Hryniewicz, B. E. Little, P. S. Cho, R. A. Wilson, L. G. Joneckis, and P.-T. Ho, "Wavelength conversion in GaAs micro-ring resonators," Opt. Lett., OL **25**, 554–556 (2000).

98. J. M. C. Boggio, D. Bodenmüller, T. Fremberg, R. Haynes, M. M. Roth, R. Eisermann, M. Lisker, L. Zimmermann, and M. Böhm, "Dispersion engineered silicon nitride waveguides by geometrical and refractive-index optimization," J. Opt. Soc. Am. B, JOSAB **31**, 2846–2857 (2014).

99. Y. Okawachi, K. Saha, J. S. Levy, Y. H. Wen, M. Lipson, and A. L. Gaeta, "Octave-spanning frequency comb generation in a silicon nitride chip," Opt. Lett., OL **36**, 3398–3400 (2011).

100. A. M. Darwish, E. P. Ippen, H. Q. Le, J. P. Donnelly, and S. H. Groves, "Optimization of four-wave mixing conversion efficiency in the presence of nonlinear loss," Appl. Phys. Lett. **69**, 737–739 (1996).

101. K. Akeley, S. J. Watt, A. R. Girshick, and M. S. Banks, "A Stereo Display Prototype with Multiple Focal Distances," in *ACM SIGGRAPH 2004 Papers*, SIGGRAPH '04 (ACM, 2004), pp. 804–813.

102. M. Wöpking, "Viewing comfort with stereoscopic pictures: An experimental study on the subjective effects of disparity magnitude and depth of focus," Journal of the Society for Information Display **3**, 101–103 (1995).

103. M. Mon-Williams, J. P. Wann, and S. Rushton, "Binocular vision in a virtual world: visual deficits following the wearing of a head-mounted display," Ophthalmic Physiol Opt **13**, 387–391 (1993).

104. J. P. Wann, S. Rushton, and M. Mon-Williams, "Natural problems for stereoscopic depth perception in virtual environments," Vision Research **35**, 2731–2736 (1995).

105. S. J. Watt, K. Akeley, and M. S. Banks, "Focus cues to display distance affect perceived depth from disparity," Journal of Vision **3**, 66–66 (2003).

106. G. Mather and D. R. R. Smith, "Depth cue integration: stereopsis and image blur," Vision Research **40**, 3501–3506 (2000).

107. M. S. Banks, J. Kim, and T. Shibata, "Insight into Vergence-Accommodation Mismatch," Proc SPIE **8735**, (2013).

108. "Computational Models of Visual Processing," https://mitpress.mit.edu/books/computational-models-visual-processing.

109. M. Levoy and P. Hanrahan, "Light Field Rendering," in *Proceedings of the 23rd Annual Conference on Computer Graphics and Interactive Techniques*, SIGGRAPH '96 (ACM, 1996), pp. 31–42.

110. S. J. Gortler, R. Grzeszczuk, R. Szeliski, and M. F. Cohen, "The Lumigraph," in *Proceedings of the 23rd Annual Conference on Computer Graphics and Interactive Techniques*, SIGGRAPH '96 (ACM, 1996), pp. 43–54.

111. "A practical algorithm for the determination of phase from image and diffraction plane pictures," https://www.researchgate.net/publication/221725051_A_practical_algorithm_for_the_determination_of_phase_from_image_and_diffraction_plane_pictures.

112. J. R. Fienup, "Reconstruction of an object from the modulus of its Fourier transform," Opt. Lett., OL **3**, 27–29 (1978).

113. J. Sun, E. Timurdogan, A. Yaacobi, E. S. Hosseini, and M. R. Watts, "Large-scale nanophotonic phased array," Nature **493**, 195–199 (2013).

114. J. Sun, E. Timurdogan, A. Yaacobi, Z. Su, E. S. Hosseini, D. B. Cole, and M. R. Watts, "Large-Scale Silicon Photonic Circuits for Optical Phased Arrays," IEEE Journal of Selected Topics in Quantum Electronics **20**, 264–278 (2014).

115. E. Brinkmeyer, "Simple algorithm for reconstructing fiber gratings from reflectometric data," Opt. Lett., OL **20**, 810–812 (1995).

116. L. Poladian, "Group-delay reconstruction for fiber Bragg gratings in reflection and transmission," Opt. Lett., OL **22**, 1571–1573 (1997).

117. G. Lenz, B. J. Eggleton, C. R. Giles, C. K. Madsen, and R. E. Slusher, "Dispersive properties of optical filters for WDM systems," IEEE Journal of Quantum Electronics **34**, 1390–1402 (1998).

118. T. M. Press, "Adaptation in Natural and Artificial Systems," https://mitpress.mit.edu/books/adaptation-natural-and-artificial-systems.

119. Z. Michalewicz, *Genetic Algorithms + Data Structures = Evolution Programs*, 3rd ed. (Springer-Verlag, 1996).

120. P. Mühlschlegel, H.-J. Eisler, O. J. F. Martin, B. Hecht, and D. W. Pohl, "Resonant Optical Antennas," Science **308**, 1607–1609 (2005).

121. A. Yaacobi, E. Timurdogan, and M. R. Watts, "Vertical emitting aperture nanoantennas," Opt. Lett., OL **37**, 1454–1456 (2012).

122. L. Tang, S. E. Kocabas, S. Latif, A. K. Okyay, D.-S. Ly-Gagnon, K. C. Saraswat, and D. A. B. Miller, "Nanometre-scale germanium photodetector enhanced by a near-infrared dipole antenna," Nature Photonics **2**, 226–229 (2008).